Atomic Scale Simulations of the Solid Electrolyte $Li_7La_3Zr_2O_{12}$

by

Seungho Yu

A dissertation submitted in partial fulfillment
of the requirements for the degree of
Doctor of Philosophy
(Mechanical Engineering)
in the University of Michigan
2018

Doctoral Committee:

Associate Professor Donald Siegel, Chair
Professor Udo Becker
Assistant Professor Neil Dasgupta
Associate Professor Jeff Sakamoto

Seungho Yu

yseungho@umich.edu

ORCID iD: 0000-0003-3912-6463

Acknowledgements

First, I would like to express my sincere appreciation to my advisor, Professor Don Siegel, for his invaluable mentorship during my Ph.D. studies. Without his guidance and persistent help this dissertation would not have been possible.

I am also deeply grateful to Professor Jeff Sakamoto, whose research insights have been greatly beneficial and helpful to me. I additionally thank Professors Neil Dasgupta and Udo Becker for their valuable advice and service on my committee.

I would like to thank Dr. Jeff Wolfenstine, Dr. Travis Thompson, Dr. Asma Sharafi, and Eric Kazyak for their experimental efforts. I am also grateful to members of the Siegel research group for their supportive discussions.

This work was supported by the U.S. Department of Energy (DOE) Advanced Battery Material Research (BMR) program under Grant DE-EE-0006821 and Advanced Research Projects Agency – Energy (ARPA-e), grant no. DE-AR0000653. I also acknowledge financial support from the Kwanjeong Educational Foundation.

Last but not least, I am greatly indebted to my parents and my wife, Sooyeon Kim, for their warm love, encouragement, and endless support.

Table of Contents

List of Tables

List of Figures

Abstract

Solid-state electrolytes are attracting increasing attention for applications in high energy density batteries. At present, $Li_7La_3Zr_2O_{12}$ (LLZO) is one of the most promising Li solid electrolytes due its favorable combination of high conductivity and chemical stability against Li metal. However, there are several challenges that potentially limit the use of LLZO practically. The work presented in this dissertation characterizes several properties of LLZO at the atomic scale using density functional theory (DFT) and molecular dynamics (MD) calculations.

Calculations addressing the electrochemical window of LLZO, the impact of exposure to air, elastic properties, grain boundary transport, and potential dendrite formation mechanisms are presented. Firstly, DFT calculations of absolute band edge positions indicate that LLZO is an excellent electronic insulator with an intrinsic electrochemical window of 0 to 4 V vs. Li/Li^+. Next, the impact of exposure to humid air is examined. The thermodynamics of Li_2CO_3 surface layers is characterized, in combination with the bulk protonation of LLZO. The impact on Li ion transport is examined as a function of proton exchange. The formation of surface contamination layers is predicted to reduce the wettability between Li and LLZO, resulting in increased interfacial resistance.

Regarding elastic properties, linear elasticity models and the calculated shear modulus suggest that LLZO should be sufficiently stiff to suppress lithium dendrite formation. However, subsequent experimental studies have shown that elastic properties alone are insufficient for achieving dendrite suppression: microstructural features of the solid electrolyte should also be

accounted for. Toward this goal, three hypotheses regarding microstructural features are examined. More specifically, we consider the possibility that dendrites can result from focusing of the Li-ion current caused by (i) limited contact caused by surface contamination and poor wetting at the Li/SE interface or (ii) from fast Li-ion migration along GBs; alternatively, (iii) softening in the vicinity of GBs could foster lithium accumulation during plating. Cleaning the surface of LLZO (scenario 1) appears helpful in delaying the onset of Li penetration, but appears to be insufficient on its own, as dendrites are still observed at high current densities. The 'fast GB diffusion' hypothesis is tested by calculating the rate of Li-ion migration along three low-energy GBs of LLZO. These calculations reveal that Li transport is generally reduced in the GB region, ruling out the second hypothesis. GB softening could arise from deviations in density and atomic structure near the GB plane. MD calculations indicate that significant softening can occur in the immediate vicinity of GBs. We propose that nanoscale softening attributed to microstructural features such as GB may also contribute to Li penetration of nominally stiff solid electrolytes.

Chapter 1 Introduction

1.1 Motivation

Lithium ion batteries are now widely used in portable electronics, and are transitioning to new applications in electric vehicles (EV) and stationary energy storage systems.[1–5] To accelerate this transition, it is desirable to develop batteries with higher energy densities. Optimization of Li-ion systems has largely focused on improving electrode properties, for example, by raising the voltage of cathodes and increasing the capacity of anodes.[3,4] A promising, yet less examined alternative strategy is to replace the battery's liquid electrolyte with a fast ion conducting solid.[6,7] A viable solid-state electrolyte could unlock several of the high-capacity battery concepts shown in Figure 1.1:[2] For example, employing Li metal anodes enables emerging cell chemistries such as Li-S and Li-air.[2,8–12]

The substitution of flammable liquid electrolytes with stable solid-state compounds also offers clear safety advantages.[13,14] Inorganic solid electrolytes are intrinsically non-flammable compared to carbonate liquid electrolytes. Additionally, Li dendrite formation in liquid electrolytes can be suppressed (in principle) by the use of a stiff solid electrolyte.[15]

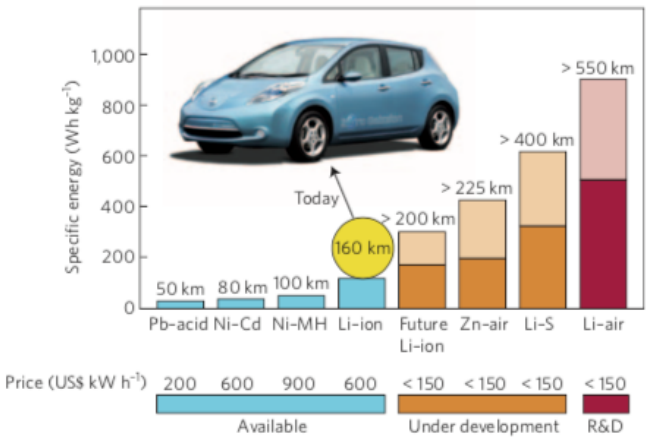

Figure 1.1 Specific energies for existing and developmental batteries along with estimated driving distances and pack prices. Taken from Bruce *et* al.[2]

Finally, the wide electrochemical window of some solids could enable the use of high voltage cathodes, resulting in additional gains in energy density.[7] Carbonate based liquid electrolytes typically have electrochemical windows that result in oxidative decomposition at voltages greater than 4.3 V.[7,16] Solid electrolytes with a window beyond 5 V would enable high energy density cathodes such as spinel $LiMn_{1.5}Ni_{0.5}O_4$ which operates at 4.7 V.[7,17,18]

1.2 Solid Electrolytes

A viable solid electrolyte should satisfy several performance requirements simultaneously:[19,20] it should possess high Li-ion conductivity, ~1 mS cm^{-1} or higher, with low electronic conductivity; chemical and electrochemical stability against the Li metal anode and state-of-the-art cathodes (5 V or higher vs. Li/Li^+) is also essential; finally, it should exhibit sufficient mechanical properties.

Various types of solid electrolytes have been developed as shown in Figure 1.2.[20] Sulfide materials presently exhibit higher ionic conductivities than oxides, which has been suggested to arise from the higher polarizability of the sulfide ion.[21] For example, $Li_{10}GeP_2S_{12}$ (LGPS)

exhibits an ionic conductivity of 12 mS cm^{-1} at room temperature, which is comparable to conventional liquid electrolytes.[22] However, sulfides are hygroscopic, and form toxic H_2S when exposed to moisture.[23] On the other hand, oxides generally exhibit high stability against air and ease of handling.

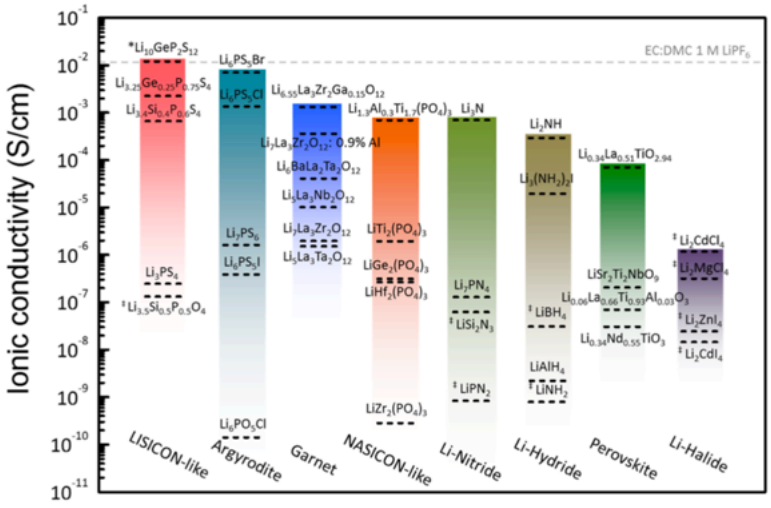

Figure 1.2 Ionic conductivity of several categories of solid-state lithium-ion conductors. Adapted from Bachman *et* al.[20]

Among Li-ion conducting oxides, NaSICON (Na Super Ionic CONductor) type solid electrolytes such as $Li_{1.3}Al_{0.3}Ti_{1.7}(PO_4)_3$ have been reported to exhibit high conductivity, ~ 1 mS/cm;[24,25] however, this compound is unstable in contact with Li.[26] Perovskites with the nominal formulation $Li_{3x}La_{2/3-x}TiO_3$ show high conductivity in the 0.1 to 1 mS/cm range.[25,27] Nevertheless, these materials exhibit high grain boundary resistance and are unstable in contact with Li.[20,25,27] At present, perhaps the most promising Li-ion conducting oxides are garnets with nominal composition $Li_7La_3Zr_2O_{12}$.[28,29] Commonly referred to as LLZO, this oxide exhibits a favorable combination of high conductivity (~1 mS cm^{-1}), with early reports indicating chemical stability against Li metal.[30–33]

1.3 $Li_7La_3Zr_2O_{12}$ (LLZO)

The garnet mineral structure represents a family of complex oxides spanning a broad range of compositions.[28,34] Of the possible garnet formulations, the cubic phase with composition $Li_7La_3Zr_2O_{12}$ (LLZO) has recently emerged as one of the most promising solid electrolytes.

The garnet structure $A_3B_3C_2O_{12}$ is comprised of a $B_3C_2O_{12}$ framework structure of B cations in 8-coordination sites and C cations in octahedral sites.[35] The Li migration path follows the three-dimensional interstitial space within the framework, consisting of tetrahedral sites bridged by octahedral sites.[36] Compared to the three Li in the $Li_3Nd_3Te_2O_{12}$ garnet where Li ions are ordered into the tetrahedral sites[37], additional Li ions are "stuffed" into the interstitial space in LLZO,[38–40] resulting in Li occupation of the octahedral sites. Figure 1.3 shows the Li sublattice for two types of LLZO: the cubic and tetragonal polymorphs. Li ions are distributed amongst partially occupied tetrahedral 24d (56.4 %) and octahedral 96h (44.2 %) sites in cubic LLZO,[36] while they form a fully ordered distribution in tetragonal LLZO.[41] In tetragonal LLZO, the 24d sites present in the cubic polymorph are transformed into fully occupied tetragonal 8a sites and vacant 16e sites (denoted as small spheres in Figure 1.3), while the 16f and 32g sites are fully occupied.[41–43] In other words, the 56 Li atoms in the unit cell of LLZO (8 formula units) are distributed amongst the partially-occupied 24d (~13 Li atoms) and 96h (~43 Li atoms) sites in cubic LLZO, and amongst the fully occupied 8a (8 Li atoms), 16f (16 Li atoms), and 32g (32 Li atoms) sites in tetragonal LLZO.

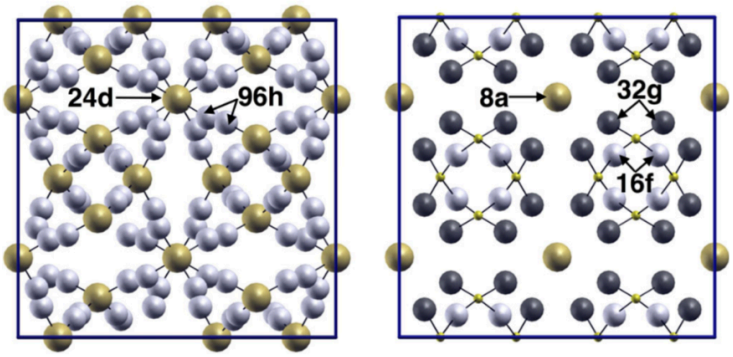

Figure 1.3 Li sublattice for the cubic (left) and tetragonal (right) phases of LLZO. Taken from Bernstein *et* al.[41]

At room temperature, stoichiometric LLZO adopts a tetragonal crystal structure (space group $Ia\bar{4}d$).[42] This polymorph is of less interest for solid electrolyte applications than the cubic polymorph, as the former is limited by low ionic conductivity (~10^{-6} S cm^{-1}) due to the fully ordered Li distribution. However, supervalent doping stabilizes the (typically high-temperature) cubic crystal phase at room temperature (space group $Ia\bar{3}d$), which has a much higher conductivity, ~10^{-4}-10^{-3} S cm^{-1}.[30,32,33,44] Dopants are also expected to increase the degree of vacancy disorder within the Li sub-lattice, leading to enhanced hopping paths for Li^+ and an increase in conductivity. For example, substitution of 0.2-0.24 moles of aluminum (nominal oxidation state of 3+) for lithium stabilizes the cubic phase and creates 0.4-0.48 moles of lithium vacancies per LLZO formula unit.[30] In this phase the ionic conductivity is increased to 0.4 mS/cm at 298 K. Density functional and molecular dynamics calculations demonstrated that the transition from the tetragonal to cubic phase occurs for Li vacancy concentrations greater than 0.4–0.5 per LLZO formula unit.[41] An alternative to Al doping is substitution of Ta^{5+} on Zr^{4+} sites. Substitution of Ta^{5+} is preferred to Al doping, since Ta, unlike Al, does not reside on the Li sublattice, and thus yields higher conductivity. In fact, $Li_{6.5}La_3Zr_{1.5}Ta_{0.5}O_{12}$ (0.5 Li vacancy per formula unit) has achieved a conductivity close to 1 mS/cm at room temperature.[31]

1.4 Challenges

Electrochemical window. Ideally, a solid electrolyte should be chemically stable against Li metal.[28] Garnets are typically wide-band-gap oxides that are expected to be stable at high oxidation potentials.[45] However, the intrinsic electrochemical window (EW) is poorly defined, and should be characterized to clarify the potential for undesirable electronic transport (via charge injection) and decomposition of LLZO. Stability window data for LLZO as reported in recent experiments is based on transient techniques such as cyclic voltammetry (CV), which can be insufficient to determine the EW.[45] A careful determination of the intrinsic EW of the bulk LLZO will aid in understanding its electrochemical stability.

Surface contamination mechanism. LLZO is unstable with respect to humid air, and it can also react with CO_2 to form Li_2CO_3 on the surface, presumably resulting in high interfacial resistance.[46] However, consensus regarding these reaction pathways, their products, and their consequences for performance has not been achieved. For example, Larraz et al. showed that LLZO reacts with H_2O forming LiOH as intermediate phase, and the LiOH subsequently reacts with CO_2 in air to form Li_2CO_3.[46] Conversely, Cheng et al. reported that LLZO reacts with water to form Li-deficient garnet and LiOH, without Li^+/H^+ ion exchange.[47] Li_2CO_3 formation can either occur through CO_2 absorption by LiOH or the direct reaction of LLZO with CO_2.[47] Clarifying these factors will further our understanding of the origin(s) of resistance at electrode/LLZO interfaces.

Surface modification. The interfacial resistance between a Li metal anode and LLZO is a critical factor for developing efficient solid-state batteries. While several studies have reported

significantly higher interfacial resistance than in conventional (liquid-electrolyte) Li-ion batteries,[48,49] coating of the LLZO surface has dramatically lowered this resistance.[50–52] The reduction of interfacial resistance was caused by the enhanced Li wettability of the surface, but the underlying mechanisms are not well understood.[50–52] It remains to be seen if interfacial coatings are required to achieve low interfacial resistance; can similar improvements be achieved by minimizing reactivity of LLZO with air, water, and CO_2?

Li dendrite formation. Li metal cells based on liquid electrolytes exhibit the formation of Li dendrites during Li plating (during charge), which leads to an internal short circuit between the electrodes.[5,45] Use of a stiff solid electrolyte in place of a liquid electrolyte can in principle suppress Li dendrite formation. According to the model of Monroe and Newman,[15,53] a solid electrolyte having a shear modulus that is a factor of approximately 2 times greater than the shear modulus of metallic Li should suppress dendrite initiation. Nevertheless, Li dendrites could still form even in the presence of an electrolyte that satisfies Monroe's criterion if microstructural features in the solid results in inhomogeneous Li plating. For example, recent studies showed that Li dendrites can penetrate LLZO membranes along its grain boundary network, resulting in cell failure.[54] This surprising result indicates that microstructural features, and not elastic properties alone,[15] should be considered in the design of practical solid electrolytes.

Grain boundary resistance. The typical procedure for the synthesis of solid electrolytes results in a polycrystalline solid rather than a single crystal monolith. Grain boundaries (GBs) between individual crystallites can influence of the transport properties due to their different structure and potentially distinct chemical composition compared to the bulk. Regarding the ion transport at

GBs, earlier studies have shown that ion diffusivity can be enhanced or suppressed at GBs. In LLZO, several studies showed that the presence of GB can decrease the Li ion conductivity,[55–59] although the magnitude of this effect can be small and depends sensitively on processing conditions. At present, the atomic-scale processes occurring at GB in LLZO, including transport mechanisms and local elastic properties, remain poorly understood.

1.5 Goals and Outline

The primary purpose of this thesis is to characterize several properties of LLZO at the atomic scale, focusing on key properties that are expected to limit performance. This approach allows for the development of the fundamental understanding needed to overcome the limitations presented in section 1.4. Three classes of calculations are performed: bulk, surface, and GB. For bulk LLZO, structural, electrical, and elastic properties are studied to characterize intrinsic features. Surface calculations are performed to characterize electrochemical stability and the reactivity in air. Finally, ion transport and elastic properties at GBs are investigated. First principles calculations and molecular dynamics simulations are adopted as the primary characterization techniques.

A brief outline of this thesis is given below:

Chapter 2 presents the methodology of atomic scale simulations employed in this thesis. First, the fundamentals of Density Functional Theory (DFT) are introduced, including the Kohn-Sham equations, exchange correlation functionals, and quasi particle GW methods. Next, an overview of classical molecular dynamics (MD) is presented. Two interatomic potentials used in the MD simulations are also described in the methodology chapter.

Chapter 3 discusses the electronic properties and electrochemical stability window of LLZO. DFT and G_0W_0 methods are used to predict the density of states and band gap for bulk LLZO. The electrochemical window is determined using a hybrid functional by aligning the planar-averaged electrostatic potential in bulk LLZO with that in surface slabs.

Chapter 4 addresses the reaction of LLZO with humid air, and involving the protonation of bulk LLZO. First, the thermodynamics of hydration and carbonation were examined using DFT calculations. The interfacial resistance of the surface contamination layers is also examined using DFT calculations by estimating the Li wettability. Finally, the transport properties within protonated LLZO were studied using *ab initio* MD.

Chapter 5 presents the elastic properties of Al- and Ta-doped LLZO using DFT calculations. The predicted elastic properties are compared to the experimental values from measurements, and found to be in excellent agreement. The elastic properties of metallic Li are also revisited using DFT calculations.

Chapter 6 probes grain boundary (GB) contributions to Li ion transport. The energetics, composition, and transport properties of three low-energy ($\Sigma3$ & $\Sigma5$) symmetric tilt GBs in LLZO were investigated by combining classical Monte Carlo and MD simulations.

Chapter 7 describes another possible mechanism for Li metal penetration in LLZO, GB softening, using classical MD calculations. The elastic constants associated with uniaxial strain perpendicular to the GB plane and with shear parallel to the GB were calculated at 300 K. MD results indicate the possibility for severe softening in elastic properties in the immediate vicinity of the GB.

Finally, Chapter 8 concludes this thesis with a brief summary of our findings and possible extensions.

The computational studies described in this thesis have been, or are currently in review, in the following peer-reviewed publications.[60–64] Papers 1-4 and 7 describe joint computational-experimental studies performed with experimental colleagues. Papers 5 and 6 describe studies that are entirely computational in nature.

1. S. Yu, R. D. Schmidt, R. G. Mendez, E. Herbert, N. J. Dudney, J. B. Wolfenstine, J. Sakamoto, and D. J. Siegel, "Elastic Properties of the Solid Electrolyte $Li_7La_3Zr_2O_{12}$ (LLZO)", *Chem. Mater.*, **2016**, 28 (1), 197–206.

2. T. Thompson, S. Yu, L. Williams, R. D. Schmidt, R. G. Mendez, J. Wolfenstine, J. L. Allen, E. Kioupakis, D. J. Siegel, and J. Sakamoto, "Electrochemical Window of the Li-Ion Solid Electrolyte $Li_7La_3Zr_2O_{12}$", *ACS Energy Lett.*, **2017**, 2, 462−468.

3. A. Sharafi, S. Yu, M. Naguib, M. Lee, C. Ma, H. M. Meyer, J. Nanda, M. Chi, D. J. Siegel, and J. Sakamoto, "Impact of Air Exposure and Surface Chemistry on Li- $Li_7La_3Zr_2O_{12}$ Interfacial Resistance", *J. Mater. Chem. A*, **2017**, 5, 13475−13487.

4. A. Sharafi, E. Kazyak, A. L. Davis, S. Yu, T. Thompson, D. J. Siegel, N. P. Dasgupta, and J. Sakamoto, "Surface Chemistry Mechanism of Ultra-Low Interfacial Resistance in the Solid-State Electrolyte $Li_7La_3Zr_2O_{12}$". *Chem. Mater.*, **2017**, 29 (18), 7961−7968.

5. S. Yu, and D. J. Siegel, "Grain Boundary Contributions to Li-Ion Transport in the Solid Electrolyte $Li_7La_3Zr_2O_{12}$ (LLZO)", *Chem. Mater.*, **2017**, 29 (22), 9639–9647.

6. S. Yu, and D. J. Siegel, "Grain Boundary Softening: A Mechanism for Lithium Metal Penetration through Stiff Solid Electrolytes", submitted.

7. X. Liu, Y. Chen, Z. D. Hood, C. Ma, S. Yu, A. Sharafi, H. Wang, K. An, J. Sakamoto, Y. Cheng, N. H. Jalarvo, D. J. Siegel, and, M. Chi, "Elucidating the mobility of H^+ and Li^+ ions

in protonated LLZO ($Li_{6.25-x}H_xAl_{0.25}La_3Zr_2O_{12}$) by combining neutron and electron spectroscopy with first-principles calculations", in preparation.

Chapter 2 Methodology

2.1 First Principles Calculations

2.1.1 Kohn-Sham Density Functional Theory

The Schrödinger equation is the fundamental equation that describes the physics in quantum mechanical systems given by

$$i\hbar\frac{d\Psi}{dt} = \widehat{H}\Psi \tag{2.1}$$

where $\hbar$ is the reduced Planck constant, Ψ is the many-body wavefunction, and $\widehat{H}$ is the Hamiltonian operator. Since the equation is extremely complex, this equation is simplified by following assumptions. First, the system is time-independent and non-relativistic. Second, the Born-Oppenheimer approximation assumes that nuclei are treated as static since the nuclei are significantly heavier than the electrons. Under this assumption, only the electronic part is considered quantum-mechanically. Finally, electrons are assumed to be in their ground state. The resulting equation is given by

$$\widehat{H}\Psi(r_{\text{electron}}) = E\Psi(r_{\text{electron}}) \tag{2.2}$$

where E is the total energy of the system and r_{electron} is the coordinate of electrons.

Despite of these assumptions, solving the time-independent Schrödinger equation in Eq. (2.2) is still infeasible except for the smallest hydrogen systems. Hohenberg and Kohn's formulation of Density Functional Theory (DFT)[65] adopts a simpler method by mapping a system of interacting electrons on to a system of non-interacting one-electron. Hohenberg and Kohn's two theorems provided the formal basis of DFT. The first Hohenberg and Kohn (HK) theorem states that the external potential $V_{\text{ext}}(\boldsymbol{r})$ is solely determined by the ground-state charge density $n_0(\boldsymbol{r})$. The second HK theorem states that total energy of an electronic system is a functional of the charge density,

$$E[n(\boldsymbol{r})] = F[n(\boldsymbol{r})] + \int V_{\text{ext}}(\boldsymbol{r}) n(\boldsymbol{r})\, d\boldsymbol{r} \tag{2.3}$$

and that the global minimum in energy E_0 corresponds to the ground state charge density $n_0(\boldsymbol{r})$.

Using the Kohn-Sham ansatz,[66] Eq. 2.3 is expressed in the form of a system of fictitious non-interacting electrons,

$$E[n(\boldsymbol{r})] = E_{\text{kin}}^{\text{non}}[n(\boldsymbol{r})] + \int V_{\text{ext}}(\boldsymbol{r}) n(\boldsymbol{r})\, d\boldsymbol{r} + E_{\text{H}}[n(\boldsymbol{r})] + E_{\text{XC}}[n(\boldsymbol{r})] \tag{2.4}$$

where $E_{\text{kin}}^{\text{non}}[n(\boldsymbol{r})]$ is the kinetic energy of a set of non-interacting electrons, $E_{\text{H}}[n(\boldsymbol{r})]$ is the classical Coulomb interaction, and $E_{\text{XC}}[n(\boldsymbol{r})]$ is the exchange-correlation energy. The charge density is defined in terms of the non-interacting single-particle wavefunctions ψ_i for the non-interacting N electrons system:

$$n(\boldsymbol{r}) = \sum_{i=1}^{N} \psi_i^*(\boldsymbol{r})\, \psi_i(\boldsymbol{r}) \tag{2.5}$$

The kinetic energy of the non-interacting electrons $E_{\text{kin}}^{\text{non}}$ is expressed as

$$E_{\text{kin}}^{\text{non}}[n(\boldsymbol{r})] = \frac{-\hbar^2}{2m} \sum_{i=1}^{N} \psi_i^*(\boldsymbol{r}) \nabla^2\, \psi_i(\boldsymbol{r}) \tag{2.6}$$

The Hartree energy E_{H} between an electron at $\boldsymbol{r}$ and the mean electron density at $\boldsymbol{r}'$ is given by

$$E_{\mathrm{H}}[n(\boldsymbol{r})] = \frac{1}{2}\iint \frac{n(\boldsymbol{r})n(\boldsymbol{r}')}{|\boldsymbol{r}-\boldsymbol{r}'|}d\boldsymbol{r}d\boldsymbol{r}' \tag{2.7}$$

The exact functional dependence upon $n(\boldsymbol{r})$ for the exchange-correlation energy E_{XC} is unavailable and the solution of DFT rely upon the accurate approximation for the exchange-correlation energy $E_{\mathrm{XC}}[n(\boldsymbol{r})]$.

The ground state energy can be found using the Kohn-Sham (KS) equations, which is the same form as the time-independent Schrödinger equation for non-interacting electrons in an effective local potential:

$$\left[-\frac{\hbar^2}{2m}\nabla^2 + V_{\mathrm{ext}}[n(\boldsymbol{r})] + V_{\mathrm{H}}[n(\boldsymbol{r})] + V_{\mathrm{XC}}[n(\boldsymbol{r})]\right]\psi_i(\boldsymbol{r}) = \varepsilon_i\psi_i(\boldsymbol{r}) \tag{2.8}$$

where,

$$V_{\mathrm{H}}[n(\boldsymbol{r})] = \frac{\delta E_{\mathrm{H}}[n(\boldsymbol{r})]}{\delta n(\boldsymbol{r})} \tag{2.9}$$

and,

$$V_{\mathrm{XC}}[n(\boldsymbol{r})] = \frac{\delta E_{\mathrm{XC}}[n(\boldsymbol{r})]}{\delta n(\boldsymbol{r})} \tag{2.10}$$

2.1.2 Exchange-Correlation Functional

An appropriate form of the exchange-correlation (XC) energy E_{XC} should be provided for solving the KS equations. The XC energy is defined with the XC energy density per electron $\varepsilon_{\mathrm{XC}}[n(\boldsymbol{r})]$,

$$E_{\mathrm{XC}}[n(\boldsymbol{r})] = \int \varepsilon_{\mathrm{XC}}[n(\boldsymbol{r})]n(\boldsymbol{r})d\boldsymbol{r} \tag{2.11}$$

The $\varepsilon_{\mathrm{XC}}[n(\boldsymbol{r})]$ is the electrostatic interaction energy of an electron at $\boldsymbol{r}$ with XC hole density $n_{\mathrm{XC}}^{\mathrm{hole}}$ at $\boldsymbol{r}'$,

$$\varepsilon_{\mathrm{XC}}[n(\boldsymbol{r})] = \frac{1}{2}\int \frac{n_{\mathrm{XC}}^{\mathrm{hole}}(\boldsymbol{r},\boldsymbol{r}')}{|\boldsymbol{r}-\boldsymbol{r}'|} \tag{2.12}$$

Among various XC functionals, three types are widely used: the local density approximation (LDA), the generalized gradient approximation (GGA), and the hybrids.

The LDA is a simple method assuming a homogeneous electron gas (HEG) with same density.[67,68] The LDA depends only on the local density, and the XC energy is expressed as

$$E_{\mathrm{XC}}^{\mathrm{LDA}}[n(\boldsymbol{r})] = \int \varepsilon_{\mathrm{XC}}^{\mathrm{LDA}}[n(\boldsymbol{r})]n(\boldsymbol{r})d\boldsymbol{r} \tag{2.13}$$

where $\varepsilon_{\mathrm{XC}}^{\mathrm{LDA}}[n(\boldsymbol{r})]$ is the XC energy density per electron of a HEG. The calculation of $\varepsilon_{\mathrm{XC}}^{\mathrm{LDA}}$ is enhanced by interpolating the data from quantum Monte Carlo over wide range of densities.[69] The LDA can be used for the system where the charge density is relatively homogeneous. However, the LDA typically overestimates exchange energy E_{X} and underestimates correlation energy E_{C}, which results in problems where XC hole has local variations.

The GGA improves the accuracy by incorporating the gradient of the electron density for the systems varying the density.[70] The XC energy $E_{\mathrm{XC}}^{\mathrm{GGA}}$ is expressed using the additional variable of gradient of the electron $\nabla n(\boldsymbol{r})$ as:

$$E_{\mathrm{XC}}^{\mathrm{GGA}}[n(\boldsymbol{r})] = \int \varepsilon_{\mathrm{XC}}^{\mathrm{GGA}}[n(\boldsymbol{r}),\nabla n(\boldsymbol{r})]n(\boldsymbol{r})d\boldsymbol{r} \tag{2.14}$$

The GGA corrects the overbinding problem of LDA and yields accurate structural properties. Among various GGAs, the PBE[71] has been widely used due to their efficiency and accuracy for generous systems.

Advanced functional beyond GGA shows the improvements by incorporating additional variables such as higher order density gradient or nonlocal Hartree-Fock (HF) exchange energy.

The problem of GGA in strongly correlated systems can be mitigated by combining the HF method, which does not account for the correlation energy. The XC energy in hybrid functional is given by,

$$E_{\mathrm{XC}} = \alpha E_{\mathrm{x}}^{\mathrm{HF}} + (1-\alpha)E_{\mathrm{x}}^{\mathrm{GGA}} + E_{\mathrm{C}}^{\mathrm{GGA}} \tag{2.15}$$

where $E_{\mathrm{x}}^{\mathrm{HF}}$ is the HF exchange energy, $E_{\mathrm{x}}^{\mathrm{GGA}}$ is the GGA exchange energy, $E_{\mathrm{C}}^{\mathrm{GGA}}$ is the GGA correlation energy, and α is the mixing parameter determining the fraction of $E_{\mathrm{x}}^{\mathrm{HF}}$.

The GGA underestimates the band gap because GGA treats the ground state. The incorporation of HF exchange energy estimates a better band gap, since the self-interaction in the Hartree term is exactly removed by the $E_{\mathrm{x}}^{\mathrm{HF}}$. The GW methods based on the many-body perturbation theory result in more accurate band gap, which is discussed in section 2.1.3

2.1.3 GW Methods

The quasi-particle (QP) equation based on the many-body perturbation theory is

$$\left[-\frac{\hbar^2}{2m}\nabla^2 + V_{\mathrm{ext}}[\boldsymbol{r}] + V_{\mathrm{H}}[n(\boldsymbol{r})] + \int \sum(\boldsymbol{r},\boldsymbol{r}';\varepsilon_i)\, d\boldsymbol{r}'\right]\psi_i = \varepsilon_i\psi_i \tag{2.16}$$

where $\sum(\boldsymbol{r},\boldsymbol{r}';\varepsilon_i)$ is the self-energy operator, which is non-local and energy-dependent.[72,73] The eigenvalues of the equation correspond to the energy for electron addition or removal, and thus the band gap is obtained using a difference in QP energies. Using GW approximation, the self-energy operator is expressed in terms of the single-particle Green function G and the dynamically screened interaction W:[73]

$$\sum(\boldsymbol{r},\boldsymbol{r}';\varepsilon) \approx iG(\boldsymbol{r},\boldsymbol{r}';\varepsilon)W(\boldsymbol{r},\boldsymbol{r}';\varepsilon) \tag{2.17}$$

G and W can be expressed in terms of quasiparticle wavefunctions. In the simplest G_0W_0 method, the DFT wavefunctions and eigenvalues are used to calculate G and W, and the self-

energy operator is considered as a perturbation to the Kohn-Sham potential. Further updates to G and W can be performed for the QP equations.

2.1.4 Implementation

First-principles calculations were performed using the Vienna *Ab initio* Simulation Package (VASP).[74] Charge densities and wavefunctions were expanded in a plane wave basis set, while core-valence electron interactions were treated using the projector augmented wave (PAW) method.[75,76] Three different levels of theory were employed for the exchange-correlation energy: (i.) the semi-local generalized gradient approximation (GGA) of Perdew, Burke, and Ernzerhof (PBE),[71] (ii.) the hybrid functional of Heyd, Scuseria, and Ernzerhof (HSE06),[77,78] and, (iii.) quasi-particle (QP) calculations based on many-body perturbation theory (G_0W_0 method).[79,80] Occupancies were determined by a Gaussian smearing of width 0.1 eV, and the Brillouin zone was sampled with Monkhorst-Pack grids.[81]

2.2 Classical Molecular Dynamics

2.2.1 Principles of Molecular Dynamics

Molecular dynamics (MD) is a simulation method that determines the time evolution of interacting atoms by solving Newton's equation of motion,

$$\boldsymbol{F} = m\boldsymbol{a} = m\frac{d\boldsymbol{v}}{dt} = m\frac{d^2\boldsymbol{r}}{dt^2} \tag{2.18}$$

The force on each atom is evaluated using the negative gradient of potential U,

$$\boldsymbol{F} = -\nabla U(r) \tag{2.19}$$

The initial position, velocity, and net force on atoms are used to obtain the motion over time. New position at the next step $t + \Delta t$ is estimated using finite difference methods and this calculation is repeated using the estimated position as an input for the next movement of atoms. Velocity Verlet algorithm is one of the most popular methods, which calculates the position, velocity, and acceleration at the next step $t + \Delta t$ as[82]

$$\boldsymbol{r}(t + \Delta t) = \boldsymbol{r}(t) + \boldsymbol{v}(t)\Delta t + \frac{1}{2!}\boldsymbol{a}(t)\Delta t^2 = \boldsymbol{r}(t) + \boldsymbol{v}\left(t + \frac{\Delta t}{2}\right)\Delta t \tag{2.20}$$

$$\boldsymbol{a}(t + \Delta t) = \frac{\boldsymbol{F}(t + \Delta t)}{m} = -\frac{1}{m}\frac{dU[\boldsymbol{r}(t + \Delta t)]}{dt} \tag{2.21}$$

$$\boldsymbol{v}(t + \Delta t) = \boldsymbol{v}(t) + \frac{\boldsymbol{a}(t) + \boldsymbol{a}(t + \Delta t)}{2}\Delta t = \boldsymbol{v}\left(t + \frac{\Delta t}{2}\right) + \frac{1}{2}\boldsymbol{a}(t + \Delta t)\Delta t \tag{2.22}$$

As the time evolution, the atomic positions, forces, and energies can be used for further statistical analysis to examine the structural, mechanical, thermodynamic, and transport properties.

2.2.2 Force-Fields

Two types of empirical potentials are used to examine the static and dynamic properties of LLZO. The first force field is based on the bond valence (BV) method. Empirical relation between bond length and BV has been used to examine the ion transport in solid electrolytes.[83–85] The variation of an individual bond valence can be translated into the variation of a Morse-type interaction potential

$$E = D_0\{(\exp[\alpha(R_{\min} - R)] - 1)^2 - 1\} \tag{2.23}$$

$R_{\min}$ is given by

$$R_{\min} = R_0[0.9185 + 0.2285|\sigma_{\mathrm{A}} - \sigma_{\mathrm{X}}|] - b\ln(V_{\mathrm{id}}/N_{\mathrm{C}}) \tag{2.24}$$

where R_0 is the BV parameter, σ_{A} and σ_{X} are the absolute softness of the cation and anion, b is $1/\alpha$, V_{id} is the absolute value of nominal charge, and N_{C} is the preferred coordination number of the central ion. The dissociation energy D_0 is approximated for a wide range of cation as

$$D_0 = c \times 14.4 \frac{\left(V_{\mathrm{id,A}} V_{\mathrm{id,X}}\right)^{1/c}}{R_{\min}\sqrt{n_A n_X}} \times \frac{b^2}{2} \tag{2.25}$$

where $c = 1$ if a cation, A, is an s or p block element, or $c = 2$ if A is a d or f block element. n_A and n_X represent the principal quantum numbers of cation A and anion X. The BV parameters for 132 cation types in oxides are provided by Adams *et* al.[83]

Coulomb repulsion terms are screened by an error function

$$E_{\mathrm{Coulomb}} = 14.4 \frac{q_A q_X}{R_{\mathrm{A-X}}} efrc\left(\frac{R_{\mathrm{A-X}}}{\rho_0}\right) \tag{2.26}$$

where q_A and q_X are fractional charges, $R_{\mathrm{A-X}}$ is the distance between cation and anion, and ρ_0 is the screening factor derived from the covalent radii of cation and anion. The q_A and q_X are estimated based on

$$q_{\mathrm{Ai}} = \frac{V_{\mathrm{id,Ai}}}{\sqrt{n_{\mathrm{Ai}}}} \sqrt{\frac{\sum_j \frac{V_{\mathrm{id,Xj}} N_{\mathrm{Xj}}}{\sqrt{n_{\mathrm{Xj}}}}}{\sum_i \frac{V_{\mathrm{id,Ai}} N_{\mathrm{Ai}}}{\sqrt{n_{\mathrm{Ai}}}}}} \tag{2.27}$$

$$q_{\mathrm{Xj}} = \frac{V_{\mathrm{id,Xj}}}{\sqrt{n_{\mathrm{Xj}}}} \sqrt{\frac{\sum_i \frac{V_{\mathrm{id,Ai}} N_{\mathrm{Ai}}}{\sqrt{n_{\mathrm{Ai}}}}}{\sum_j \frac{V_{\mathrm{id,Xj}} N_{\mathrm{Xj}}}{\sqrt{n_{\mathrm{Xj}}}}}} \tag{2.28}$$

where N_{Ai} (N_{Xj}) refer to the occupancies of the ith cation A_{i} (jth cation X_{j}) in the structure.

The second force field is based on the classical Born description. Long-range Coulombic interaction is given by Coulomb's low

$$U_{\mathrm{ij}} = \frac{q_i q_j}{4\pi\epsilon_0 r_{\mathrm{ij}}} \tag{2.29}$$

where q_i and q_j are the charges, ϵ_0 is the permittivity, and r_{ij} is the distance between the ions. The fractional effective charges were used based on a partially ionic model ($q_{\mathrm{eff}} = 0.7 q_{\mathrm{norminal}}$).

The Buckingham potential was used for the short-range interactions,

$$\phi_{\mathrm{ij}} = A_{\mathrm{ij}} \exp\left(-r_{\mathrm{ij}}/\rho_{\mathrm{ij}}\right) - C_{\mathrm{ij}}/r_{\mathrm{ij}}^6 \tag{2.30}$$

where A_{ij}, ρ_{ij}, and C_{ij} are empirically derived parameters for interacting ions. The cutoff distance for the short-range interaction was set to 10.5 Å. All classical molecular dynamics simulations were performed using LAMMPS.[86]

Chapter 3 Electronic Properties and Electrochemical Stability

3.1 Introduction

The electrochemical window (EW) determines an electrolyte's resistance to undesirable electronic transport, and by extension, controls phenomena such as short-circuiting and self-discharge. Accurate estimates do not yet exist for basic EW-related properties of LLZO such as its band gap and the positions of its band edges. These properties are now routinely examined in the assessment of liquid electrolytes,[87–89] but have not been thoroughly explored for solid electrolytes. Moreover, experimental measurements of the LLZO EW often employ transient techniques such as cyclic voltammetry (CV),[45] which can be insufficient to determine electronic transport properties. Lacking these data, it is unclear whether the promising performance reported for LLZO represents an intrinsic property of the bulk phase, or is instead a consequence of fortuitous "kinetic stabilization" arising from interfacial reactions with the electrodes.[14,90]

The study presented in this chapter aims to close this knowledge gap by assessing the EW of LLZO-based solid electrolytes. First-principles calculations were used to predict the density of states (DOS), band gap, and absolute positions of the band edges for LLZO. The calculations indicated that the conduction band minimum in LLZO is predicted to lie slightly above Li/Li^+, suggesting moderate stability against electron injection (n-type conductivity) from the Li anode.

The position of the valence band maximum (VBM) in bulk LLZO further supports the observation of limited electronic transport at high (positive) voltages: p-type conduction arising from hole injection into the valence band is hindered by the low energy of the VBM, which is ~4 V more positive than the Li/Li^+ redox potential.

3.2 Methodology

3.2.1 Bandstructure and Density of States

First-principles calculations were performed using three different levels of theory were employed: (i.) GGA-PBE,[71] (ii.) the hybrid functional of HSE06,[77,78] and, (iii.) G_0W_0 method.[79,80] Bandstructure and density of states (DOS) calculations were performed on the primitive unit cell (96 atoms) of LLZO. The convergence criterion for electronic self-consistency was set to 10^{-5} eV. Electronic occupancies were determined using Gaussian smearing with an energy width 0.05 eV for calculations of the bandstructure, DOS, and the electrostatic potential. A larger smearing of 0.1 eV was used for all other calculations (geometry optimization, surface energies, *etc*.).

Ionic relaxations for the conventional/primitive unit cells and surface slabs were performed at the GGA-PBE level of theory. Atomic positions were relaxed until all forces were less than 0.03 eV/Å. In these cases, an energy cutoff of 600 eV was used for the plane wave basis. Monkhorst-Pack[81] k-point grids with a $2 \times 2 \times 2$ density were used for calculations on the bulk cells; surface slabs used Gamma-centered grids with a $2 \times 2 \times 1$ sampling density.

Calculations performed on the conventional unit cell of LLZO adopted the experimental cubic crystal structure.[36] Li was randomly distributed on the partially-occupied 24d and 96h sites on the Li-sublattice using a procedure that minimizes occupancy of electrostatically-unfavorable first nearest-neighbor sites.[36] Energy differences were negligible (<1.5 meV/atom) among

several structures generated in this manner. The structure having the lowest total energy was used in subsequent calculations. The resulting partial occupancies of the 24d and 96h sites was 0.542 and 0.448, respectively, which is equivalent to 13 and 43 atoms in the LLZO unit cell. These occupancies are similar to the experimental values of 0.564 and 0.442.[36] The bulk lattice parameter was obtained by fitting total energy *vs.* volume data to the Murnaghan equation of state,[91] resulting in a calculated value of 13.026 Å. This is similar to the experimental measurement of 13.0035 Å. For calculations on the primitive cell the fractional occupancy of the 24d (96h) sites was 0.583 (0.438), which is equivalent to 7 (21) Li atoms in the cell.

Due to the expense of hybrid functional calculations, combined with the large size of the LLZO cell, calculations performed with the HSE06 functional used a lower energy cutoff of 450 eV. Bandstructure calculations used a self-consistent charge density evaluated at the Γ-point, while k-point grids up to 2 × 2 × 2 (8 irreducible k-points) were used for DOS calculations. Non-self-consistent G_0W_0 calculations were performed using input from prior self-consistent PBE and HSE06 calculations (referred to as PBE+G_0W_0 and HSE06+G_0W_0, respectively). DOS calculations were conducted using an energy cutoff of 450 eV in combination with Γ-centered k-point grids with densities as large as 2 × 2 × 2 (8 irreducible k-points). Band gaps were converged with respect to the number of bands: 720 bands were used for PBE+G_0W_0 calculations, with 840 used for HSE06+G_0W_0.

3.2.2 Band Edge Positions

Band edge positions were determined using the HSE06 functional by aligning the planar-averaged electrostatic potential in bulk LLZO with that in (100) and (110)-oriented surface slabs.[92] Several (100) and (110)-oriented surface slabs based on the conventional unit cell (192

atoms) with distinct surface compositions were used to establish the positions of the LLZO band edges. Atomic positions within the slabs were relaxed at the GGA-PBE level of theory, as mentioned above; subsequently, HSE06 calculations with a 450 eV cutoff (10^{-4} eV convergence criterion) were performed on these 'frozen' geometries.

The surface energies of the various LLZO surface models were calculated according to:

$$\gamma = \frac{1}{2A}\left(G_{LLZO}^{slab} - n_{LLZO}^{f.u.}\mu_{LLZO}^{bulk} - \Sigma n_i \mu_i\right) \quad (3.1)$$

Here G_{LLZO}^{slab} is the total energy of the slab, $n_{LLZO}^{f.u.}$ is the integer number of stoichiometric formula units in the slab, μ_{LLZO}^{bulk} is the energy of one formula unit of bulk LLZO, n_i is the number of atoms of type i in the slab in excess of the stoichiometric amount, and μ_i is the chemical potential of element i.

Prior computational study[93] found that at 0 K (neglecting vibrational and entropy effects) LLZO is weakly meta-stable with respect to decomposition into Li_8ZrO_6, $Li_6Zr_2O_7$, and La_2O_3. Indeed, our calculations indicate that the decomposition of LLZO into these phases is exothermic by only 5.8 meV/atom. Presumably the inclusion of other contributions to the free energies of these phases would narrow this energy gap, or reverse its sign.

Recent DFT calculations[90,94] show that LLZO is stable between 0.05 and 2.91 V vs Li/Li^+ upon reduction and oxidation, respectively. The decomposition energy for the reduction at 0 V is 9 meV/atom, suggesting the stability of LLZO against Li metal anode. LLZO also can be stable with the cathode operating voltages ~ 4 V vs. Li/Li^+, due to the large over-potential for the oxidation of LLZO and kinetic protections of decomposition phases.

Therefore, Li_8ZrO_6, $Li_6Zr_2O_7$, and La_2O_3 are assumed to be in equilibrium with LLZO between 0 and 4 V vs. Li/Li^+. The chemical potentials of the elements comprising LLZO were

determined using these phases. This yields a series of three equations relating the chemical potentials to the total energies of the phases:

$$E(La_2O_3) = 2\,\mu_{La} + 3\,\mu_O \tag{3.2}$$

$$E(Li_6Zr_2O_7) = 6\,\mu_{Li} + 2\,\mu_{Zr} + 7\,\mu_O \tag{3.3}$$

$$E(Li_8ZrO_6) = 8\,\mu_{Li} + \mu_{Zr} + 6\,\mu_O \tag{3.4}$$

The chemical potential of lithium, μ_{Li}, was obtained assuming local equilibrium with the electrodes,

$$\mu_{Li}(\Phi) = \mu_{Li,BCC} - e\Phi \tag{3.5}$$

where $\mu_{Li,BCC}$ is the chemical potential of BCC Li, e is the elementary charge, and Φ is the electrostatic potential referenced to Li anode.

A total of twelve LLZO surface slabs were examined as candidate systems for evaluation of the electrostatic potential, as shown in Figure 3.1 and 3.2. The surfaces having the lowest surface energy in each of the (100) and (110) directions were used to determine the positions of the LLZO band edges. These calculations employ the planar-averaged electrostatic potential, ϕ, within, and outside of, an LLZO slab. The potential corrugations in the central region of the slab, ϕ_{bulk}, mimic those in bulk LLZO, while the asymptotic behavior of the potential far from the slab establishes the vacuum level, ϕ_{vac}.[92] Knowledge of ϕ_{vac} allows for positioning of the absolute Li/Li^+ level (i.e., Li Fermi level). Similarly, the position of the band gap center (BGC) in bulk LLZO can be determined by overlaying ϕ_{bulk} from a bulk LLZO cell onto ϕ_{bulk} from the surface slab. Finally, the absolute positions of the CBM and VBM in bulk LLZO are given by BGC $\pm$ $\frac{E_{gap}}{2}$, where E_{gap} is the band gap evaluated from the present G_0W_0 calculations.

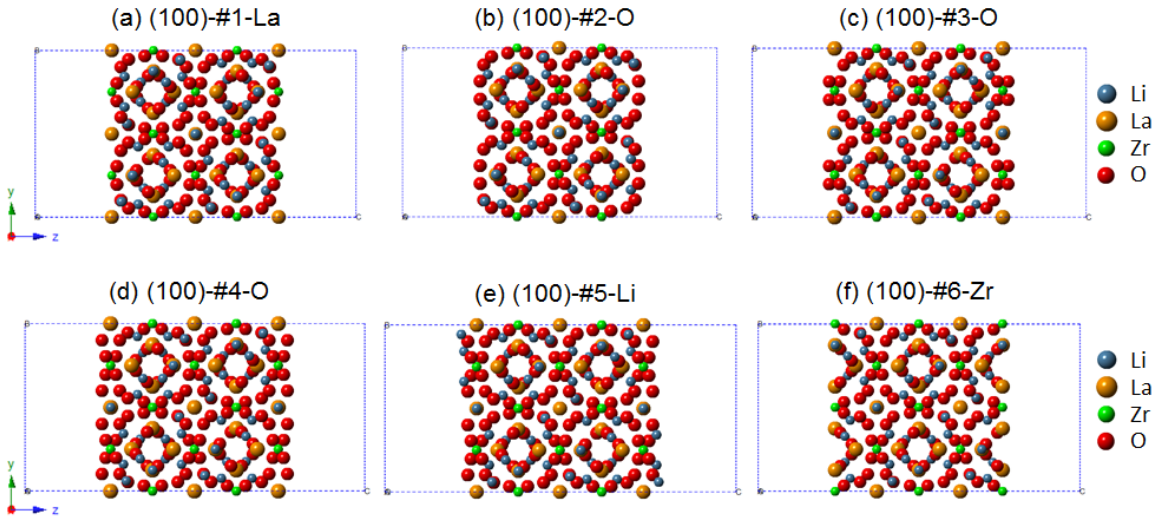

Figure 3.1 Illustration of the six LLZO (100) slabs used in surface energy calculations. The slab name indicates the predominant composition of the surface. (a) La-terminated $Li_{58}La_{28}Zr_{20}O_{96}$, (b) O-terminated $Li_{54}La_{20}Zr_{12}O_{96}$, (c) O-terminated $Li_{59}La_{28}Zr_{20}O_{104}$, (d) O-terminated $Li_{59}La_{28}Zr_{20}O_{112}$, (e) Li-terminated $Li_{67}La_{28}Zr_{20}O_{112}$, and (f) Zr-terminated $Li_{58}La_{28}Zr_{20}O_{96}$.

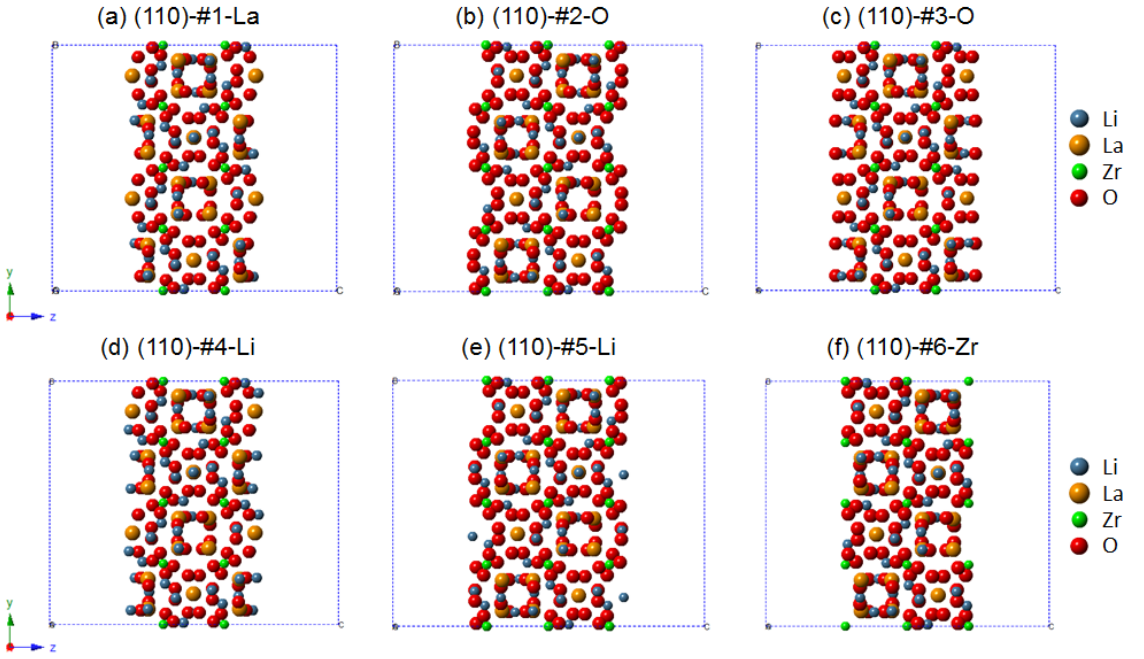

Figure 3.2 Illustration of the six LLZO (110) slabs used in surface energy calculations. The slab name indicates the predominant composition of the surface. (a) La-terminated $Li_{58}La_{28}Zr_{16}O_{96}$, (b) O-terminated $Li_{59}La_{24}Zr_{24}O_{120}$, (c) O-terminated $Li_{66}La_{28}Zr_{16}O_{112}$, (d) Li-terminated $Li_{66}La_{28}Zr_{16}O_{96}$, (e) Li-terminated $Li_{65}La_{24}Zr_{24}O_{120}$, and (f) Zr-terminated $Li_{56}La_{24}Zr_{24}O_{96}$.

3.3 Results and Discussion

3.3.1 Electronic Properties

Figure 3.3 shows the calculated band gap and density of states of LLZO evaluated using three levels of theory: PBE, HSE06 and G_0W_0. Band structure plots are reported in Figure 3.2 for the PBE and HSE06 functionals. The partial DOS evaluated at the PBE+G_0W_0 and HSE06+G_0W_0 levels of theory is plotted in Figure 3.3. Band gaps calculated at the HSE06 level of theory are approximately 5.79 eV, while quasi-particle calculations based on the G_0W_0 method yield slightly larger gaps of 6.07 (PBE+G_0W_0) and 6.42 (HSE06+G_0W_0) eV. GW calculations – in particular those based on HSE06 input wavefunctions – typically yield highly accurate band gaps that are in better agreement with experimental photoemission data than those predicted by hybrid functionals.[95] These factors lead us to conclude that the band gap of LLZO is best approximated by the HSE06+G_0W_0 gap of 6.4 eV. The large band gap reported here is consistent with a large

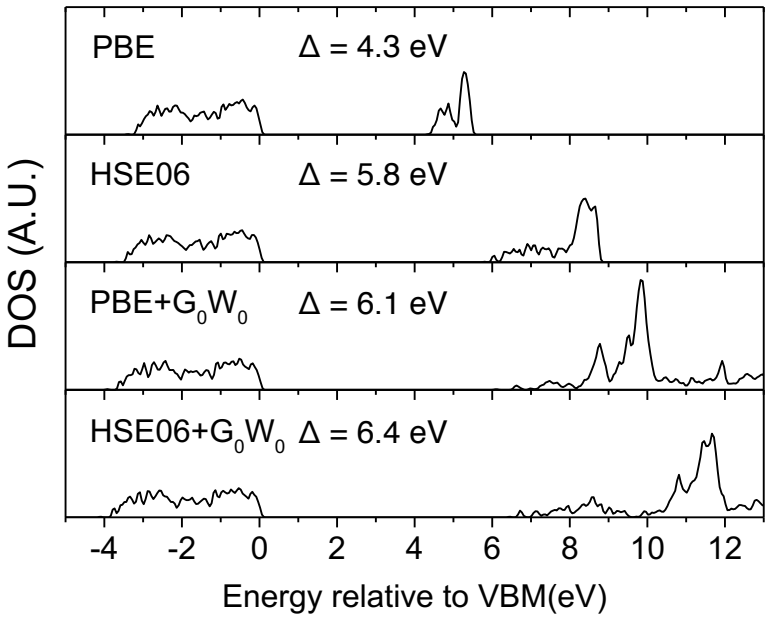

Figure 3.3 Total density of states (DOS) for LLZO as a function of calculation method. The energy scale is set such that a value of zero corresponds to the energy of the valence band maximum.

optical gap of 5.5 eV and CV measurements[61] suggesting that LLZO should be compatible with high voltage cathodes.

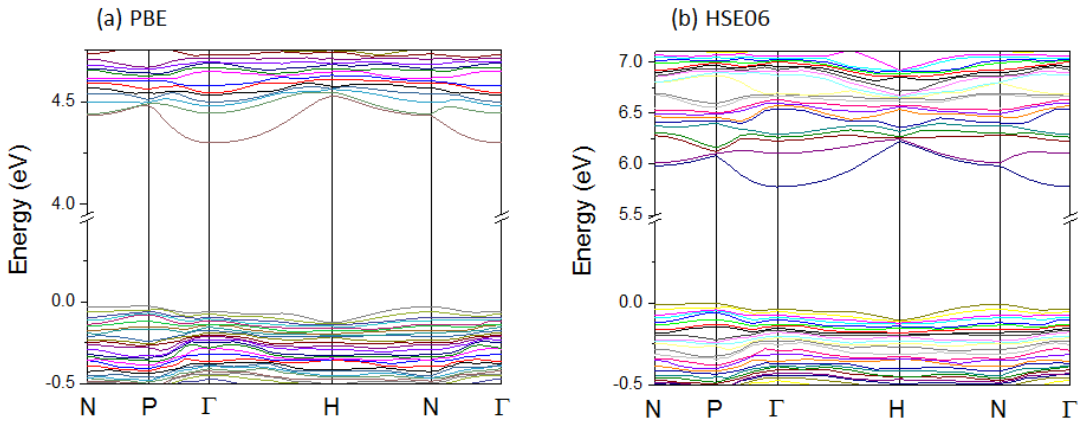

Figure 3.4 Calculated band structure for LLZO evaluated using the (a) PBE and (b) HSE06 functionals.

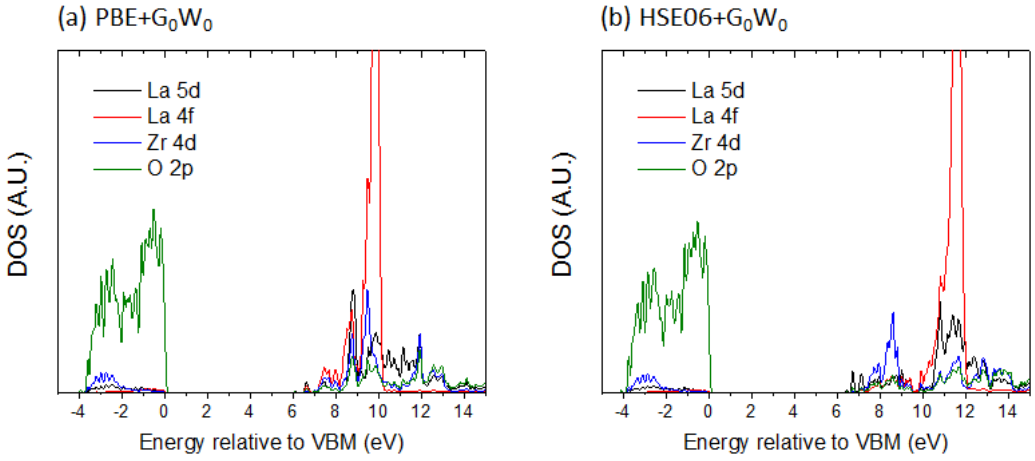

Figure 3.5 Calculated partial DOS for LLZO evaluated using (a) PBE+G_0W_0 and (b) HSE06+G_0W_0.

3.3.2 Electrochemical Window

LLZO has a sufficiently large band gap (6.4 eV) to enable its use with high voltage electrodes, in principle allowing for an all solid-state cell with OCV > 6 V. However, it is important to recognize that a large band gap represents a necessary, but not sufficient condition for a viable electrolyte; the positions of the band edges relative to the electrochemical potentials of the electrodes are also critical. More specifically, a solid electrolyte will be stable against electron injection if the CBM lies at a higher energy (i.e., more negative potential) than the Fermi level of the negative electrode: E(CBM) > η_-. Similarly, stability against hole injection from the positive electrode requires that the electrolyte's VBM have a lower energy (i.e., be positioned at a more positive potential) than the redox level of the positive electrode: E(VBM) < η_+.

To assess the resistance of LLZO to charge injection and undesirable electronic transport, the absolute positions of the LLZO band edges were evaluated computationally.[92] Electrochemical window of LLZO was evaluated assuming two local equilibria with a Li metal anode and cathode as shown in Figure 3.6. Different local equilibria at the two interfaces (with the anode and with the cathode) are illustrated in the Figure 3.6.

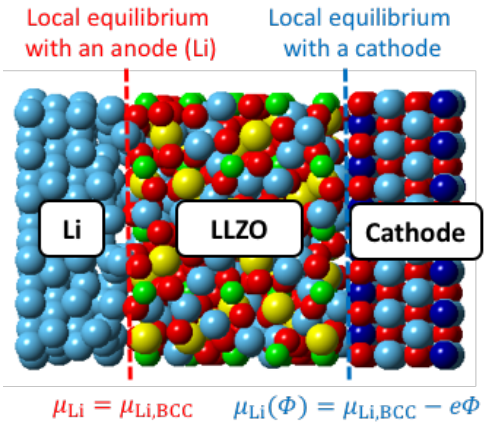

Figure 3.6 Li/LLZO/Cathode structure with different local equilibria present at the two interfaces.

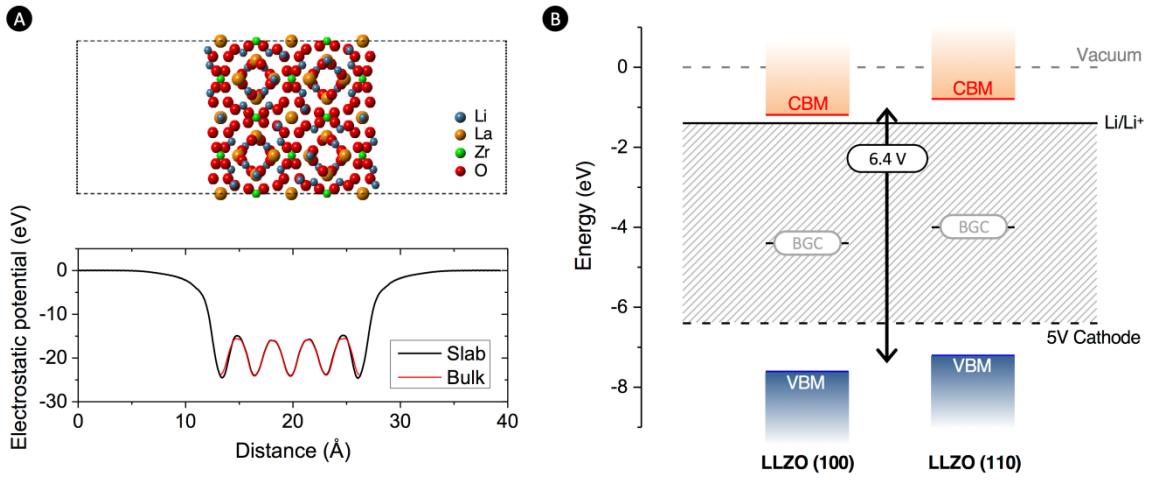

Figure 3.7 (a) The lowest energy (100) slab of LLZO (top) and the associated planar-averaged electrostatic potential (bottom panel, black curve). The electrostatic potential from a bulk supercell is overlaid (red data). (b) Position of the conduction band minimum (CBM) and valence band maximum (VBM) of LLZO for the lowest energy (100) and (110) surface slabs.

At first, band edge positions were evaluated assuming local equilibrium with a Li metal anode. The most stable surfaces – (100) slab #5 and (110) slab #4 – were Li terminated and had nearly identical surface energies of 0.84 and 0.85 J/m^2, respectively. Figure 3.7(a) shows the lowest energy (100) surface along with an overlay of the planar-averaged electrostatic potentials, ϕ, evaluated from the slab and bulk cells. These data were used to determine the absolute positions of the CBM and VBM in bulk LLZO, shown in Figure 3.7(b), for both the lowest energy (100) and (110) slabs.

Fig. 3.7(b) demonstrates that the calculated band edge positions satisfy the electrochemical stability criteria, E(CBM) > η_- , regardless of the slab model used. LLZO should be susceptible to electron injection from the Li negative electrode.

Band edge positions were also evaluated assuming local equilibrium with a cathode as illustrated in Figure 3.6. Six slabs from each of (100) and (110) orientations in Figure 3.2 were examined for band edge calculations using the chemical potential of Li described in Eq. (3.5).

Table 3.1 Calculated surface energy for (100) and (110) slabs of LLZO.

	(100) surface						(110) surface					
Φ (vs Li/Li$^+$)	#1-La	#2-O	#3-O	#4-O	#5-Li	#6-Zr	#1-La	#2-O1	#3-O2	#4-Li1	#5-Li2	#6-Zr
0	1.44	5.06	1.19	1.01	0.84	1.35	0.90	2.53	1.81	0.85	1.95	1.35
1	2.86	3.64	1.89	0.97	1.17	2.76	1.36	2.09	1.47	1.58	1.72	2.42
2	4.28	2.22	2.60	0.92	1.50	4.18	1.83	1.66	1.14	2.32	1.49	3.49
3	5.69	0.81	3.31	0.87	1.84	5.60	2.30	1.23	0.80	3.05	1.25	4.56
4	7.11	-0.61	4.02	0.82	2.17	7.01	2.77	0.79	0.47	3.79	1.02	5.62

The surface energies of twelve LLZO slabs were obtained as a function of electrostatic potential, which are summarized in Table 3.1. At high potential greater than 3 V vs. Li/Li$^+$, the lowest surface energy slabs were oxygen terminated (100)-#2-$Li_{54}La_{20}Zr_{12}O_{96}$ and (110)-#3-$Li_{66}La_{28}Zr_{16}O_{112}$. These slabs also showed the lowest surface energy when the LLZO is in the local equilibrium with oxygen gas at T = 300 K. The unphysical surface energy at 4 V vs. Li/Li$^+$ for (100)-#2 can be explained by the oxidation of LLZO. These two slabs ((100)-#2 and (110)-#3) were used for the electrostatic potential calculations. The vacuum region of slabs was 12 Å for the surface energy calculations and 24 Å for the electrostatic potential calculations. A thicker slab ($Li_{92}La_{40}Zr_{24}O_{160}$) than was used to evaluate the electrostatic potential for (110) -#3 slab.

The electrostatic potential in the slab cells were used to position the electrostatic potential of bulk LLZO with respect to the vacuum level, as shown in Figure 3.8. The electrostatic potential of the bulk LLZO is shifted to match that from the bulk-like center region of the slab. Based on the band gap of 6.4 eV from the quasiparticle calculations (HSE06+G_0W_0), the absolute position of the VBM was found for both the lowest energy (100) and (110) slabs. For the stability against oxidation by the cathode, the VBM of LLZO has a lower energy than the redox level of the cathode.

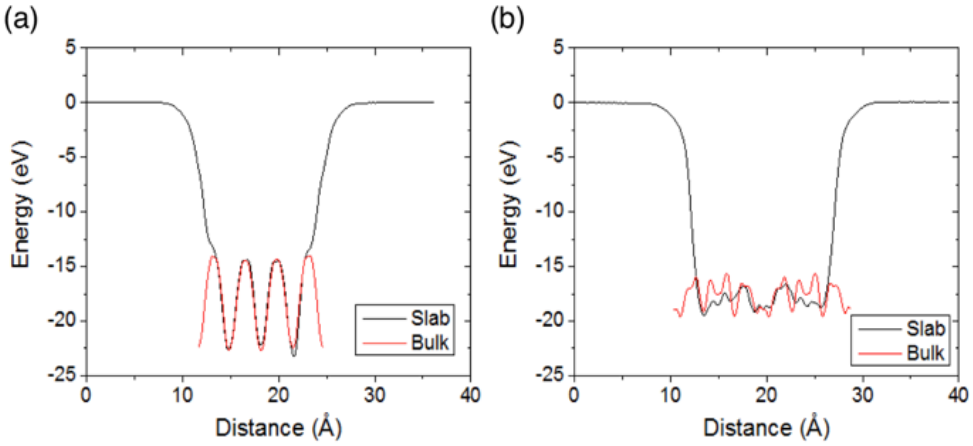

Figure 3.8 Planar averaged electrostatic potential for bulk LLZO overlaid onto that for (a) (100)-#2-O-terminated $Li_{54}La_{20}Zr_{12}O_{96}$ and (b) (110)-#3-O-terminated $Li_{66}La_{28}Zr_{16}O_{112}$ slabs.

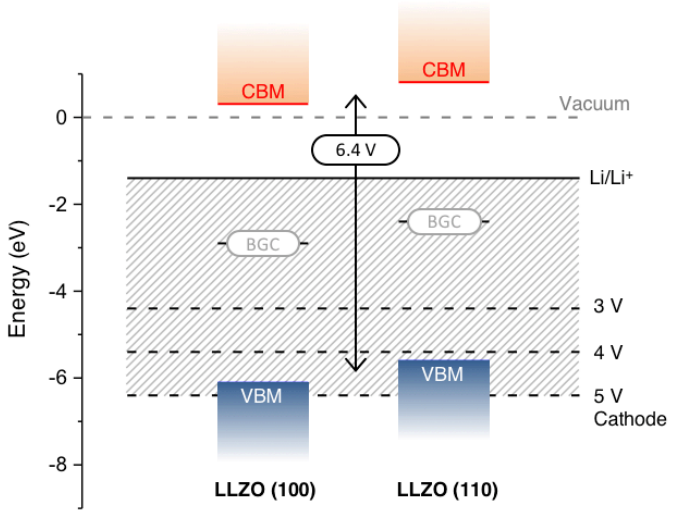

Figure 3.9 The absolute position of the CBM and VBM of LLZO for the lowest energy (100) and (110) surface slabs relative to the Li/Li^+ level assuming local equilibrium with a high potential (>3 V) cathode.

In Figure 3.9, the locations of the VBM for (100)-#2 and (110)-#3 slabs show that LLZO is marginally stable relative to ~4 V vs. Li/Li^+ cathodes such as LCO and NMC. This result can explain the decomposition of LLZO contacting with LNMO which has a higher redox potential of 4.7 V vs. Li/Li^+.[7,17,18] The CBM position in Figure 3.9 was obtained by assuming the local equilibrium with a Li metal, which indicated the reductive stability between LLZO and Li anode.

While the positions of the band edges suggest a suitably-wide EW, a few caveats apply. First, as shown by the (100)-oriented slab, the energy difference between the CBM and the Li/Li^+ level can be modest, only 0.2 eV in this case. Second, the present band edge model depicts LLZO as a fictitious "isolated" solid: that is, it omits interfacial effects that will be present in a real electrochemical cell and which can potentially narrow or expand the effective EW.[89,90] For example, *chemical* reactions at LLZO/electrode interfaces could yield thin product layers that "kinetically stabilize" LLZO by preventing further redox reactions from occurring.[90,96] Similarly, *electrochemical* oxidation or reduction at these interfaces could be self-limiting due to the formation of electrically passivating films. Such processes would be similar to those associated with SEI formation in conventional Li-ion batteries.[1,14] Accounting for these effects will require modeling the full interface at the GW level of theory. Such a calculation is a challenge due to the large size of the LLZO unit cell and the expense of these calculations.

3.4 Conclusions

First-principles calculations were performed to characterize the electrochemical window of the LLZO. The EW determines an electrolyte's resistance to undesirable electronic transport, and, by extension, controls phenomena such as short-circuiting and self-discharge. The position of the EW also impacts electrochemical oxidation and reduction of LLZO by the electrodes; these

faradaic processes are generally the first step in subsequent (chemical) reactions at electrolyte/electrode interfaces.

DFT calculations reveal that LLZO is an excellent electronic insulator with the large band gap (6.4 eV from GW calculations). An evaluation of the absolute positions of the band edges lends further support to the observation of limited electronic transport in LLZO. The position of the VBM in bulk LLZO indicates that LLZO is stable against p-type conduction arising from hole injection up to ~4 V vs. Li/Li^+ cathodes. In addition, the conduction band minimum in LLZO is predicted to lie slightly above Li/Li^+, suggesting moderate stability against n-type charge injection from the anode. These data indicate that a wide EW window is an intrinsic property of LLZO, furthering its prospects for use in next-generation batteries.

Chapter 4 Impact of Surface Contamination

4.1 Introduction

LLZO is moderately unstable against air. During air exposure, a Li_2CO_3 layer forms on the surface of LLZO, which can potentially affect the interfacial resistance with electrodes.[46,47] The study presented in this chapter aims to clarify the impact of air exposure on the LLZO surface chemistry and the Li-LLZO interfacial resistance.

Density functional theory (DFT) was used to investigate the reaction between LLZO and air. Previous DFT calculations examined the carbonation of LLZO via formation of LiOH or by direct reaction of LLZO with CO_2.[47] The present study takes a different approach by exploring a hydration/carbonation reaction pathway that involves Li^+/H^+ ion exchange; such ion exchange has been demonstrated to be facile, for example, in aqueous environments.[97,98] Our DFT results indicate that the Li^+/H^+ ion exchange pathway is a thermodynamically favorable route for the formation of a Li_2CO_3 layer on the surface of LLZO.

The formation of contamination layers can potentially increase the Li-LLZO interfacial resistance. The Li wettability of LLZO is predicted as a means to rationalize the observation of high interfacial resistance in the presence of a contamination layer. The contact angle of Li on LLZO, Li_2CO_3, and LiOH was evaluated using DFT calculations. Calculations indicate that Li

strongly wets clean LLZO, but not Li_2CO_3 and LiOH, which is consistent with contact angle measurements.[63] The Li wetting is significantly enhanced upon removal of the surface contamination layers.[63]

The reaction of LLZO in humid air can proceed via the protonation of LLZO.[46,62] The present DFT results show that Li^+/H^+ ion exchange is thermodynamically favorable for all proton compositions up to the complete exchange of all Li^+ ions.[62] LLZO is also reported to take H^+ when immersed in water.[97] Recent classical MD simulations showed that the major level of exchange of protons (~60 %) in LLZO decreases the Li ion conductivity.[98] The present study used a different approach by performing *Ab initio* molecular dynamics (AIMD) calculations to examine the transport properties of protonated LLZO. Li^+ and H^+ ion diffusivity and conductivity for pure and H-doped LLZO cells were predicted using AIMD.

4.2 Methodology

4.2.1 Thermodynamic Driving Force of the Reaction

The thermodynamics of the hydration and carbonation of LLZO were examined using first-principles calculations. The convergence criterion for the electronic self-consistency loop was set to 10^{-5} eV, and ionic relaxations were converged to a force tolerance of less than 0.03 eV.$Å^{-1}$. An energy cut-off 600 eV was used for the plane wave basis and the Brillouin zone was sampled using the Monkhorst−Pack scheme.[81] A 2 × 2 × 2 k-point grid was used for LLZO, and 12 × 12 × 12 k-point mesh was used for crystalline LiOH, Li_2O, and Li_2CO_3.

Calculations on hydrogen-doped LLZO were performed by substituting hydrogen atoms for selected Li atoms. A prior experimental study of proton exchange in LLZO reported that proton substitution preferentially occurs on the 96h sites.[97,99] Present DFT calculations are

consistent with the site preference observed experimentally: at low proton concentrations (2% and 9% Li^+/H^+ exchange) 96h sites are weakly favored over 24d sites by 1 to 8 meV per atom. At higher concentrations (~ 63% Li^+/H^+ exchange) the preference for the 96h sites increases to ~20 meV per atom.

The molecular species H_2O and CO_2 were simulated within cubic simulation cells with dimensions of 8 Å; crystal structures for LiOH, Li_2O, and Li_2CO_3 were taken from experimental data. The optimal lattice parameters for all computational cells were obtained by fitting total energy *vs.* volume data to the Murnaghan equation of state.[91]

The Gibbs free energies of gas and liquid phases were obtained using equations (4.1) and (4.2):

$$\text{Gas phase: } G(T) = E^{\mathrm{DFT}}_{0\mathrm{K(g)}} + \Delta H(T) - TS^{\mathrm{expt}}_{\mathrm{(g)}}(T) \tag{4.1}$$

$$\text{Liquid phase: } G(T) = E^{\mathrm{DFT}}_{0\mathrm{K(g)}} + \Delta H(T) - \Delta H^{\mathrm{expt}}_{\mathrm{vap}}(T) - TS^{\mathrm{expt}}_{\mathrm{(l)}}(T) \tag{4.2}$$

here $E^{\mathrm{DFT}}_{0\mathrm{K(g)}}$ is the total energy of an isolated gas phase molecule at zero Kelvin, $\Delta H(T)$ is the enthalpy difference for the molecule associated with a temperature change between 0 K and a given temperature T, $S^{\mathrm{expt}}_{\mathrm{(i)}}$is the experimental gas (i=g) or liquid (i=l) phase entropy at temperature T,[100] and $\Delta H^{\mathrm{expt}}_{\mathrm{vap}}(T)$ is the enthalpy of vaporization. The ideal gas approximation was used to estimate the enthalpy difference, $\Delta H(T) \approx nk_{\mathrm{B}}T$, where n is 7/2 for linear molecules (i.e., CO_2) and 4 for nonlinear molecules (i.e., H_2O), respectively. The pressure was set to 1 atm. Finally, the Gibbs free energies of solids were approximated as the DFT total energy, $G \approx E^{\mathrm{DFT}}_{0\mathrm{K}}$.

4.2.2 Work of Adhesion and Wetting Angle

First-principles calculations were performed using density functional theory (DFT) with the GGA-PBE as the exchange correlation energy. For LiOH, van der Waals-aware density functional (vdW-DF2)[101] was additionally used to describe the weak interaction between LiOH (001) layers. An energy cutoff of 450 eV was used for the plane wave basis. The Brillouin zone was sampled using the Monkhorst-Pack scheme,[81] with 3×3×1, 4×4×1, and 4×4×1 k-point meshes used for the Li-LLZO, Li-Li_2CO_3, and Li-LiOH interfaces, respectively. The convergence criterion for the electronic self- consistency loop was set to 10^{-5} eV, while atomic positions were relaxed until atomic forces were less than 0.05 eV/Å.

A (001) Li slab with 20 layers was used to calculate the surface energy of Li, which resulted in 0.452 J m^{-2}. The Li-LLZO, Li-Li_2CO_3, and Li-LiOH interfaces were assembled using geometries that minimize interfacial strain; periodic boundary conditions in directions parallel to the interfacial plane were accommodated by adjusting the lattice constants of Li to match the dimensions of LLZO, Li_2CO_3, or LiOH. A vacuum layer of 8 Å was included in the interface supercells; each supercell contained one interface.

The interfacial distance was determined by rigidly displacing the two slabs along the interface normal, and fitting the resulting energy versus displacement data to the Universal Binding Energy Relation (UBER).[102] This procedure resulted in minimum-energy interfacial distances of 1.96, 3.04, and 2.32 Å for Li-LLZO, Li-Li_2CO_3, and Li-LiOH, respectively. Ionic relaxations were then performed for the three interfaces starting from interfacial separations predicted by the UBER fit. For the Li-LLZO interface, which had the largest supercell size (570 atoms), atoms in the "back" half of each slab (i.e., the portion farthest from the interface) were fixed at their bulk-like positions. The Li-Li_2CO_3 and Li-LiOH interfaces were fully relaxed

without fixing any atom positions. Testing on these two systems revealed that the work of adhesion was not strongly influenced by the presence/absence of these constraints.

The optimization of the translation state within the interfacial plane and the interfacial distance for the Li−LLZO interface are shown in Figure 4.1, respectively. Contour plots of W_{ad} were obtained by translating the Li slab among many configurations at a constant interfacial distance. The lowest interface in the contour plot was then used to calculate interfacial distance by fitting to the UBER.

The wetting angle, θ, was calculated by combining the Young-Dupré equation, $W_{ad} = \sigma_{Li}(1 + \cos\theta)$, with DFT calculations of the interfacial work of adhesion, W_{ad}, and the surface energy of Li, σ_{Li} = 0.45 J/m^2. Using the Li/LLZO interface as an example, W_{ad} is evaluated as: $W_{ad} = E_{int} - E_{Li\text{-}slab} - E_{LLZO\text{-}slab}$. Here, E_{int} is the energy of the interface cell and $E_{X\text{-}slab}$ refers to the energy of an isolated Li (X = Li) or LLZO slab (X = LLZO).

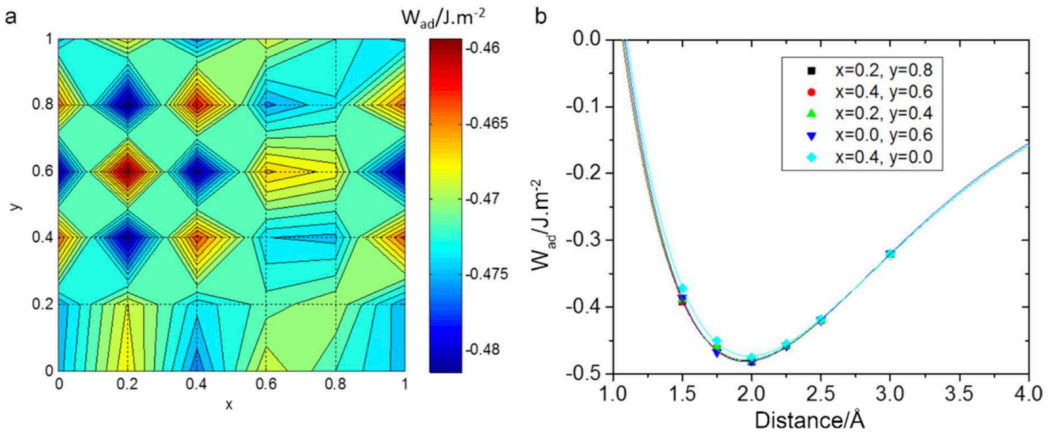

Figure 4.1 Optimization of the translation state within the interfacial plane and the interfacial distance for the Li-LLZO interface: a) contour plot of W_{ad} as a function of translation state for the Li slab relative to the LLZO slab using a 5×5 grid with a constant interfacial distance of 2 Å. b) W_{ad} as a function of interfacial distance between slabs fitted by the UBER for the five lowest W_{ad} interfaces identified in the contour plot of panel (a)

4.2.3 Li^+ and H^+ Ion Transport

AIMD calculations were performed to characterize Li^+ and H^+ diffusivity in pure and H-doped LLZO cells. Three different proton concentrations were used for H-doped LLZO cells: (i) $Li_{6.375}H_{0.625}La_3Zr_2O_{12}$ (5H-LLZO, 8.9 %) for minor contamination, (ii) $Li_{2.625}H_{4.375}La_3Zr_2O_{12}$ (35H-LLZO, 63 %) for major contamination, and (iii) $H_7La_3Zr_2O_{12}$ (56H-LLZO, 100 %) for full exchange. The 5 and 35 Li ions on 96h sites in unit LLZO cell were randomly substituted by proton for 5H-LLZO and 35H-LLZO, respectively. Due to the expense of AIMD calculations, a lower energy cutoff of 400 eV and gamma point-only sampling of the Brillouin zone were used. Following initial ionic relaxations, AIMD calculations were conducted on the pure and H-doped LLZO unit cells using a time step of 2 fs for pure LLZO and 1 fs for H-doped LLZO. The cells were heated at a rate of 500 K/ps and subsequently equilibrated for 5 ps at one of several target temperatures, which ranged from 700 to 1000 K. Finally, 40 ps of AIMD were performed in the NVT ensemble to collect diffusion data.

The diffusion coefficient was obtained from the ensemble-averaged mean squared displacement (MSD) over a time t,

$$D = \frac{1}{2dt}\langle[\mathbf{r}(t + t_0) - \mathbf{r}(t_0)]^2\rangle \tag{4.3}$$

where d is the dimensionality of the system, t_0 is the initial time, and the angled brackets indicate an average over all Li^+ ions. The ionic conductivity, σ, was derived using the Nernst−Einstein equation,

$$\sigma = \frac{(ze)^2 cD}{k_B T} \tag{4.4}$$

where z is the valence of an ion, e is the elementary charge, c is the concentration of ion, and D is the diffusion coefficient.

Ionic trajectories during AIMD were also analyzed visually to qualitatively convey the distinct displacement behavior of Li^+ and H^+. Ion positions were sampled using a regular grid of dimension 50 x 50 x 50. Isosurfaces of ionic probability densities, normalized with respect to the mean ionic probability density (P_0), were plotted as a function of proton content in LLZO.

4.3 Results and Discussion

4.3.1 Impact of Air Exposure on Surface Chemistry

The thermodynamic driving force (i.e., the Gibbs free energy of reaction, ΔG) for the hydration and/or carbonation of LLZO was evaluated using DFT calculations for several plausible reaction pathways. The first pathway results in Li_2CO_3 formation, and proceeds via a two-step process that involves protonation of LLZO (i.e., Li^+/H^+ exchange) and the formation of LiOH as an intermediate:[46,103]

$$Li^+/H^+ \text{ ion exchange: } Li_7La_3Zr_2O_{12} + x\ H_2O \rightarrow Li_{7-x}H_xLa_3Zr_2O_{12} + x\ LiOH \quad (4.5a)$$

$$\text{Carbonation of LiOH: } LiOH + \frac{1}{2}\ CO_2 \rightarrow \frac{1}{2}Li_2CO_3 + \frac{1}{2}\ H_2O \quad (4.5b)$$

In a similar fashion, the second pathway also results in LLZO protonation and formation of Li_2CO_3, but proceeds through an Li_2O intermediate:

$$Li^+/H^+ \text{ ion exchange: } Li_7La_3Zr_2O_{12} + x\ H_2O \rightarrow Li_{7-2x}H_{2x}La_3Zr_2O_{12} + x\ Li_2O \quad (4.6a)$$

$$\text{Carbonation of } Li_2O\text{: } Li_2O + CO_2 \rightarrow Li_2CO_3 \quad (4.6b)$$

Finally, the energetics of direct hydration and carbonation of LLZO were also investigated:

$$\text{Direct hydration: } Li_7La_3Zr_2O_{12} + x\ H_2O \rightarrow Li_{7-2x}La_3Zr_2O_{12-x} + 2x\ LiOH \quad (4.7a)$$

$$\text{Direct carbonation: } Li_7La_3Zr_2O_{12} + x\ CO_2 \rightarrow Li_{7-2x}La_3Zr_2O_{12-x} + x\ Li_2CO_3 \quad (4.7b)$$

Table 4.1 summarizes the calculated ΔG for reactions 4.5-4.7 with $x = 1/8$ at T = 298.15 K. (Here $x = 1/8$ refers to the exchange of a single Li^+ for H^+ in the LLZO computational cell for reactions 4.5a-b, to the exchange of two Li^+/H^+ pairs for reactions 4.6a-b, and to the extraction of a single formula unit of Li_2O in 4.7a-b.) Several configurations were examined for the substitution and extraction of these species; the lowest energy configurations were used to evaluate Equations 4.5-4.7). Overall, pathway 4.5a-b (involving protonation of LLZO and formation of an LiOH intermediate) is predicted to be the most thermodynamically favorable reaction, given the negative values calculated for ΔG, -33 kJ.mol^{-1} for reaction 4.5a and -34 kJ.mol^{-1} for 4.5b. These data are in good qualitative agreement with experimental measurements that report Li^+/H^+ ion exchange and Li_2CO_3 formation in ambient air.[46] On the other hand, pathway 4.6a-b (involving protonation of LLZO and formation of an Li_2O intermediate) is somewhat less favored due to the positive reaction energy of 21 kJ.mol^{-1} predicated for its first step, reaction 4.6a. In addition, the total reaction energy for pathway 4.6, -127 kJ per Li_2CO_3 formula unit (f.u.), is slightly less exergonic than that of reaction 4.5: -134 kJ per Li_2CO_3 f.u. Finally, formation of LiOH and Li_2CO_3 by the direct reaction of LLZO with H_2O or CO_2 (Equation. 4.7a-b) is predicted to be thermodynamically unfavorable, as $\Delta G > 0$ for both reactions (ΔG = 83 kJ.mol^{-1} for reaction 5a and 15 kJ.mol^{-1} for 4.7b).

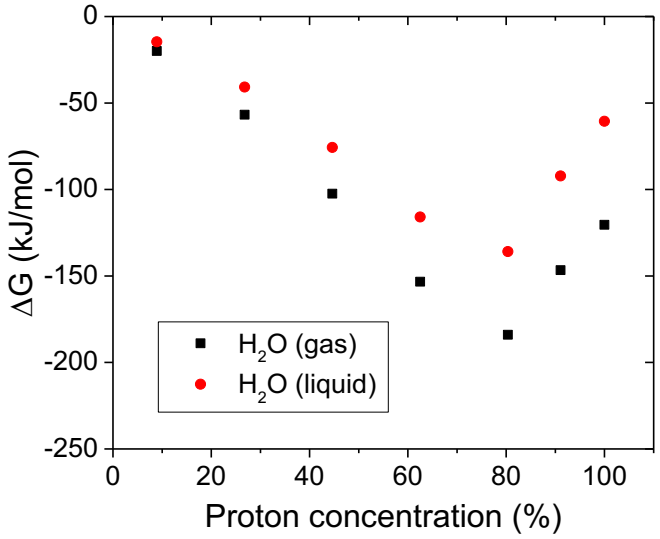

Figure 4.2 The change in Gibbs free energy at 298.15 K for reaction 4.5(a) as a function of proton concentration.

Experimental results are in good agreement with the DFT calculations. XPS data showed that LiOH and Li_2CO_3 are present on the LLZO surface after processing in the air, and TEM analysis identified the formation of Li deficient LLZO beneath the Li_2CO_3 contamination layer, which is consistent with reaction pathway (4.5) where LLZO loses Li in exchange for protons.[62] The extent of Li_2CO_3 formation on LLZO surface has been shown to depend strongly on humidity level and exposure time using Raman spectroscopy.[62]

Figure 4.2 plots ΔG at $T = 298.15$ K for reaction 4.5(a) as a function of the Li^+/H^+ exchange percentage. The data reveals that Li^+/H^+ ion exchange is thermodynamically favorable for all proton compositions up to full exchange of Li^+. The most negative ΔG value occurs at approximately 80% protonation; this value is in reasonable agreement with an earlier experimental study that observed approximately 60% of Li in LLZO powder could be exchanged with hydrogen in de-ionized water at room temperature.[97,98] Although ΔG is negative for all

proton concentrations, limited Li^+/H^+ ion mobility within partially ion-exchanged LLZO could kinetically preclude achieving very high (or full) proton exchange.[98]

Figure 4.3 plots ΔG for reaction 4.5(a) (assuming $x = 1/8$) as a function of temperature and the phase of the proton source, liquid or gaseous water. The data reveals that reaction 4.5(a) is favorable at low-to-moderate temperatures, $\Delta G < 0$ up to 466 K, regardless of whether water is a liquid or vapor. At higher temperatures, the positive values of ΔG for reaction 4.5(a) indicate the possibility for reversing the effects of water exposure by decomposing LiOH and de-protonating LLZO. In addition, we investigated the possibility for thermal decomposition of Li_2CO_3 based on a pathway that is the reverse of reactions 4.5a and 4.5b:

$$Li_{7-x}H_xLa_3Zr_2O_{12} + x/2\, Li_2CO_3 \rightarrow Li_7La_3Zr_2O_{12} + x/2\, H_2O + x/2\, CO_2 \qquad (4.8)$$

As before, we assume $x = 1/8$ (the exchange of a single Li^+ for H^+ in the LLZO unit cell). The energetics associated with reaction 4.8 at T = 298.15 K are summarized in Table 4.1. Our calculations indicate that reaction 4.8 becomes thermodynamically favorable at 597 K,

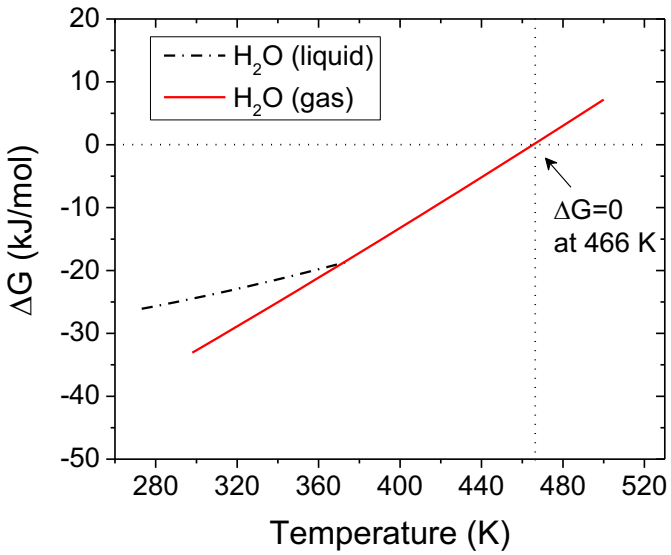

Figure 4.3 The change in Gibbs free energy for LLZO protonation, reaction 4.5(a), as a function of temperature and the phase of the proton source (liquid or gaseous H_2O). The calculation assumes $x = 1/8$.

suggesting the possibility for decomposition of Li_2CO_3 and de-protonation of LLZO at high temperatures. The predicted decomposition temperatures are consistent with earlier TG-MS measurements showing H_2O evolution from LLZO at approximately 523 K, and de-protonation of LLZO with decomposition of Li_2CO_3 between 673 and 773 K.[46,103]

4.3.2 Li Wettability at the Li-LLZO Interface

The formation of contamination layers such as LiOH and Li_2CO_3 significantly increases the Li-LLZO interfacial resistance. The increase of interfacial resistance could result from the reduction of Li wettability. To validate the correlation between surface chemistry and wettability, the wetting angle of Li on LLZO, Li_2CO_3, and LiOH was evaluated using DFT calculations.

Figure 4.4 shows the atomic structure of the low-energy interfaces for Li-LLZO and Li-Li_2CO_3. The calculated values for W_{ad} and θ are shown in Figure 4.4 below their respective interfaces. The trend predicted by our calculations - that Li strongly wets LLZO, but not Li_2CO_3 and LiOH - is consistent with the measurements of contact angle.[63] More specifically, the wetting angle predicted for the Li-Li_2CO_3 interface, $\theta = 142°$, is in excellent agreement with the measured value (142°) indicating a weak interfacial interaction between Li and Li_2CO_3 (W_{ad} = 0.10 J/m^2). In contrast, the calculated W_{ad} for the Li-LLZO interface is nearly seven times larger, W_{ad} = 0.67 J/m^2, resulting in a relatively small wetting angle, $\theta = 62°$. This value is qualitatively consistent with the measured value of 95°.[63]

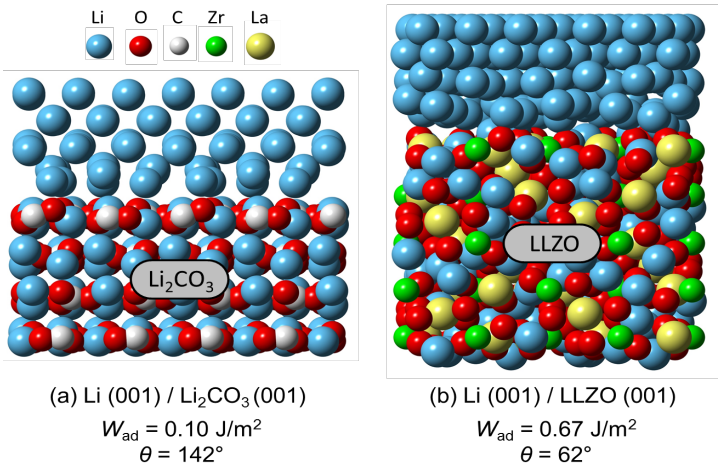

Figure 4.4 Calculated work of adhesion (W_{ad}), contact angle (θ), and atomic structure for the (a) Li-Li_2CO_3 and (b) Li-LLZO interfaces.

The smaller value predicted by our calculations is expected, given that approximately 15% of carbonate or hydroxide remains on the LLZO surface after heating to 500 °C.[63] Calculations on the Li-LiOH interface predict a relatively large contact angle of 125°, similar to the non-wetting behavior observed for the Li-Li_2CO_3 system.

The removal of LLZO surface contamination was demonstrated to enhance Li wetting of LLZO, which was also quantitatively evaluated using molten Li contact angle measurements.[63] Surface conditioning including wet polishing and heat treatment results in a dramatic increase in Li wetting and the elimination of nearly all interfacial resistance. The interfacial resistance is reduced to 2 Ω cm^2, which is lower than that of liquid electrolytes.[63]

4.3.3 Impacts of Proton Contamination on the Transport Properties

The mobility of Li^+ and H^+ ion in the H-doped LLZO was investigated using AIMD. The Arrhenius plot in Figure 4.5 demonstrates that the diffusivities of Li^+ and H^+ both decrease as the proton content of LLZO increases. In the case of limited protonation, 5H-LLZO, the reduction in the Li^+ diffusivity compared to that of pure LLZO is negligible. At this proton concentration, the diffusivity of H^+ in 5H-LLZO is also predicted to be similar to that of Li^+ in pure LLZO. These similarities are reflected in the activation energies for Li^+ and H^+ diffusion, which fall within 0.22-0.24 eV in pure and 5H-LLZO. In contrast, the diffusivities of Li^+ and H^+ are both significantly decreased in the sample with higher proton concentrations, 35H-LLZO, as shown in Figure 4.5. For this composition, Li^+ exhibits a higher diffusivity than does H^+; nevertheless, this value remains below that of Li^+ in pure LLZO. Calculated activation energies in 35H-LLZO are significantly larger (in some cases double) than in pure LLZO or 5H-LLZO: 0.32 eV for Li^+ and 0.41 eV for H^+.

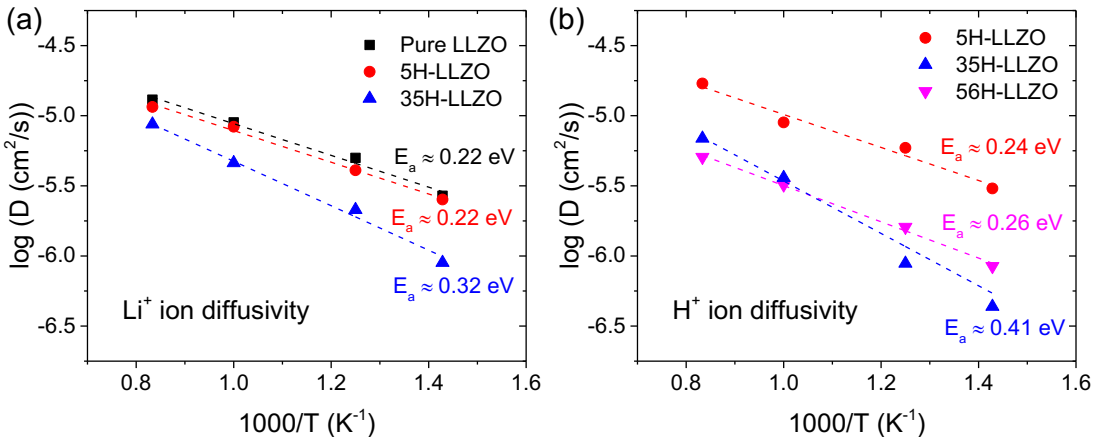

Figure 4.5 Arrhenius plots for diffusivity derived from MSD plots: (a) Li^+ ion diffusivity for pure, 5H-LLZO, and 35H-LLZO and (b) H^+ ion diffusivity for 5H-LLZO, 35H-LLZO, and 56H-LLZO.

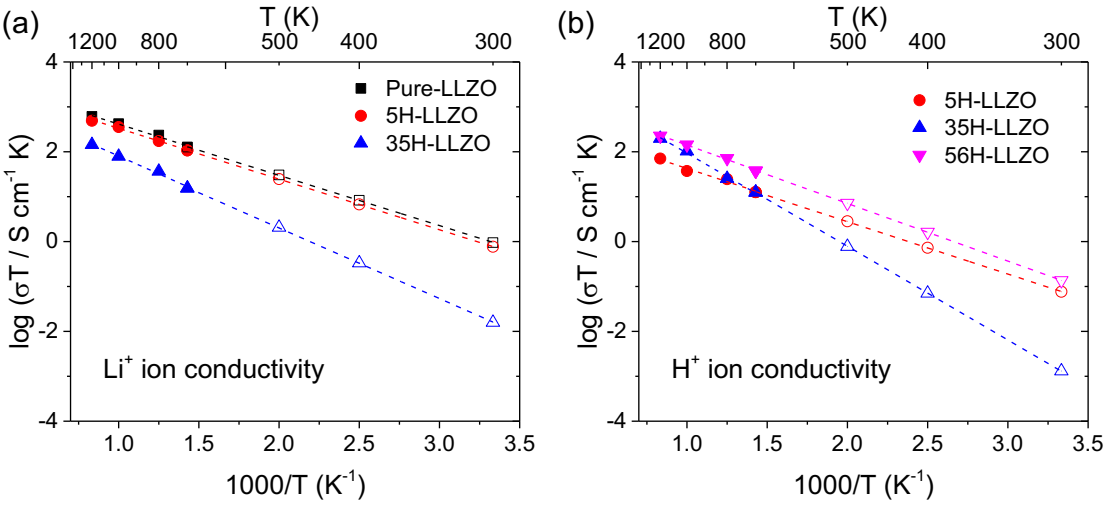

Figure 4.6 Arrhenius plots for conductivity derived from MSD plots using the Nernst-Einstein equation: (a) Li^+ ion conductivity for pure, 5H-LLZO, and 35H-LLZO and (b) H^+ ion conductivity for 5H-LLZO, 35H-LLZO, and 56H-LLZO. Ionic conductivities for lower temperature (open symbols) were obtained using the extrapolation of Arrhenius fits for high temperature data (700-1200 K).

The ionic conductivities are extrapolated to 300 K as shown in Figure 4.6 and Table 4.2. The Li ionic conductivity in pure LLZO is comparable to that in 5H-LLZO ($3*10^{-3}$ S/cm), while the conductivity in 35H-LLZO is two orders smaller. The proton conductivity is smaller than Li^+ ion conductivity about one order in 5H-LLZO and 56H-LLZO, while it is three orders smaller in 35H-LLZO. These results indicate that the Li^+ and H^+ ion conductivities are significantly decreased at the major level of proton contamination above 60 %.

Ionic trajectories were obtained to examine the role of proton in decreasing the ion diffusivity in protonated LLZO. Figure 4.7 shows isosurfaces of the Li^+ and H^+ ion probability densities ($2P_0$) for Pure and H-LLZO cells, obtained from 40 ps AIMD simulations at 1000 and 700 K. As predicted from the Arrhenius plot, the isosurfaces for Li are well-connected in 5H-LLZO, indicative of a high Li-ion diffusivity. In contrast, these features are more fragmented in 35H-LLZO, consistent with lower mobility. In the case of H^+, for low proton concentrations the trajectory isosurfaces resemble that of Li^+ (with the exception that much less H^+ is present compared to Li^+). However, at the higher protonation level H^+ exhibits localized displacements which appear to be more compact that those of Li^+. This behavior suggests that H^+ acts to partially block Li ion diffusion at high proton concentrations.

Table 4.2 Activation energy and extrapolated ionic conductivity at 300 K

	E_a for σ_{Li} (eV)	E_a for σ_H (eV)	σ_{Li} at 300 K (S cm^{-1})	σ_H at 300 K (S cm^{-1})
Pure LLZO	0.22	N/A	3.2×10^{-3}	N/A
5H-LLZO	0.22	0.24	2.6×10^{-3}	2.5×10^{-4}
35H-LLZO	0.32	0.41	5.3×10^{-5}	4.4×10^{-6}
56H-LLZO	N/A	0.26	N/A	4.5×10^{-4}

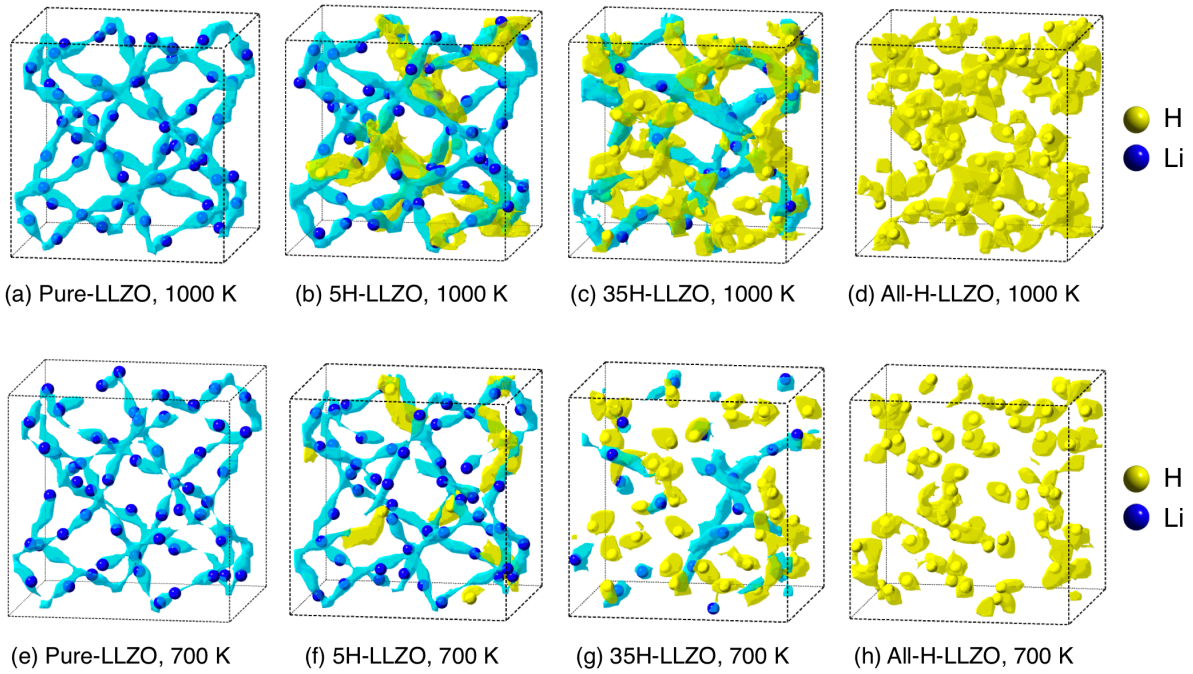

Figure 4.7 Isosurfaces of Li^+ and H^+ probability densities from 40 ps AIMD simulations at T = 700 and 1000 K plotted for a density of $2P_0$. (P_0 represents the respective mean probability density.) (a, e) Pure LLZO; (b, f) 5H-LLZO; (c, g) 35H-LLZO; and (d, h) 56H-LLZO. For clarity, only Li and H atoms are shown. Blue isosurfaces correspond to the probability density for Li-ions, yellow isosurfaces correspond to protons.

4.4 Conclusions

The impact of air exposure on the LLZO surface are examined using DFT calculations. The calculations indicate that Li^+/H^+ exchange with formation of LiOH is a thermodynamically favorable route for the subsequent formation of a Li_2CO_3 layer on the surface of LLZO, while direct hydration and carbonation of LLZO is found to be thermodynamically unfavorable.

The formation of contamination layers at the LLZO surface has a significant effect on the Li-LLZO interfacial resistance. The Li wettability is examined as a means to explain the origin of high interfacial resistance in the presence of a contamination layer. DFT Calculations indicate that Li strongly wets LLZO, but not Li_2CO_3 and LiOH, which is consistent with the measurements of contact angle. The removal of surface contamination dramatically reduces the interfacial resistance to 2 Ω cm^2, comparable to solid-liquid interfaces in Li-ion cells.

The transport properties in protonated LLZO are studied using AIMD. The Li ionic conductivity in protonated LLZO is comparable to that in pure LLZO at the minor level of protonation (~10 %), while Li ion conductivities are significantly decreased at the major level of proton contamination (~ 60%). At the higher protonation level, H^+ exhibits localized displacements suggesting H^+ acts to partially block Li ion diffusion.

Chapter 5 Elastic Properties

5.1 Introduction

A viable solid electrolyte (SE) should exhibit appropriate mechanical properties. In particular, the elastic moduli of a SE are of key importance. First, it is believed that a SE's shear modulus impacts the tendency for dendrites to form on the anode surface during plating.[15] Linear elasticity analyses performed by Monroe and Newman suggest that the shear modulus should be at least twice that of Li metal in order to prevent dendrite nucleation.[15] Secondly, the Young's modulus impacts the fracture strength of a SE. Based on Griffith theory, the fracture strength can be estimated using the Young's modulus and the surface energy.[104]

Unfortunately, very few investigations of the mechanical properties of LLZO have been reported. Ni *et al*.[105] measured the room temperature elastic moduli (Young's modulus, E, shear modulus, G, bulk modulus, B, and Poisson's ratio, v) of Al-doped cubic LLZO ($Li_{6.24}Al_{0.24}La_3Zr_2O_{11.98}$, volume fraction porosity, $P = 0.03$) using resonant ultrasound spectroscopy (RUS).[105] The values reported were E = 149.8 GPa, G = 59.6 GPa, and B = 102.8 GPa. On the other hand, the elastic properties of Ta-doped LLZO are not available in the literature. Similarly, an evaluation of the elastic constants of LLZO also appears to be absent.

The present study aims to close these knowledge gaps by determining the elastic constants and moduli for Al- and Ta-doped LLZO using first-principles computation. Multiple experimental measurements were compared to values predicted by Density Functional Theory (DFT) calculations. In addition, the elastic properties of metallic Li were re-visited computationally. This data was used with the elasticity analyses of Monroe and Newman,[15] and in combination with the measured LLZO elastic properties, to assess the effectiveness of LLZO in suppressing dendrite formation at the Li-LLZO interface.

We find that the predicted and measured elastic properties for LLZO are in excellent agreement. For example, the calculated elastic constants are within 5% of the nanoindentation measurements, with Young's modulus values (E) ranging from 147 to 154 GPa across the Al and Ta-doped LLZO compositions. Furthermore, the predicted data are consistent with impulse excitation measurements, which capture the polycrystalline microstructure of LLZO specimens; in this case E values between 140 and 146 GPa were obtained for specimens of relative density greater than 98%. Finally, the measured and calculated shear modulus (G) for Al/Ta-doped LLZO is approximately 60 GPa. This value is more than an order of magnitude larger than that of BCC Li. Hence, based on the model of Monroe,[15] both LLZO compositions may be stiff enough to suppress lithium dendrite formation. These data provide important insights into the mechanical properties of the Li-LLZO interface.

5.2 Methodology

DFT calculations were performed using GGA-PBE as the exchange correlation energy. An energy cutoff of 600 eV was used for the plane wave basis. Extensive K-point convergence testing was performed so as to obtain accurate elastic properties. Calculations employing up to a

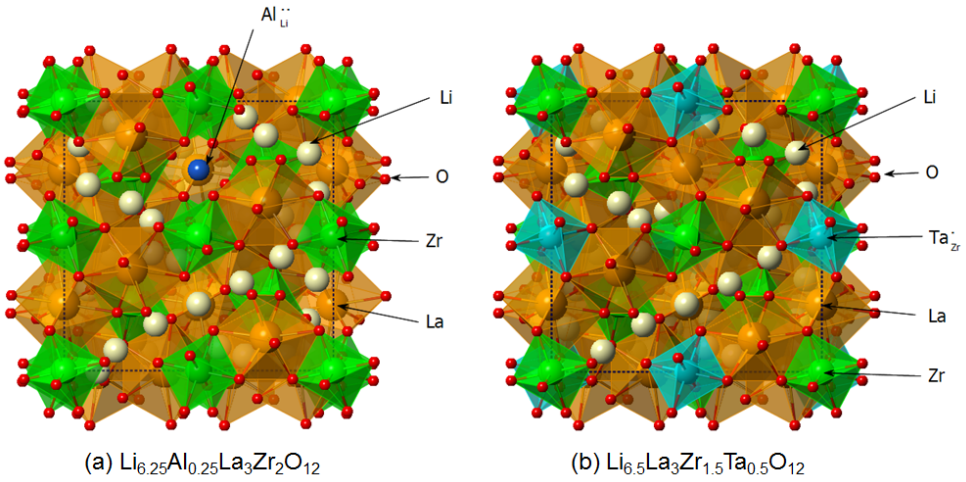

Figure 5.1 Atomic structure of the computational cells for (a) $Li_{6.25}Al_{0.25}La_3Zr_2O_{12}$ and (b) $Li_{6.5}La_3Zr_{1.5}Ta_{0.5}O_{12}$. Al''_{Li} and $Ta^{\cdot}_{Zr}$ denote, respectively, Al substitution on Li sites and Ta substitution on Zr sites, using Kröger–Vink notation.

46×46×46 *k*-point mesh (2300 irreducible *k*-points) were used for metallic Li, and a 4×4×4 mesh (32 irreducible k-points) was used for LLZO. The convergence criterion for the electronic self-consistency loop was set to 10^{-5} eV (5.32×10^{-5} meV/atom for LLZO) and atomic positions were relaxed (for a specified cell shape and volume) until the forces were less than 0.01 eV/Å.

Simulation cells were based on the experimental Al-doped[106] and Ta-doped[32] LLZO cubic crystal structures, as shown in Figure 5.1. For pristine LLZO cells, Li was distributed on the partially-occupied 24d and 96h sites with occupancies of 0.543 and 0.448 using a procedure that excluded occupation of electrostatically-unfavorable first nearest-neighbor sites.[36]

In the Al-doped structure ($Li_{6.25}Al_{0.25}La_3Zr_2O_{12}$), two randomly-selected 24d Li sites were replaced by Al. (Li 24d sites have been previously identified as the most energetically favorable sites for Al doping.[107]) To maintain charge neutrality, a total of four Li atoms located near the Al-sites were also removed from the cell. Likewise, for the Ta-doped structure ($Li_{6.5}La_3Zr_{1.5}Ta_{0.5}O_{12}$), four Zr atoms were replaced by an equivalent number of Ta dopants,[32] and a total of four Li vacancies were created to maintain charge neutrality. The resulting

occupancies of the 24d sites are 0.458 (equivalent to 11 Li^+ ions in unit cell) for both the Al and Ta-doped cells, and 0.406 and 0.427 (equivalent to 39 and 41 Li^+ ions in unit cell) for the 96h sites, respectively. To facilitate comparisons with the mechanical properties of a Li anode, the elastic properties of metallic BCC lithium were also investigated.

The elastic properties of a solid phase having a cubic crystal structure can be described using three elastic constants: C_{11}, C_{12}, and C_{44}.[108] The elastic constants were evaluated using Hook's law by calculating the total energy as a function of strain. In addition to being ingredients in the calculation of the elastic and shear moduli (described below), the elastic constants constitute fundamental mechanical properties of a crystalline phase. For example, these data may be useful in follow-on studies involving mesoscale modeling of LLZO-based separators. Three methods were explored for determining the C_{11} and C_{12} elastic constants for LLZO:

*Method A: Direct calculation of C_{11} and the bulk modulus, B***.** In this case the uniaxial strain, C_{11}, was determined by incrementally expanding or contracting the crystal along a [100] direction (up to ±3% of the minimum-energy lattice constant), and fitting the resulting energy-strain data to a quadratic polynomial. Next, the bulk modulus, *B*, was obtained by fitting total energy *vs*. volume data to the Murnaghan equation of state.[91] C_{12} was then derived using *B* and C_{11}, using the relation (5.1):[108]

$$B = \frac{1}{3}(C_{11} + 2C_{12}) \tag{5.1}$$

Method B: Direct calculation of C_{11} and the difference $C_{11} - C_{12}$. The difference $C_{11} - C_{12}$, defined as Δ_{11-12}, can be independently derived by shearing the crystal with an orthorhombic strain,[108]

$$\varepsilon = \begin{bmatrix} \delta & 0 & 0 \\ 0 & -\delta & 0 \\ 0 & 0 & \delta^2/(1-\delta^2) \end{bmatrix} \tag{5.2}$$

Here, $(\Delta_{11-12})/2$ represents the resistance to a shear stress applied across the (110) plane in the $[1\bar{1}0]$ direction.[109] δ refers to a small strain, which in our calculations is on the order of 0.02. C_{12} can then be obtained using a combination of C_{11} and Δ_{11-12}.

Method C: Direct calculation of B and Δ_{11-12}. In this case C_{11} and C_{12} are evaluated using Eq. 5.1 and the definition of Δ_{11-12}.

For all methods C_{44} was obtained by incrementally shearing the crystal with a monoclinic strain,[108]

$$\varepsilon = \begin{bmatrix} 0 & \delta/2 & 0 \\ \delta/2 & 0 & 0 \\ 0 & 0 & \delta^2/(4-\delta^2) \end{bmatrix} \tag{5.3}$$

and fitting to a quadratic polynomial. In this case δ was varied between -0.03 and +0.03.

Subsequently, the directional properties of the Young's modulus, $E_{[100]}, E_{[110]}$, and $E_{[111]}$, and the shear modulus, $G_{[100]}, G_{[110]}$, and $G_{[111]}$, were derived from the elastic constants C_{11}, C_{12}, and C_{44} according to:[110]

$$E_{[100]} = \frac{(C_{11}-C_{12})(C_{11}+2C_{12})}{(C_{11}+C_{12})} \tag{5.4a}$$

$$E_{[100]} = \frac{(C_{11}-C_{12})(C_{11}+2C_{12})}{(C_{11}+C_{12})} \tag{5.4b}$$

$$E_{[110]} = \frac{4(C_{11}-C_{12})(C_{11}+2C_{12})C_{44}}{2C_{11}C_{44}+(C_{11}-C_{12})(C_{11}+2C_{12})} \tag{5.4c}$$

$$G_{[100]} = C_{44} \tag{5.5a}$$

$$G_{[110]} = \frac{2(C_{11}-C_{12})C_{44}}{C_{11}-C_{12}+2C_{44}} \tag{5.5b}$$

$$G_{[111]} = \frac{3(C_{11} - C_{12})C_{44}}{C_{11} - C_{12} + 4C_{44}} \tag{5.5c}$$

These values allow for estimating the anisotropy of the elastic moduli. The polycrystalline isotropic shear modulus, G, was obtained using the calculated elastic constants in combination with the Voigt–Reuss–Hill averaging scheme:[110]

$$G = \frac{1}{2}\left[\frac{C_{11} - C_{12} + 3C_{44}}{5} + \frac{5C_{44}(C_{11} - C_{12})}{4C_{44} + 3(C_{11} - C_{12})}\right] \tag{5.6}$$

Finally, Young's modulus, E, and Poisson's ratio, ν, assuming an isotropic polycrystalline material, were evaluated using:

$$E = \frac{9GB}{3B + G} \tag{5.7}$$

$$\nu = \frac{3B - 2G}{2(3B + G)} \tag{5.8}$$

5.3 Results and Discussion

5.3.1 Elastic Properties of Al and Ta-Doped LLZO

Figure 5.2(a) shows the total energy of Al-doped LLZO as a function of cell volume, and the associated fit of this data to the Murnaghan equation of state. Similarly, Figure 5.2(b), (c), and (d) show the total energy as a function of uniaxial, monoclinic, and orthorhombic strain, respectively; solid lines represent fits to a quadratic polynomial. A 2×2×2 *k*-point mesh (4 irreducible *k*-points) was determined to be sufficient to achieve converged values for the bulk modulus and elastic constants; this *k*-point mesh was also adopted for calculations of the elastic constants, C_{11}, C_{12}, and C_{44}.

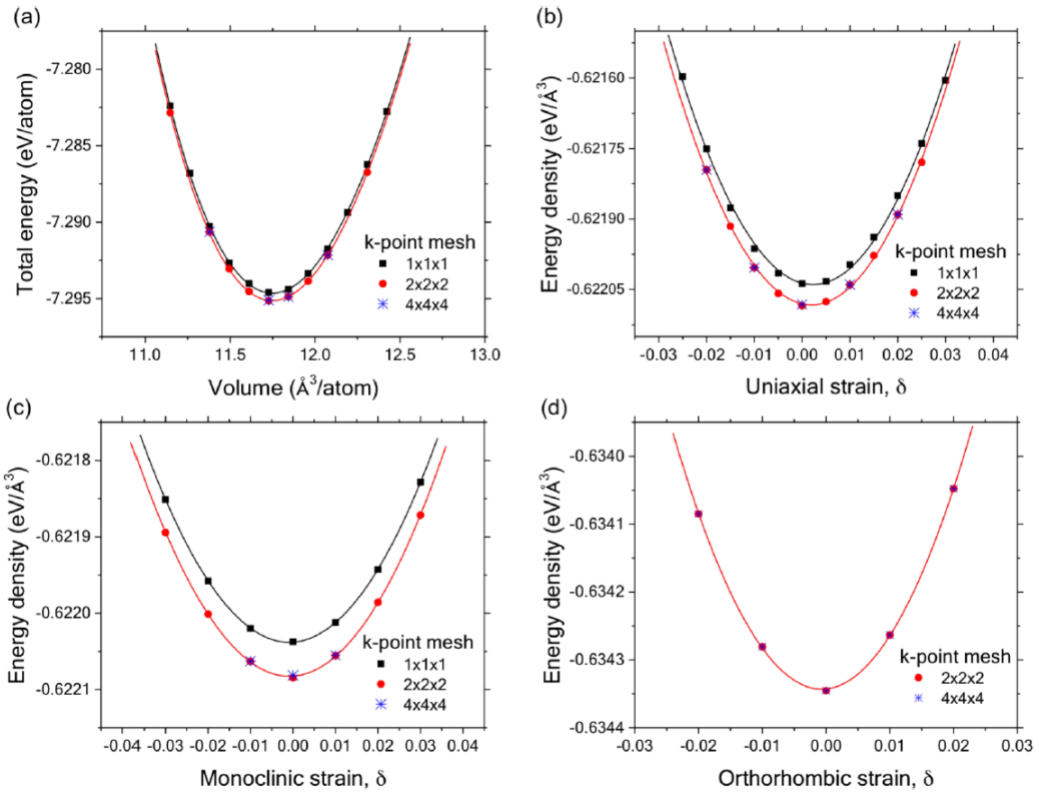

Figure 5.2 A Calculated total energy (or energy density) of Al-doped LLZO as a function of the (a) cell volume, (b) uniaxial strain, (c) monoclinic strain, and (d) orthorhombic strain.

As mentioned earlier, three methods were explored for determining the elastic constants. All three approaches employ a direct calculation for C_{44}, but then use two different independent quantities to derive the remaining elastic properties. The elastic constants for LLZO derived from these three methods have very similar values, as shown in Table 5.1. The elastic moduli and Poisson's ratio were derived using Eq. (5.1), (5.4)-(5.7).

The elastic constants and moduli of Al-doped LLZO are summarized in Table 5.2. The calculated values were determined using method A (via independent calculations of B, C_{11}, and C_{44}). The calculated B, E, and G at zero Kelvin are 112.4 GPa, 162.6 GPa and 64.6 GPa, respectively. The elastic moduli of oxides typically decrease with increasing temperature.

Table 5.1 Calculated elastic properties of Al-doped LLZO ($Li_{6.25}Al_{0.25}La_3Zr_2O_{12}$) as a function of calculation method[a]

Method	B	C_{11}	C_{12}	C_{44}	$E_{[100]}$	$E_{[110]}$	$E_{[111]}$	E	$G_{[100]}$	$G_{[110]}$	$G_{[111]}$	G	ν
A	112.4*	187.0*	75.1	71.0*	144.0	166.8	176.0	162.6	71.0	62.6	60.2	64.6	0.26
B	113.2	187.0*	76.2*	71.0*	142.8	166.5	176.2	162.2	71.0	62.2	59.8	64.3	0.26
C	112.4*	186.2	75.5*	71.0*	142.7	166.3	176.0	162.0	71.0	62.2	59.8	64.3	0.26

[a]Values marked with an asterisk denote data evaluated directly from DFT calculations; the remaining values were derived using Eq. (5.1), (5.4)-(5.7). The elastic constants and moduli are expressed in GPa.

Table 5.2 Elastic properties of Al-doped and Ta-doped LLZO[a]

	C_{11}	C_{12}	C_{44}	B	E	G	ν
Al-doped LLZO							
DFT (0 K)	187.0	75.1	71.0	112.4	162.6	64.6	0.26
DFT extrapolated (298 K)					154.5	61.4	
Impulse excitation (298 K)				100.2 ± 0.6	146.1 ± 0.8	58.1 ± 0.3	
Nanoindentation (298 K)					150.3 ± 2.2	59.8 ± 0.9	
RUS (298 K) Ref. A				102.8 ± 0.3	149.8 ± 0.4	59.6 ± 0.1	0.257±0.002
Ta-doped LLZO							
DFT (0 K)	169.8	63.9	69.8	99.2	154.9	62.5	0.24
DFT extrapolated (298 K)					147.2	59.4	
Impulse excitation (298 K)				96.0 ± 1.4	139.9 ± 2.1	55.7 ± 0.8	
Nanoindentation (298 K)					153.8 ± 2.7	61.2 ± 1.1	

[a]The elastic constants and moduli are expressed in GPa.

Representative decreases for common oxides between 0 and 298 K are: ~4 % for MgO, ~1 % for Al_2O_3,[111] and ~9 % for Li_2O.[112] We therefore assume that the calculated moduli of LLZO at 0 K should be reduced by ~5% to estimate behavior at room temperature. Adopting this scaling factor, we arrive at room temperature values of 154.5 GPa and 61.4 GPa for E and G, respectively.

Methods A-C were also used to calculate the elastic constants of Ta-doped LLZO. The elastic constants derived from the three methods have very similar values. In Table 1, the

calculated B, E, and G evaluated using method A are 99.2, 154.9 and 62.5 GPa, respectively. Assuming a 5% softening of moduli between 0 and 298 K, the predicted values of E and G at room temperature are 147.2 and 59.4 GPa, respectively.

From nanoindentation, the Young's modulus (E) of the Al-doped LLZO is 150.3 ± 2.2 GPa; for Ta-doped LLZO a value of 153.8 ± 2.7 GPa was measured. Because the size of each nanoindentation is approximately 500 nm - which is 2 to 100 times smaller than the diameter of each grain - the elastic moduli values are approximately equivalent to an average over several single grain/quasi-single crystal measurements performed on random orientations. Thus, when comparing the calculated (154.5 and 147.2 GPa, respectively) and measured average quasi-single crystal values, excellent agreement is achieved (Table 5.2). At 298 K the Al-doped and Ta-doped calculated and measured quasi-single crystal elastic moduli are within 3 and 5 %, respectively. Indeed, theory predicts the Ta-doped LLZO should have a lower elastic modulus compared to the Al-doped LLZO. However, the relatively small difference in values could be due to experimental error.

By impulse-excitation, the E of the Al-doped LLZO is 146.1 ± 0.8 GPa and Ta-doped LLZO is 139.9 ± 2.7 GPa (Table 5.2). Because the impulse excitation technique interrogates the specimen volume beneath the transducer (8 mm diameter) and the grains are < 50 μm, the elastic moduli represent isotropic bulk polycrystalline values that include < 2% porosity. The error in the elastic moduli is primarily a function of the variation in the specimen thickness.

Experimentally, G measured by nanoindentation is 59.8 ± 0.9 GPa for Al doped LLZO and 61.2 ± 1.1 GPa for the Ta- doped sample (Table 5.2). By impulse excitation G is 58.1 ± 0.3 GPa for Al doped LLZO and 55.7 ± 0.8 GPa for Ta-doped LLZO (Table 5.2). Importantly, from Table 5.2 it can be observed that the calculated and measured (by both impulse excitation and

nanoindentation) E and G moduli are within 5%. In addition, from Table 5.2 it can be observed that experimental and calculated E and G values for Al-doped LLZO are consistent with literature values reported from RUS measurements of similar Al-doped LLZO.[105]

The average of the calculated, nanoindentation, and impulse excitation measurements for E (Table 5.2 at 298 K) for Al and Ta-doped LLZO is 150 GPa and 147 GPa, respectively. Using $\nu = 0.26$ (Table 5.2) and equation 5.10, these elastic moduli averages give average shear moduli of 60 GPa and 58 GPa for the Al and Ta-doped LLZO, respectively. The significance of these values will be discussed below after we revisit the shear moduli data for Li.

5.3.2 Ductility and Elastic Anisotropy

In addition to being stiff to prevent dendrite penetration, some degree of ductility would also be desirable in a SE so as to maintain good interfacial contact with an electrode during cycling. As a rough estimate of the ductility of LLZO, we have calculated the ratio of the bulk modulus to the shear modulus, B/G, which indicates the ductility/brittleness nature of a solid. According to Pugh's criterion,[113] the critical B/G value for a transition from brittle to ductile behavior is 1.75. The calculated B/G values for Al and Ta-doped LLZO are 1.74 and 1.59, respectively. A strict interpretation of Pugh's criterion indicates that both compounds should therefore be considered brittle materials, with the Al-doped variant being the more ductile of the two compositions. The brittle behavior of both compounds is consistent with the general properties of oxides such as γ-SiO_2, for which $B/G = 1.4$.[114]

The predicted brittle nature of the two LLZO compositions is in agreement with fracture toughness results of Wolfenstine *et al.*[115] on Al doped LLZO ($Li_{6.24}Al_{0.24}La_3Zr_2O_{11.98}$) where a fracture toughness of ~1.25 MPa-$m^{1/2}$ was measured. This value can be compared to fracture

toughness values of ~1 MPa-$m^{1/2}$ for an ideal brittle material, such as silicate glass, and 25-35 MPa-$m^{1/2}$ for ductile metals like aluminum.

Both Al and Ta-doped LLZO exhibit elastic anisotropy: the Young's modulus projected onto the [111] direction is the largest of the 3 directions, with the [100] projection being the smallest. The ratio $E_{[111]}/\ E_{[100]}$ is 1.22 and 1.26 for Al and Ta-doped LLZO, respectively. The Zener anisotropy ratio, A, which is given by

$A = \frac{2C_{44}}{C_{11}-C_{12}}$ describes the elastic anisotropy of a cubic crystal, with a value of A = 1 indicating an isotropic material. For Al and Ta-doped LLZO, anisotropy ratios of 1.27 and 1.32 were calculated, respectively. To place these values in context, we note that several oxides have high anisotropy ratios: for example, 2.38 for $BaTiO_3$, 2.15 for $MgAl_2O_4$ and 2.14 for UO_2. On the other hand, common isotropic oxides include: NiO (1.45), MnO (1.54), and MgO (1.55).[116] Since $A \cong 1$ for Al and Ta-doped LLZO, we conclude that their elastic properties are relatively isotropic.

5.3.3 Elastic Properties of Metallic Lithium

The calculated elastic constants and moduli for BCC Li are summarized in Tables 5.3 and 5.4. Values reported there are for Method A. The values for B**,** C_{11}, and C_{44} at zero Kelvin were obtained using direct DFT calculations, while the other elastic properties were derived from those values using Eq. (5.4)-(5.7). In Table 5.3, the calculated values for B, C_{11}, and C_{44} are 13.7 GPa, 15.3 GPa and 11.3 GPa, respectively. These values are in very good agreement (differing by only 3%) with the experimental data, which fall within the ranges 13.1 - 13.8 GPa (B), 14.6 - 15.4 GPa (C_{11}) and 11.3 - 11.4 GPa (C_{44}) GPa at 0 K.[117–119] At room temperature the experimental values are approximately 15% lower.[118–120] Thus, the predicted E and G values are

Table 5.3 Elastic Properties of BCC Li[a]

	B	C_{11}	C_{12}	C_{44}	E	G	ν
			0 K				
DFT (present study)	13.7	15.3	12.8	11.3	13.0	5.0	0.34
Experiment Ref. 117	13.8	15.4	13.0	11.3	12.9*	4.9*	
Experiment Ref. 118	13.2	14.7	12.5	11.3	12.6*	4.8*	
Experiment Ref. 119	13.1	14.6	12.4	11.4	12.6*	4.8*	
			298 K				
DFT (present study)					11.1	4.25	
Experiment Ref. 118	12.0	13.4	11.3	8.9	10.6*	4.0*	
Experiment Ref. 119	11.9	13.3	11.2	8.8	10.5*	4.0*	
Experiment Ref. 120	12.0	13.4	11.3	8.8	10.5*	4.0*	
Experiment Ref. 121					8.0		
Experiment Ref. 122					4.9		

[a]The elastic constants and moduli are expressed in GPa. Values marked with an asterisk are derived using Eq. (5.6) and (5.7). DFT values were extrapolated to 298 K by reducing the zero Kelvin values by 15%.

Table 5.4 Calculated elastic properties of BCC Li evaluated using method A[a]

B	C_{11}	C_{12}	C_{44}	$E_{[100]}$	$E_{[110]}$	$E_{[111]}$	E	$G_{[100]}$	$G_{[110]}$	$G_{[111]}$	G	ν
13.7*	15.3*	12.8	11.3*	3.6	10.3	26.6	13.0	11.3	2.2	1.8	5.0	0.34

[a]Values marked with an asterisk denote data evaluated directly from DFT calculations; the remaining values were derived using Eq. (5.1), (5.4)-(5.7). The elastic constants and moduli are expressed in GPa.

approximately 11.1 and 4.25 GPa, respectively, when extrapolated to room temperature using a similar scaling factor (reduction of 15%).

The predicted value for *E* of 11.1 GPa at room temperature can be compared to room temperature experimental values for Li of 8 GPa[121] and 4.9 GPa[122], as determined by resonance spectroscopy and from static bending tests under oil, respectively. The predicted value is reasonable agreement with the resonance value and about twice higher than the static value. It is

known that dynamic values are in general more accurate than static values as a result of experimental difficulties (e.g. friction at the load points).

5.3.4 Discussion and Implications

Microstructural features such as (i) porosity, (ii) second phases, (iii) texture, and (iv) grain size can influence the experimental modulus. Although calculated and measured moduli are in very good agreement, these four features could, in principle, account for differences between theory and experiment. As described above, the LLZO samples examined here are close to theoretical density, contain no second phases and have no texture.[105] This rules out contributions from factors (i)−(iii). Furthermore, it has been previously established that the modulus is independent of grain size and grain boundary characteristics when the grain size is in the micrometer range.[123] Since the grain size of both LLZO samples is within this range, 5−50 μm for the Al-doped specimen and 1−10 μm for the Ta-doped specimen, this rules out factor (iv). Therefore, the experimental modulus is not strongly influenced by micro- structural features and can be directly compared to the DFT values. Furthermore, our data suggests that variations in the vacancy content of the Li sublattice (brought about by doping with either Al or Ta) do not have a large effect on elastic properties for the doping levels considered here. It appears that contributions from the other sublattices (Zr, O, La) have a larger influence on these properties.

According to the model of Monroe et al., a solid electrolyte having a shear modulus that is a factor of 2 times greater than the shear modulus of metallic Li should suppress dendrite initiation.[15] Given the calculated shear modulus for Li determined in this work (4.25 GPa), a solid electrolyte having a room temperature shear modulus greater than approximately 8.5 GPa is required to suppress dendrite formation. The averaged shear moduli of Al- and Ta-doped LLZO,

58−60 GPa, are more than 10 times greater than the shear modulus of Li and, therefore, could suppress Li dendrite formation. Nevertheless, it is important to recognize that scenarios exist in which dendrites could still form even in the presence of a solid electrolyte that satisfies Monroe's criterion. This could occur, for example, in cases where significant porosity exists at the electrolyte/anode interface. In other words, satisfying Monroe's criterion should be viewed as a necessary, but not sufficient condition for a viable solid electrolyte. As the integrity of the electrode/electrolyte interface is critical, the elastic properties of the electrode materials are also an important factor in the performance of solid-state batteries.

It is instructive to compare the elastic properties of LLZO to those for other solid oxide Li-ion conductors. The Young's modulus for LATP ($Li_{1+x}Al_xTi_{2-x}(PO_4)_3$ with $x\approx0.3$) determined from stress-strain curves at low strains is approximately 115 GPa.[124] For $Li_{3x}La_{0.67-x}TiO_3$ with $x\approx0.11$ (LLTO) E ~193 GPa was determined from nanoindentation and resonant ultrasound spectroscopy.[125] Finally, LiPON thin films have E = 77 GPa as determined using nanoindentation.[126] Thus, the LLZO E value of ~150 GPa reported here is higher than that for LATP and LiPON, but smaller than that for LLTO.

5.4 Conclusions

High ionic conductivity is a necessary, *but not sufficient* condition for a viable solid electrolyte: to enable use of a metallic lithium anode, such an electrolyte must also be stiff enough to suppress Li dendrite formation during plating. Consequently, the elastic properties of the solid electrolyte are a highly important – yet occasionally overlooked – feature in the design of all-solid-state batteries. The linear elasticity model of Monroe and Newman suggests that a solid electrolyte having a shear modulus greater than approximately 8.5 GPa can suppress dendrite formation on a Li anode. The present calculations yield averaged shear moduli for Al and Ta-doped LLZO of 58-60 GPa, far exceeding the targeted value. The high shear moduli reported here suggest that an LLZO-based solid electrolyte could enable long-lived Li-metal batteries.

Chapter 6 Grain Boundary Contributions to Li-Ion Transport

6.1 Introduction

Typical protocols for the synthesis of LLZO generate samples that are polycrystalline.[55–59] It is well-known that interfaces between individual crystallites, known as grain boundaries (GBs), can strongly influence the properties of essentially all types materials. In the case of LLZO, GB-related phenomena have been implicated in two areas: the transport of Li- ions[55,56] and short-circuiting[52,54,127,128].

Regarding transport, GBs can either suppress or enhance the rates of ionic diffusion in polycrystalline oxides. For example, ionic diffusion is enhanced (relative to bulk diffusion) due to the presence of GBs in Al_2O_3,[129] HfO_2,[130] and UO_2.[131] Conversely, GBs hinder ion transport in $SrTiO_3$,[132] YSZ,[133] and doped CeO_2.[134]

In LLZO, GB resistance has been reported to decrease Li-ion conductivity.[55–59] These effects can be partially minimized by altering the synthesis conditions to increase the density of LLZO (by reducing porosity), increasing the grain size (i.e., minimize the volume fraction of GBs), and/or improving contact at the GBs.[56] For example, increasing the hot pressing temperature to 1100°C resulted in higher density LLZO samples (99% of theoretical density) and

larger grain sizes; consequently, the GB contribution to the total resistance decreased to 8%, compared to a larger 26% contribution for hot pressing at a lower temperature of 1000°C.[56]

Regarding short circuiting, recent studies have shown that Li metal 'dendrites' can penetrate stiff LLZO membranes along its GB network, resulting in cell failure.[52,54,127,128,135] This surprising result indicates that microstructural features, and not elastic properties alone,[15,60] should be considered in the design of practical solid electrolytes.

The preceding examples suggest that understanding the connection between structure and transport (of Li metal and Li-ions) at GBs will accelerate the development of solid electrolytes. Despite the importance of GBs, the atomic-scale processes occurring at GB in LLZO remain poorly understood. The study reported in this chapter aims to close this knowledge gap by combining classical Monte Carlo and molecular dynamics (MD) simulations to predict the energetics, composition, and transport properties of three low-energy (Σ3 & Σ5) symmetric tilt GBs in LLZO.

MD calculations reveal that the equilibrium composition near GBs in LLZO (i.e., in the GB plane) is enriched with Li, and to a lesser extent with oxygen. MD simulations on these off-stoichiometric structures indicate that the mobility of Li-ions is generally reduced in all three GB (compared to bulk LLZO), although the magnitude of this reduction can be small in compact boundaries, and at the high temperatures encountered during synthesis (~1000 K). The suppression of Li-ion mobility is largest in the Σ5 boundaries, where our calculations predict activation energies for diffusion are up to 35% greater than in the bulk. In contrast, diffusion in the compact Σ3 boundary is characterized by an activation energy that is identical to bulk LLZO. Consequently, the rate of Li migration in this GB is only slightly suppressed, with the suppression attributed to the diffusion prefactor. Similar to the bulk, diffusion in both of the Σ5

GBs is largely isotropic. In contrast, diffusion in the Σ3 boundary is anisotropic at lower temperatures. In this case, diffusion in the boundary plane is faster than bulk transport, while trans-boundary diffusion (i.e., across the boundary plane) is approximately 200 times slower than the bulk.

These data suggest that low-energy GBs provide a 'mixed' contribution to Li-ion transport in LLZO: more compact boundaries allow for faster diffusion (i.e., comparable to bulk), while diffusion is significantly retarded in boundaries with larger excess volumes. The opposing impact of these boundaries indicates that the net effect of GBs on Li-ion transport could be modest in samples that are processed under conditions amenable to achieving a high fraction of low-energy, compact boundaries. This observation is consistent with experimental measurements showing that the GB resistance in LLZO is relatively small in samples that are processed at high temperatures.[56]

Although the low energies of the GBs studied here suggest that they will be present in annealed samples, lower-temperature synthesis routes could generate higher-energy GBs with less-compact structures. Such GBs are expected to have a larger impact on Li-ion conductivity, and therefore should be considered in future studies.

6.2 Methodology

Symmetric tilt GBs with coincident site lattice (CSL) designations of Σ3 and Σ5 were examined.[136,137] Three boundary geometries were considered: Σ5(310)/[001], Σ5(210)/[001], and Σ3(112)/[$1\bar{1}0$].[136,138] At present, a thorough characterization of GBs in LLZO has not yet been reported; however, the geometries examined here are likely to be relevant boundaries, as they have been identified as low energy orientations in BCC metals,[136,138] and the Zr sub-lattice in

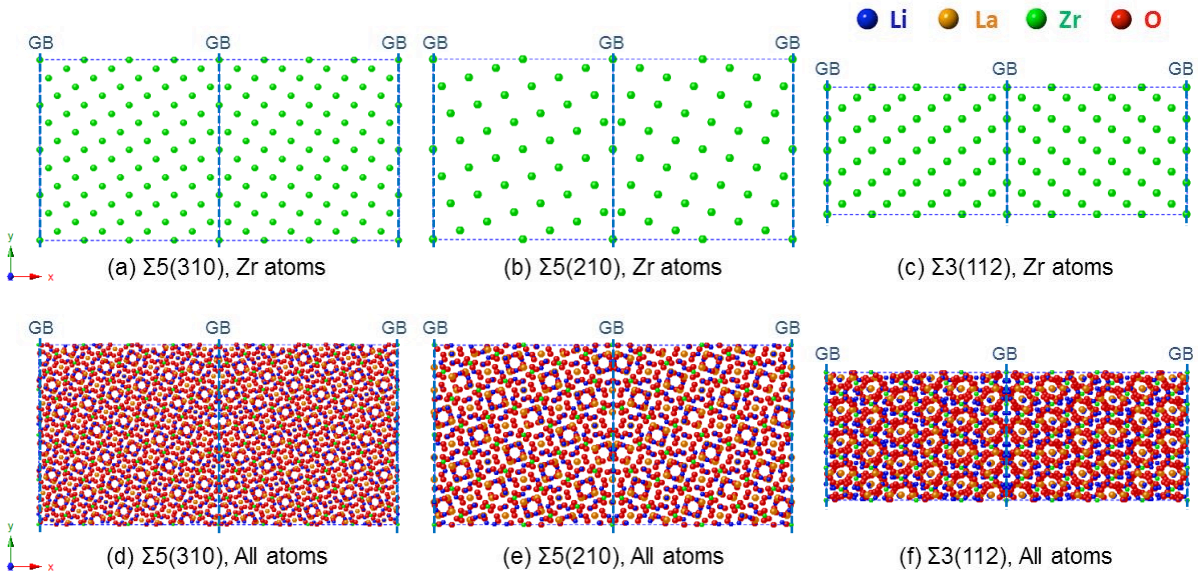

Figure 6.1 Unrelaxed structures of the three symmetric tilt GBs examined in this study: (a,d) Σ5(310), (b,e) Σ5(210), and (c,f) Σ3(112). Panels (a)-(c) illustrate the coincident-site nature of these GBs, which arises from the BCC Zr sublattice.

LLZO is BCC. The low energies of these GB suggest that they are likely to be present in samples processed at high temperatures, such as in hot-pressing.[56,136]

Figure 6.1 shows the structure of the initial (unrelaxed) GB computational cells. The cells contain 160 (Σ5(310)), 80 (Σ5(210)), and 96 (Σ3(112)) formula units of LLZO, respectively. All cells contained stoichiometric quantities of LLZO. Geometry optimization calculations were performed using the conjugate gradient algorithm implemented in LAMMPS.[86]

The energies of the GBs were evaluated (following geometry optimization) according to:

$$\gamma_{\mathrm{GB}} = (E_{\mathrm{GB}} - nE_{\mathrm{Bulk}})/2A \tag{6.1}$$

where E_{GB} is the total energy of the GB-containing cell, n is the number of LLZO formula units in that GB cell, E_{Bulk} is the total energy per formula unit of bulk LLZO, and A is the area of GB plane. The factor of 2 accounts for the fact that each simulation cell contains 2 GBs. A supercell based on a 3 × 3 × 3 replication of the conventional unit LLZO cell was used for bulk LLZO.

Molecular dynamics and Monte Carlo simulations were conducted using LAMMPS.[86] All calculations were performed using a force-field based on Morse-type interactions derived from *softBV* bond valence parameters.[83–85] Prior calculations with this force field yielded good agreement with measured static and dynamic properties of LLZO.[85,98]

After an initial geometry optimization, the GB-containing and bulk LLZO cells were heated to selected target temperatures using the NPT MD ensemble with a heating rate of 1 K/ps. This procedure accommodates thermal expansion and volume changes associated with the presence of the GBs. The time step for MD was 2 fs. Upon reaching the target temperature (ranging from 700 to 1100 K), the cells were then equilibrated with MD using the NPT and (subsequently) NVT ensembles for 3 ns for each ensemble. Next, NVT Monte Carlo simulations were performed using the Metropolis algorithm, with a maximum displacement value, r_{max} = 0.5 Å, selected to achieve a displacement-acceptance ratio of approximately 0.1. More than 10^7 MC move attempts were performed for each GB cell; the goal of the MC calculations is to establish the stoichiometry of the GB region, which can potentially differ from the bulk stoichiometry due to segregation. The composition as a function of position normal to the GB plane was obtained by averaging within 60 contiguous rectangular regions in the MC-equilibrated cells.

Finally, the diffusivity of Li was calculated using NVT MD at five temperatures: 700, 800, 900, 1000, and 1100 K. Supercells built from 1 × 1 × 4, 1 × 2 × 4, and 1 × 2 × 3 replicas of the MC-equilibrated cells (resulting in 640, 640, and 576 f.u. of LLZO) were used for the Σ5(310), Σ5(210), and Σ3(112) systems, respectively. The diffusion coefficient was obtained by evaluating the mean squared displacement (MSD) of Li ions over a time *t*,

$$D = \frac{1}{2dt}\langle[\boldsymbol{r}(t + t_0) - \boldsymbol{r}(t_0)]^2\rangle \tag{6.2}$$

Here, d is the dimensionality of the system, t_0 is the initial time, and the angled brackets indicate an average over all Li ions. Following a 1 ns startup period, MSD data was collected over a 5 ns MD window. Three NVT calculations of the MSD were performed for each simulation using different initial velocities; the standard deviations of these runs were used to establish error bars about the mean diffusivities. The diffusivity at room temperature was evaluated by extrapolating higher-temperature data collected between 700 and 1100 K. This extrapolation is necessary because the cubic phase of undoped LLZO is unstable with respect to the lower-conductivity tetragonal polymorph at room temperature. The diffusivity of Li-ions near the GB and in the bulk region was distinguished by dividing the space within the cells into 10 adjacent, non-overlapping rectangular regions. Atoms were assigned to a region based on their position at the end of the 1 ns startup MD phase.

Although all Li-ions in bulk LLZO are typically considered to be mobile, this assumption may not be valid near GBs due to the distinct atomic structure of the GB plane. The possibility for immobile Li was assessed by calculating the mobility of each Li ion. More specifically, a given Li-ion was defined as immobile if its MSD was always less than 4 $Å^2$ when assessed at 0.5 ns intervals within the 5 ns MD window. As shown below, this analysis confirms that essentially all Li in bulk LLZO are mobile, whereas a significant fraction of Li at GBs is immobile.

6.3 Results and Discussion

6.3.1 The Energetics and Composition

GB energies and excess volumes for the three systems described above were evaluated following geometry optimization at zero Kelvin. The calculated excess volumes for the Σ5(310), Σ5(210), and Σ3(112) GBs are, respectively, 313, 243, and 10 $Å^3$. These volumes are a small fraction – 1%

or less – of the total volume of the GB-free cell. The corresponding GB energies are 1.36, 1.39, and 1.01 J/m^2. The observed correlation between the GB energy and excess volume is consistent with previous calculations on Cu and Ni GBs,[139] where the Σ5 systems exhibited larger energies and excess volumes compared to the Σ3 system. Similarly, the trend in LLZO GB energies is in good agreement with calculations on the same GBs in BCC Fe, where the energies for Σ5(310) and Σ5(210) were reported to be higher than that of Σ3(112).[136,138]

Monte Carlo equilibration at 1000 K resulted in more uniformity and a reduction in magnitude of the GB energies and volumes. Relaxation of the MC-equilibrated GBs yielded excess volumes of 30, 80, and 13 Å^3 for the Σ5(310), Σ5(210), and Σ3(112) GBs, with corresponding GB energies of 0.73, 0.52, and 0.54 J/m^2. The reductions in GB volume and energy are a consequence of (local) changes to the composition in the GB plane that occur during the MC equilibration.

All atoms are uniformly distributed in the as-built cell. However, changes in the composition profiles begin to emerge following the initial structure relaxations. These effects are further magnified following heating via NPT MD and following MC calculations. Figure 6.2

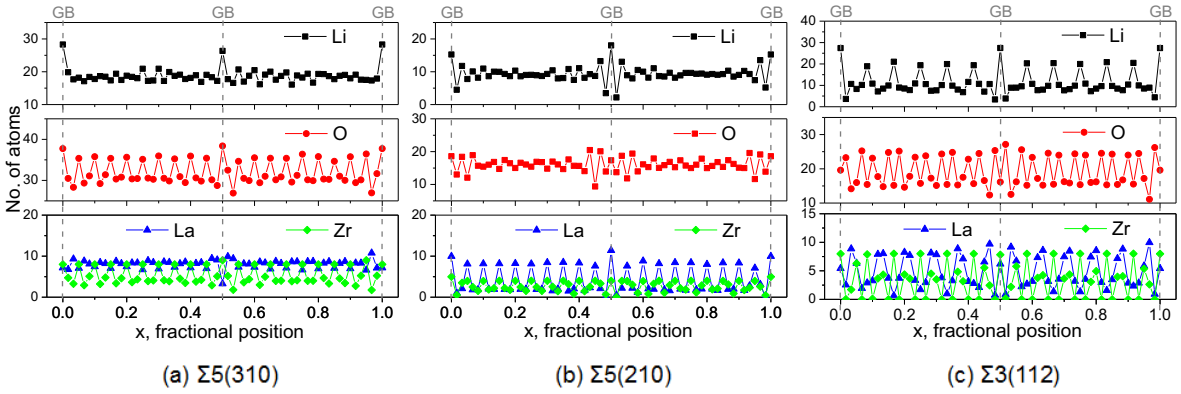

Figure 6.2 Calculated average composition of Li (black), O (red), La (blue), and Zr (green) as a function of position normal to the GB plane (x axis) at 1000 K for supercells containing (a) Σ5(310), (b) Σ5(210), and (c) Σ3(112) GBs.

shows the average equilibrium composition predicted by MC as a function of position normal to the GB plane at 1000 K for each GB. For all GBs examined, the concentration of lithium and oxygen in/near the GB is predicted to exceed that in the bulk region. Changes to the Zr and La concentrations in the GB region are also evident in Figure 6.2, but appear to be relatively small.

The ratio of the number of Li in the immediate GB region, N_{Li}(GB), to the average value in the bulk, N_{Li}(avg. bulk): $\Gamma_{Li} = N_{Li}(GB)/N_{Li}(avg.\ bulk)$ was computed to approximately quantify GB segregation. For the Σ5(310), Σ5(210), and Σ3(112), GBs we obtain Γ_{Li} values of 1.47 1.79, and 2.43, respectively. Evaluating the same ratio for oxygen, Γ_O, yields: 1.18, 1.11 and 0.93. (The slight decrease in oxygen content in the Σ3(112) boundary is due to the sampling region being narrowly centered (1.06 Å width) on the GB plane; in this GB the enrichment of oxygen occurs in the first sub-layer outside of the boundary plane.) The co-segregation of Li cations and O anions would maintain local electroneutrality in the boundary region, and suggests the formation of new GB phases with an approximate composition of Li_2O.

Our observation of deviations from the bulk stoichiometry at GBs in LLZO is consistent with prior reports involving other oxides. For example, yttrium enrichment at GBs has been observed in Y-doped $BaZrO_3$[140] and Y-stabilized zirconia (YSZ)[141]. Similarly, oxygen deficiencies have been reported at GBs in $BaTiO_3$[142] and $SrTiO_3$[143]. Differences in GB chemical composition (relative to bulk) correlate with decreased oxygen transport behavior near GBs in YSZ and $SrTiO_3$.[132,133]

The presence of non-stoichiometric compositions at GBs in LLZO could impact Li ion diffusion. To explore this possibility, the transport properties of Li ions in the GB region were evaluated using MD simulations.

6.3.2 Li-ion Trajectory

The GB compositions predicted by MC equilibration were used as input configurations to MD calculations. The trajectories of Li ions were examined to clarify the impact of GBs on transport. Figure 6.3 illustrates trajectories recorded during 5 ns MD simulations at 700 K for the three GB systems. (A trajectory is a record of the instantaneous locations of the Li ions during the MD time window. Species with a high diffusivity will exhibit a connected, percolating trajectory; in contrast, slowly diffusing components will exhibit gaps in its trajectory.) The trajectory images indicate fragmentation of the Li-ion diffusion path across, and within, the GB plane. Figure 6.3a-c illustrates the Li-ion trajectories as viewed along the GB tilt axis (i.e., along the z-direction). Compared to the bulk region, is clear that the trajectories are more fragmented in the immediate vicinity of the GB. Figure 6.3d-f depicts the trajectories in the GB plane as viewed along a direction parallel to the GB normal (i.e., along the x-direction). (The region plotted corresponds to the red rectangular area shown in Figure 6.3a-c.) For comparison, the trajectories in similarly-oriented bulk regions, corresponding to the regions in the black rectangles in Figure 6.3a-c, are shown in Figure 6.3g-i. These images convey a disruption to the connectivity of the Li-ion trajectory within the GB, suggesting a local reduction in Li-ion mobility.

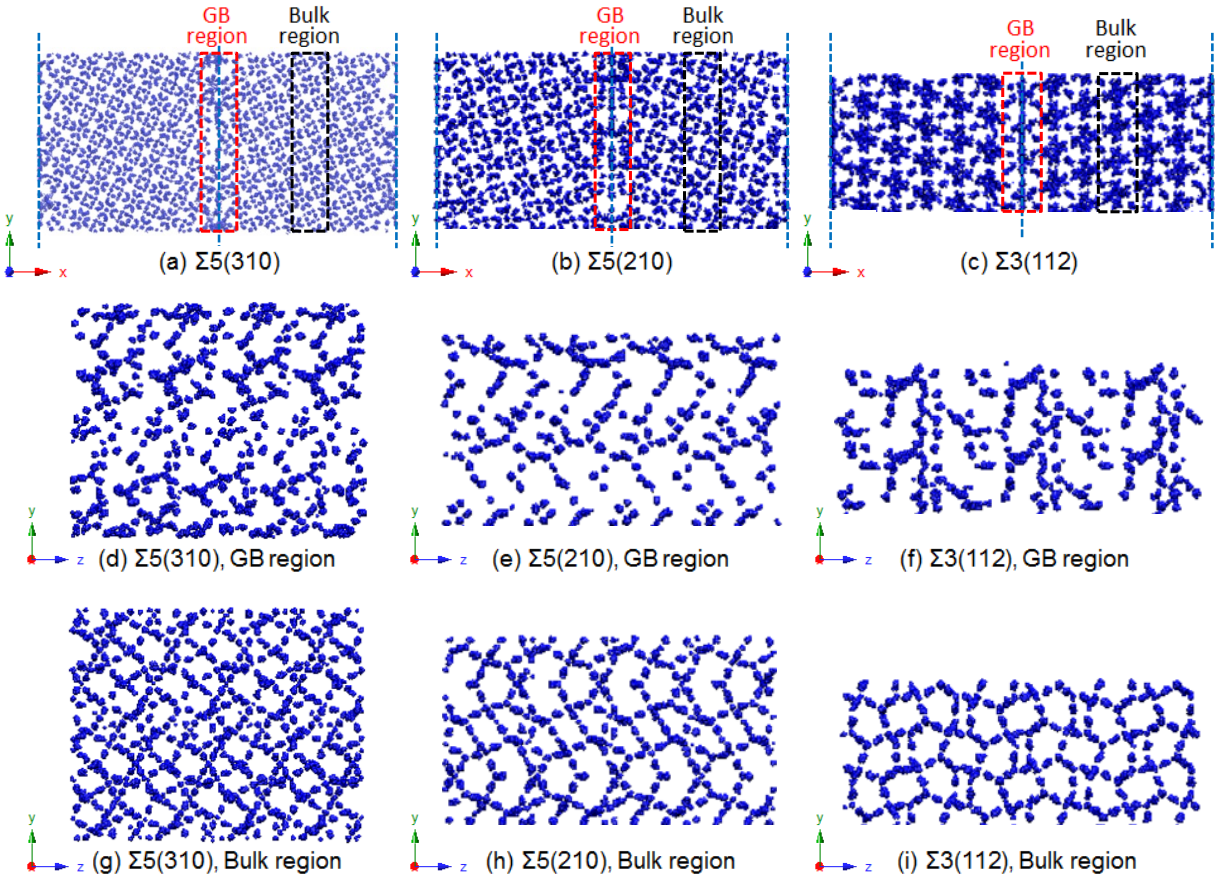

Figure 6.3 Li-ion trajectories for the GB simulation cells plotted over a 5 ns MD window at 700 K: (a-c) view along the GB tilt axis (z direction); (d-f) view normal to the GB plane (x direction) for a region centered on the GB (0.45<x<0.55) corresponding to the red dashed boxes in (a-c); (g-i) view normal to GB plane for a representative bulk region (0.7<x<0.8) corresponding to the black dashed boxes in (a-c).

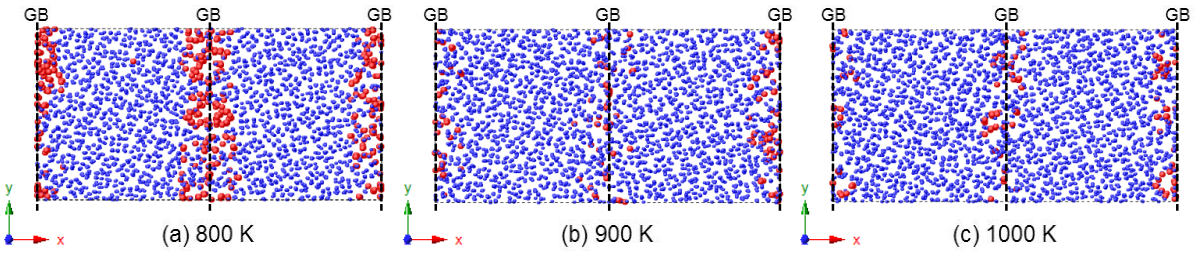

Figure 6.4 Mobile (blue) and immobile (red) Li ions in the Σ5(310) GB simulation cell during 5 ns of MD at 800-1000 K. For clarity, the size of the mobile Li atoms is reduced.

Another strategy for assessing the impact of GBs on Li-ion transport is to identify the location of Li-ions exhibiting low mobility. Low-mobility atoms were previously defined as those having a MSD that is always less than 4 $Å^2$ when assessed at 0.5 ns intervals in a 5 ns MD window. To place this threshold MSD in context, we note that 97.2% of the Li in bulk LLZO have MSDs larger than 4 $Å^2$ at 700 K. Figure 6.4 illustrates the location of mobile (blue) and immobile (red) Li-ions in the Σ5(310) GB cell at temperatures ranging from 800 to 1000 K. The data clearly indicate that immobile Li exists in the simulation cells, and is confined to the GB region. Moreover, the amount of immobile Li increases with decreasing temperature, as expected.

Figure 6.5 illustrates the percentage of immobile Li as a function of position and temperature in the Σ5(310) simulation cell. The plot shows sharp increases in immobile Li in the GB region, consistent with the behavior shown in Figure 6.4. At the lowest temperature examined, 700 K, approximately 70% of the Li in the GB region is immobile. Similar behavior is observed for the other two GBs: immobile Li accounts for about 70% of the Li in the Σ5(210) boundary, while a smaller fraction of Li, only about 45%, is immobile in the Σ3(112) boundary.

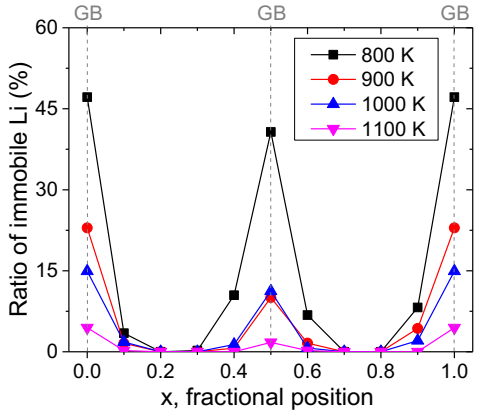

Figure 6.5 Percentage of immobile Li atoms as a function of position normal to GB plane for the Σ5(310) GB during 5 ns MD at 700-1100 K.

The higher mobility in the Σ3(112) boundary correlates with its smaller excess volume, and will be shown to follow trends in the activation energy and diffusivity across the three boundaries.

6.3.3 Li-ion Diffusivity

Figure 6.6 summarizes the calculated Li-ion diffusivity data for the GB-containing simulation cells. Panel (a) displays the total diffusivity for each GB system as a function of position in the cell at 1000 K. In addition, the total diffusivity in the bulk and GB regions is reported in Table 6.1 at 300, 700, and 1000 K. The data in Figure 6.6a show that diffusivity is highest in the bulk regions, and declines in the GB region. Similar trends hold at 700 and 300 K, indicating that diffusion at these GB is slower compared to the bulk. Nevertheless, the extent of this reduction varies significantly across the different GBs, and (as expected) is also temperature dependent. For example, as shown in Table 6.1, GB diffusion at 1000 K is largely independent of GB type, and only 2-3 times smaller than in the bulk. At 700 K GB diffusion is 5 and 2 times smaller for

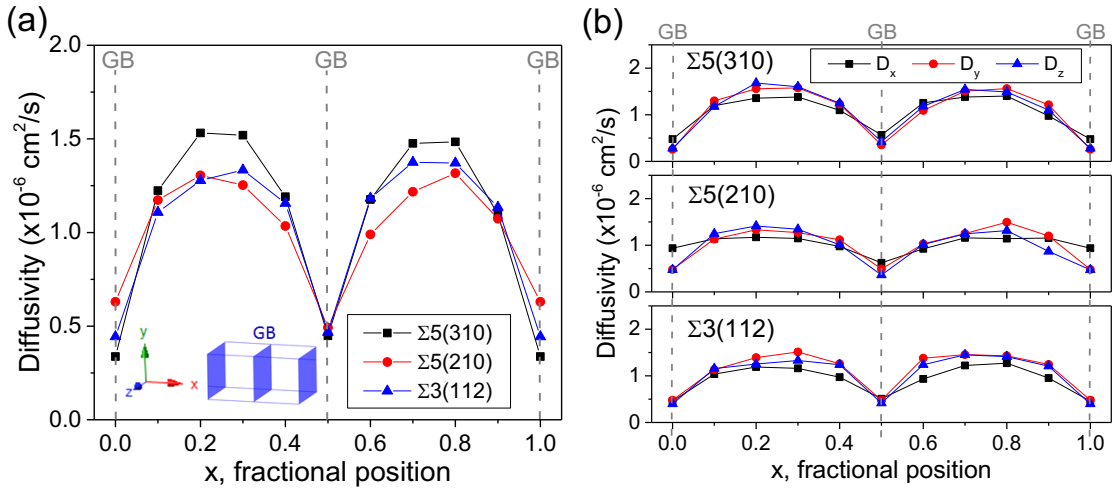

Figure 6.6 Calculated Li ion diffusivity for the three GB cells. (a) Total diffusivity, and (b) diffusivity decomposed along each Cartesian direction at 1000 K as a function of position normal to the GB plane.

the Σ5 and Σ3 boundaries, respectively. We therefore conclude that at these higher temperatures GBs slow Li-ion diffusion only slightly.

Table 6.1 Calculated transport properties (activation energy for diffusion, E_a, and diffusivity, D) in bulk LLZO and in three GBs. Li-ion diffusivities are reported for calculations at 700 and 1000 K, and extrapolated to 300 K. The total diffusivity (D) and the diffusivity projected along the three Cartesian coordinates are reported: D_y and D_z correspond to diffusion within the GB plane; D_x corresponds to diffusion across the GB plane.

System	E_a (eV)	T = 1000 K				T = 700 K				T = 300 K			
		D	D_x	D_y	D_z	D	D_x	D_y	D_z	D	D_x	D_y	D_z
		(10^{-7} cm^2/s)				(10^{-7} cm^2/s)				(10^{-13} cm^2/s)			
Bulk	0.52	13.5	-	-	-	1.01	-	-	-	9.16	-	-	-
Σ5(310)	0.64	4.30	5.57	3.61	3.72	0.22	0.24	0.17	0.24	0.15	0.11	0.10	0.28
Σ5(210)	0.71	5.50	7.35	4.90	4.23	0.17	0.21	0.16	0.14	0.03	0.05	0.02	0.02
Σ3(112)	0.52	5.10	5.40	5.35	4.55	0.50	0.18	0.81	0.52	4.71	0.04	40.0	8.12

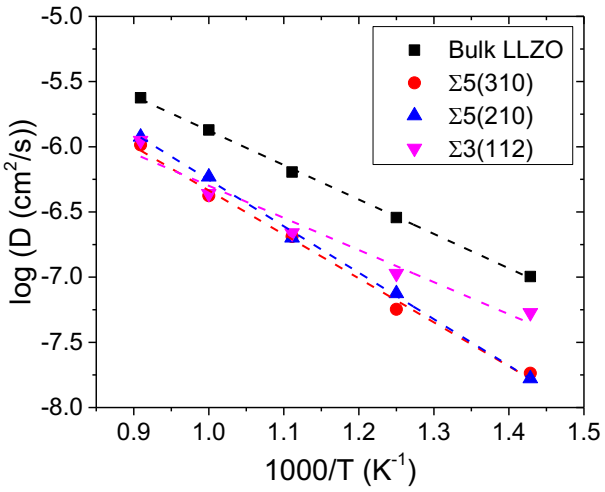

Figure 6.7 Arrhenius plots for Li-ion diffusivity in the GB regions over the temperature range 700 K to 1100 K compared to that in bulk LLZO.

While diffusion in bulk LLZO is isotropic,[93] the distinct atomic structure near the GB could give rise to local anisotropic behavior. For example, fast diffusion along the tilt axis has been observed in some GBs.[144,145] To assess the possibility for anisotropic GB diffusion, the total diffusivity at 1000 K is decomposed in Fig. 6.6b into components along each of the Cartesian directions and as a function of position in the simulation cells. A summary of the directionally-decomposed diffusivities in the GB region for all three boundaries is given in Table 6.1 at 300, 700, and 1000 K. Diffusion within the GB plane corresponds to the y-z plane, with the tilt axis parallel to the z-axis; diffusion in the x-direction would cross the GB plane.

Figure 6.6b shows that at 1000 K there is little evidence of anisotropic diffusion in any of the GBs examined. For the Σ3 boundary, however, evidence of anisotropy begins to appear at 700 K. More specifically, slower diffusion is observed across the GB plane (i.e., in the x-direction), while diffusion in the GB plane approaches rates seen in the bulk. Anisotropy in the Σ3 system is magnified at 300 K (Table 6.1), where trans-boundary diffusion is predicted to be 200 times slower than bulk, while intra-planar transport is equal to or faster than the bulk. Figure 6.7 shows Arrhenius plots for Li-ion diffusivity within the three GBs and bulk LLZO for T = 700–1100 K. The activation energies for diffusion, E_a, were extracted from the slope of these data, and are reported in Table 6.1. For bulk LLZO the calculated E_a of 0.52 eV is in good agreement with prior studies of LLZO in this temperature range.[85]

Diffusion within the GBs is predicted to exhibit activation energies that are equal to or larger than those for bulk diffusion. In the case of the Σ3 boundary, Fig. 6.7 shows a similar slope in the diffusivity *vs.* inverse temperature for bulk LLZO and for this GB. This behavior is consistent with the identical activation energies predicted, 0.52 eV, for these systems. The slightly slower diffusion in the GB illustrated in Fig. 6.7 *vs.* bulk must therefore result from a

smaller prefactor, D_0, in the expression $D(T) = D_0 \exp(-E_a/k_B T)$. Extrapolating the Arrhenius plot for the Σ3 GB to 300 K shows that its total diffusivity is only a factor of 2 smaller than the bulk (Table 6.1). The limited impact of this GB on diffusivity is likely a reflection of its similar structure to that of bulk LLZO. For example, of the boundaries examined, the density of coincident sites (1/3) is the largest in the Σ3 GB, while its excess free volume is the smallest.

As for the two Σ5 boundaries, diffusion in these systems exhibit higher activation energies of 0.64 and 0.71 eV, reflecting their steeper slopes relative to bulk LLZO in the Arrhenius plot. While the diffusivity associated with these boundaries is similar to the Σ3 system at higher temperatures (>900 K), the Σ5 boundaries retard Li-ion diffusion to a greater extent at low temperatures. For example, extrapolation of the Arrhenius data to 300 K reveals that the Σ5 boundaries have diffusivities that are up to 2 orders of magnitude slower than the bulk. The larger slow-down in diffusion in the Σ5 boundaries can be traced to their lower density of coincident sites (1/5), and larger excess volumes. Both of these properties imply a larger disruption to the bulk LLZO crystal structure in the GB region (compared to the Σ3). Since bulk LLZO is a relatively fast Li-ion conductor, disruptions to its structure are expected to slow Li transport by an amount proportional to the degree of disruption.

Taken together, our calculations suggest that low-energy GBs provide a 'mixed' contribution to Li-ion transport in LLZO. That is, diffusion is generally faster (i.e., comparable to bulk) in compact boundaries, while diffusion is significantly retarded in boundaries with larger excess volumes. The opposing impact of these boundaries indicates that the net effect of GBs on Li-ion transport could be modest in samples that are processed under conditions amenable to achieving a high fraction of low-energy, compact boundaries. This observation is consistent with

experimental measurements showing that the GB resistance in LLZO is relatively small in samples that are processed at high temperatures.[56]

Although the low energies of the GBs studied here suggest that they will be present in annealed samples,[136] lower-temperature synthesis routes could generate higher-energy GBs with less-compact structures. Such GBs are expected to have a larger impact on Li-ion conductivity, and therefore should be considered in future studies.

Catarelli *et al*.[146] used scanning electrochemical microscopy to map the local Li-ion conductivity across the surface of a polycrystalline LLZO sample comprised of relatively large grains (~150 um average diameter). Their study revealed that the resistance of the GBs to Li-ion migration was generally greater than in the bulk, consistent with the present study. Moreover, Catarelli and co-workers observed that the GB resistance varied considerably across the GB regions, suggesting a dependence on GB structure and composition. A structural dependence of GB diffusion is also predicted by the present computational results. Regarding the influence of composition on GB transport, the present atomistic models have emphasized transport in pristine (cubic) LLZO. Thus, the impact of adventitious impurities and intentional additives (e.g., dopants such as Al and Ta, or sintering aides) on GB phenomena are not considered here. While an examination of pristine LLZO is important for establishing the intrinsic properties of its GBs, more complex behavior with respect to GB composition can be expected in experiments. For example, several studies have reported Al enrichment at grain boundaries in Al-doped LLZO.[147–153] Similarly, the presence of impurity phases (Li_2CO_3 and LiOH) at GBs, which result from reaction(s) with air, can also limit ionic conductivity.[62] Computational studies that quantify the impact of segregation and second phase formation at GBs in LLZO would be a helpful next step.

6.4 Conclusions

Recent measurements on the promising solid electrolyte LLZO suggest that grain boundaries contribute to undesirable short-circuiting and resistance in polycrystalline LLZO membranes. Toward the goal of understanding – and ultimately controlling – GB-related phenomena, the present study has examined the energetics, composition, and transport properties of three Σ3 & Σ5 model GBs in LLZO at the atomic scale. Due to their low energies, these boundaries are expected to comprise a significant fraction of the GB network in samples prepared at elevated temperatures. Our Monte Carlo simulations reveal that the GB planes of all boundaries examined are enriched with lithium and oxygen. Molecular dynamics simulations on these off-stoichiometric boundaries were used to assess Li-ion transport within and across the boundary planes.

MD calculations reveal that Li transport is generally slower in the GB region compared to the bulk. Nevertheless, the magnitude of this effect is sensitive to the GB structure and temperature. For example, Li-ion diffusion is comparable in all three GBs at high temperatures (>900 K), and only slightly slower than bulk diffusion. In contrast, room temperature diffusion differs significantly between the Σ3 and Σ5 systems: diffusion in the more compact Σ3 boundary remains relatively fast (~50% of the bulk rate), while transport in the Σ5 boundaries is roughly two orders of magnitude slower than the bulk. These trends are reflected in the activation energies for diffusion, which in the Σ5 boundaries are up to 35% larger than in bulk LLZO, and are equal to the bulk for the Σ3 boundary.

Diffusion within the Σ5 boundaries is isotropic, while anisotropic transport is observed in the Σ3 system at lower temperatures (<700 K). In the latter system, intra-plane diffusion at 300 K is up to 4 times faster than the bulk, while transboundary diffusion is ~200 times slower.

Our observation of mixed GB transport contributions – some boundaries support fast diffusion (comparable to bulk diffusion), while others are slow – is consistent with the moderate GB resistance observed in polycrystalline LLZO samples processed at high temperatures. These data also suggest that higher-energy GBs with less-compact structures should penalize Li-ion conductivity to a greater degree. Additional experimental study is needed to quantify the presence, and characterize the structure, of high-energy boundaries as a function of processing temperature. Such studies would enable computational characterization of those systems, similar to the analyses performed here on low-energy GB. The role of super-valent dopants on GB diffusion should also be examined.

Chapter 7 Grain Boundary Softening, A Mechanism for Lithium Metal Penetration

7.1 Introduction

Given the relative softness of Li metal,[60] it has been proposed that dendrite initiation can be prevented by pairing the Li anode with a stiff solid electrolyte.[15,154] Monroe and Newman used linear elasticity theory to examine the conditions under which a homogeneous polymer SE could suppress dendrite initiation.[15] Their model predicted that a SE whose shear modulus, G, was approximately twice larger (~8 GPa) than that of Li metal should prevent dendrite formation. Nevertheless, Li metal penetration has been recently reported in several SEs, such as β-Li_3PS_4,[155] $Li_2(OH)_{0.9}F_{0.1}Cl$,[156] and $Li_7La_3Zr_2O_{12}$ (LLZO).[49,52,54,127,128,155,157–159] This unexpected behavior occurred despite the fact that the measured densities and moduli for these materials were very high: in the case of LLZO, $G \sim 60$ GPa, which is more than an order of magnitude larger than that of Li metal, while the measured density was 98% of the theoretical value, indicating minimal contributions from porosity. Importantly, the metal penetrants were observed to follow pathways through the SE that coincided with the grain boundary network,[54] or with the location of other microstructural features such as pores or surface cracks.[155,160]

The penetration of stiff ceramic SEs by soft Li is a surprising observation, and raises the question, 'how is this possible?' Experimental data indicating contributions from the SE's grain boundaries, pores, and surface flaws lead us to hypothesize that *microstructural features* play a critical role in the suppression of dendrites. Existing models for dendrite nucleation in the presence of a SE do not account for microstructural inhomogeneities – the SE is typically assumed to be homogeneous.[161,162] Thus, a high shear modulus in the non-defective 'bulk' regions of a SE may be considered as a necessary but insufficient condition for achieving dendrite resistance: contributions from microstructure should also be considered.

Figure 7.1 illustrates three possible scenarios by which microstructural features can promote inhomogeneous Li plating, resulting in metal penetration through a solid electrolyte.

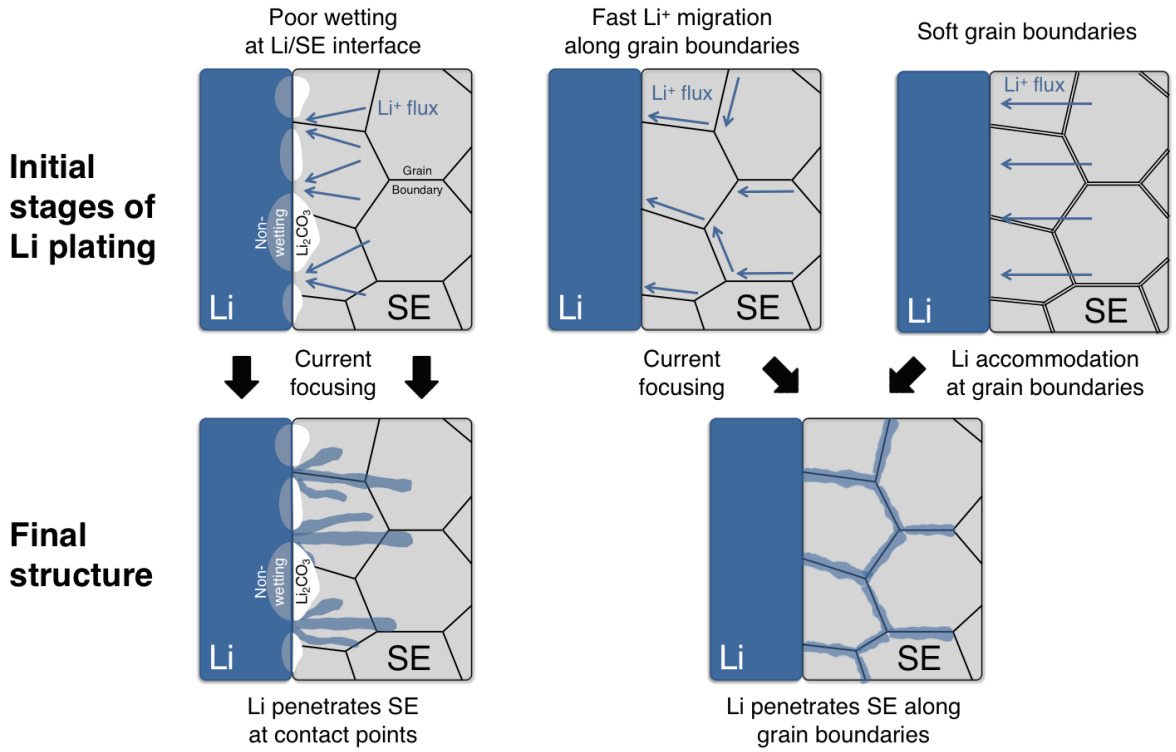

Figure 7.1 Potential microstructural contributions to inhomogeneous Li plating from a solid electrolyte. Left and middle: current focusing mechanisms resulting from poor interfacial wetting (left) or (middle) fast Li migration along GBs. Right: Li penetration along soft GBs.

The first scenario, shown on the left of Figure 7.1, arises from poor wetting at the Li/SE interface.[50,63,163] Previous chapters have shown that Li metal will wet a 'clean' LLZO surface; however, non-wetting behavior is observed when surface contaminant phases such as LiOH and Li_2CO_3 are present. Since Li-ion transport through hydroxides and carbonates is slower than in LLZO, the presence of these contaminants results in focusing of Li-ions towards the limited contact points where the SE directly interfaces with the Li anode. This current focusing results in inhomogeneous electrodeposition of Li, and ultimately to the penetration of Li metal into the SE. A similar mechanism has been proposed for the penetration of sodium metal through β-Al_2O_3.[164] In the case of LLZO, cleaning of the SE surface was found to delay the onset of Li penetration to higher current densities.[63] Nevertheless, dendrites were still observed at current densities (0.6 mA/cm^2) far below those needed for a practical battery (3-10 mA/cm^2).[165] Thus, although increasing interfacial wetting is helpful, it appears to be insufficient on its own to eliminate the dendrite problem: other mechanisms appear to be contributing.

A second scenario resulting in dendrite formation is shown in the middle portion of Figure 7.1. This mechanism also involves current focusing, and is caused by fast Li-ion migration along GBs. In the presence of fast GB transport, Li plating would occur preferentially in regions where GBs intersect the electrode surface. Assuming the arrival rate of Li at these intersections is faster than its lateral migration away (i.e., parallel to the interface), then the resulting 'pile-up' of Li could nucleate dendrites. This 'fast GB diffusion' hypothesis is studied by calculating the rate of Li-ion migration along three low-energy tilt GBs($\Sigma3$ & $\Sigma5$) of LLZO in the previous chapter. MD results revealed that Li transport is generally reduced in the GB region. Thus, current focusing along GBs does not appear to explain Li dendrite penetration.

Here we hypothesize that 'softening' of the SE in the vicinity of GBs provides a mechanism for dendrite penetration. This hypothesis represents a third microstructure-related scenario, and is shown on the right in Figure 7.1. (We speculated that GB-softening could contribute to dendrite penetration in an earlier publication.[166]) Here, 'softening' is defined as a reduction in the elastic moduli close to the GBs. These effects could arise from deviations in density and atomic structure (i.e., less-optimal bonding relative to the bulk) near the GB plane. This scenario is inspired by the elasticity model of Monroe and Newman,[15] yet accounts for inhomogeneities in elastic properties. Unlike the first two scenarios from Figure 7.1, in which current focusing drives inhomogeneous Li deposition, in the present case Li deposition is initially homogeneous (i.e., the Li-ion current is *not* focused). However, as plating progresses, Li will accumulate preferentially in softer regions near electrode/GB junctions via interfacial diffusion away from the stiffer, GB-free regions. The resulting Li protrusions will generate locally stronger electric fields, that will focus subsequent Li deposition. Indeed, prior studies have indicated the possibility of softening at GBs.[167,168] If these effects are also present in SEs, then they could provide an important contribution to the mechanism by which dendrites penetrate SEs.

The research described in this chapter demonstrates that significant softening can occur at GBs in SEs. Adopting LLZO as a model SE, molecular dynamics (MD) simulations on two, low-energy Σ5 tilt and twist GBs are reported. The elastic constants associated with uniaxial strain perpendicular to the GB plane and with shear parallel to the GB were calculated at 300 K. These calculations indicate a severe softening in the immediate vicinity of the GB: elastic constants are observed to be up to 50% smaller at GBs than in the bulk. We propose that nanoscale softening attributed to microstructural features such as GBs may explain *why* these features are susceptible to metal penetration during electrodeposition.

7.2. Methodology

7.2.1 Molecular Dynamics

Elastic properties were evaluated at a pair of low-energy tilt and twist coincident-site (Σ5) GBs, shown in Figure 7.2. GB models were generated by initially rotating two replicas of the unit LLZO cell (i.e., the individual grains) along their [001] axes by 53.1° (relative displacement). The symmetric tilt GB was constructing by cleaving and then adjoining the rotated grains along their (210) planes. Similarly, the twist boundary was formed by cleaving and adjoining the rotated grains along (001) planes.

The low energies of the two GB orientations[136,138] examined here suggest that they are likely to be present in equilibrated LLZO samples.[56,64] For example, earlier studies have shown that Σ5 GBs in body-centered cubic materials exhibit low energies (the Zr sublattice in LLZO is BCC),[136,138] while in oxides the GB habit plane tends to be the same planes as those that minimize the surface energy.[169] The tilt boundary satisfies the first (orientation) requirement, while the twist boundary satisfies both the orientation and surface energy requirement.[61] (The (100) twist boundary plane was previously identified to be low in energy.[61,170])

Figure 7.2 illustrates the computational cells used to model these two GBs. In both cases the cells contain a pair of GBs: one at the cell center (fractional coordinate $z = 0.5$) and one at the cell boundary ($z = 0$). The GB planes have normal vectors that are parallel to the long (z) direction of the cell, allowing for ample space (> 15 nm) and minimum interaction between GBs.

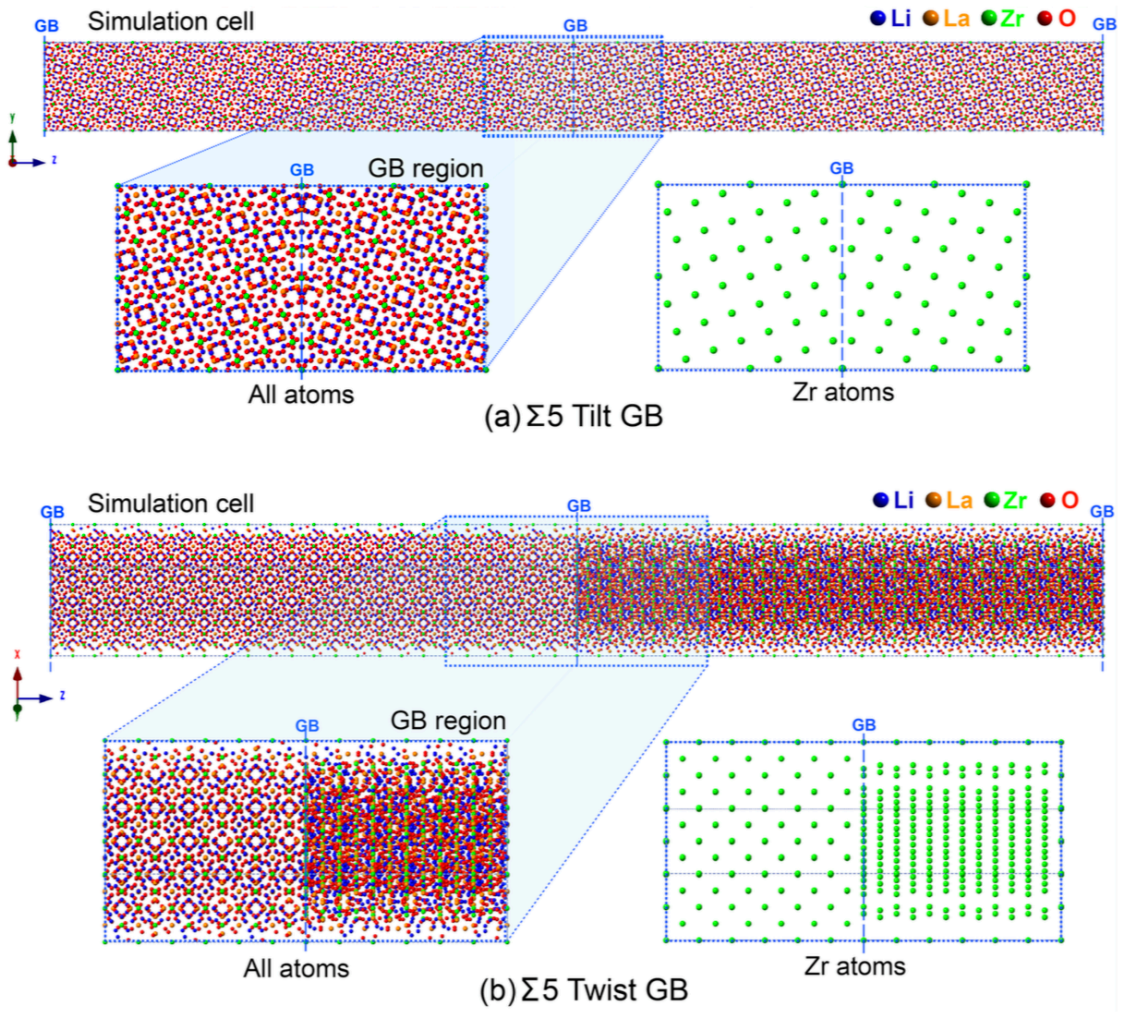

Figure 7.2 Computational models of (a) Σ5 tilt and (b) twist grain boundaries in LLZO. The full simulation cells and magnifications of one of the GB regions are shown in each case are. The coincident site nature of the grains is illustrated by showing only the Zr sublattice sites.

The elastic properties of bulk LLZO and of the two GBs were evaluated using molecular dynamics (MD) simulations, as implemented in the LAMMPS code.[86] The time step for all MD runs was 2 fs. Three force-fields (FFs)[85,171,172] were assessed with respect to their ability to reproduce the bulk elastic properties of LLZO, as previously predicted by first-principles calculations and as measured by experiments.[60,105] In an earlier chapter, the DFT-calculated

elastic properties were in excellent agreement with experimental measurements for Ta- and Al-doped LLZO.[60]

Table 7.1 compares the zero Kelvin and room temperature elastic constants and moduli for bulk LLZO, as calculated using MD, with DFT and experimental data.[173] Out of the three FFs, the potential of Jalem and co-workers[172] yielded the best agreement with the elastic constants predicted by DFT, with a mean absolute deviation of 7%. This inter-atomic potential was adopted for calculations on GB cells. It is based on long-range Coulombic and a short-ranged Buckingham interaction; the cut-off distance for the short-range interaction was set to 10.5 Å.

The equilibrium structure and composition of the GBs was determined using a multi-step procedure similar to that employed in previous analysis of GB transport.[64] After an initial

Table 7.1 Calculated elastic constants, C_{ij}, and moduli (GPa) for cubic LLZO as a function of composition and evaluation method (DFT calculations, MD calculations, and experimental measurements). The percent difference between DFT- and MD-predicted values for pure LLZO are given in parentheses.

System	Method	C_{11}	C_{12}	C_{44}	B	G	E
Al-doped LLZO	DFT (0 K)[a]	187	75	71	112	65	163
Al-doped LLZO	DFT (298 K)[a]					61	155
Al-doped LLZO	Experiment (298 K)[a,b]				100.2, 102.8	58.1, 59.8, 59.6	146.1, 150.3, 149.8
Ta-doped LLZO	DFT (0 K)[a]	170	64	70	99	63	155
Ta-doped LLZO	DFT (298 K)[a]					59	147
Ta-doped LLZO	Experiment (298K)[a]				96.0	55.7, 61.2	139.9, 153.8
Pure LLZO	DFT (0 K)[c]	186	78	73	114	65	163
Pure LLZO	MD (0 K)[c, d]	190 (2%)	115 (47%)	29 (-60%)	140 (23%)	32 (-51%)	90 (-45%)
Pure LLZO	MD (0 K)[c, e]	211 (13%)	95 (22%)	76 (4%)	134 (18%)	68 (5%)	175 (7%)
Pure LLZO	MD (0 K)[c, f]	184 (-1%)	79 (1%)	60 (-18%)	114 (0%)	57 (-12%)	146 (-10%)

a: ref [60], b: ref[105], c: present study, d: ref [85], e: ref [171], f: ref [172]

geometry optimization at zero K, the simulation cells were equilibrated using NPT MD at 300 K for 500 ps. Subsequently, they were heated to 1000 K at a rate of 1K/ps using the NPT ensemble. This procedure accommodates thermal expansion and volume changes associated with the presence of the GBs. Upon reaching 1000 K, isothermal MD was performed in the NPT and (subsequently) NVT ensembles for 500 ps each. Next, to equilibrate the local composition of the GBs, NVT Monte Carlo simulations were performed (10^6 attempts) using the Metropolis algorithm with a maximum atomic displacement of 0.5 Å. The cells were then cooled to 300 K via MD at a rate of 1K/ps and equilibrated at 300 K for 500 ps using NPT-MD with a constant cell shape to suppress the phase transform to the low-conductivity tetragonal phase. Finally, NVT-MD was performed at 300 K for 500 ps. Elastic properties were evaluated by averaging over the last 400 ps of this time window. The computational procedure is summarized in Figure 7.3.

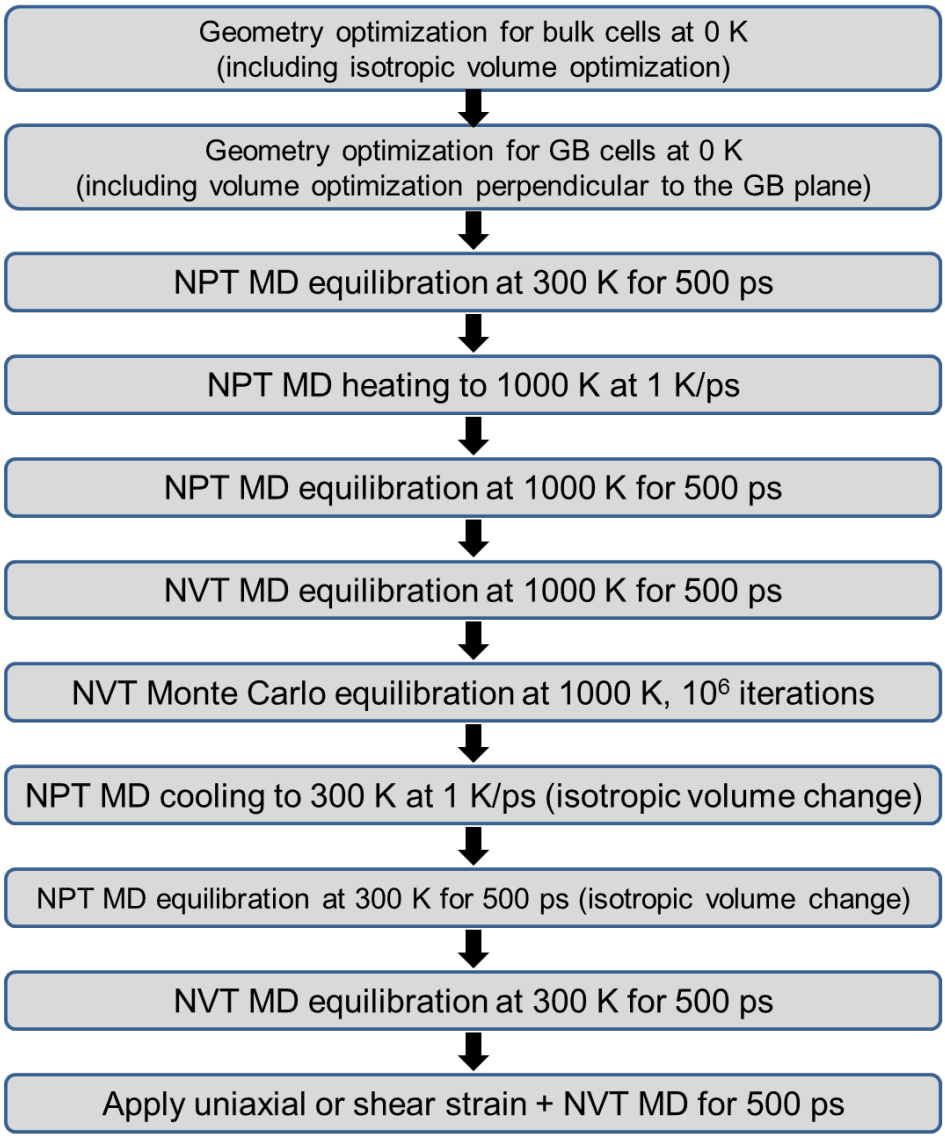

Figure 7.3 Summary of the computational procedure used to evaluate local elastic constants in the grain boundary simulation cells.

7.2.2 Elastic Properties

GB elastic properties were calculated using the methodology described for twist GBs in copper.[167,168] A series of uniaxial or shear strains of magnitude -0.75%, -0.5%, -0.25%, 0.25%, 0.5%, and 0.75% were applied to the boundary of the simulation cell. The stresses associated with the applied strains were obtained as output from the calculations. These global strains generate localized uniaxial strains perpendicular to the GB plane, and shear strain parallel to the GB plane, respectively. Local strains were evaluated as a function of position in the computational cell by measuring the relative positions of planes of La and Zr atoms. For the tilt (twist) GB the unstrained interplanar spacing, $L_{z,0}$, is given by $\sqrt{5}a/4$ $(a/2)$, where a is the lattice constant of the cubic unit cell.

The elastic constant, C_{33}, is associated with uniaxial strain perpendicular to the GB plane (z direction). Changes to the interplanar spacing perpendicular to the GB plane were used to measure local deformations resulting from the global strain, $\varepsilon_{33,0}$. The local uniaxial strain, ε_{33}, is given by $\varepsilon_{33} = \left(L_z - L_{z,0}\right)/L_{z,0}$ where $L_{z,0}$ and L_z are, respectively, the interplanar spacing before and after strain is applied. The local elastic constant is then given by: $C_{33} = \sigma_{33}/\varepsilon_{33,}$ where σ_{33} is the global stress in the z direction.

The elastic constant associated with shear parallel to the GB plane, C_{44}, was calculated by applying a shear strain, $\varepsilon_{44,0}$, to the simulation cell in the y direction. The local shear strain, ε_{44}, can be expressed as: $\varepsilon_{44} = \Delta d_{Ly}/L_{z,0}$. Here $L_{z,0}$ is the interplanar spacing along the z-direction of a given region in the cell before strain is applied, while Δd_{Ly} represents the magnitude of displacement in the direction of the shear (the y-direction in our calculations) across that region. These displacements were measured by tracking the y-components of atom positions on the two

planes that bound a given region in the z-direction. The local elastic constant is then given by $C_{44} = \sigma_{44}/\varepsilon_{44}$, where σ_{44} is the global shear stress.

7.3 Results

Figure 7.4 shows the calculated strain behavior of the Σ5 tilt GB cell under uniaxial loading at 300 K. Figure 7.4(a) presents the local strain as a function of the global applied strain and of position normal to the GB plane. As expected, the local strain in the bulk region is very similar to the global strain. In contrast, the local strain in the immediate vicinity of the GB is much larger than in the bulk, suggesting a softening in the GB region. Figure 7.4(b) shows that the relationships between the local and global applied strain in the bulk and GB regions are in both cases roughly linear for the strains examined here. While the slope of the line fit to the bulk data is approximately unity, for the GB the slope is ~30% steeper, consistent again with GB softening. Finally, Figure 7.4(c) plots the ratio of local to global strain, $\varepsilon/\varepsilon_0$, as a function of position normal to the GB plane. These data were obtained from the slopes of linear fits to the position-dependent local strain (as in Figure 7.4(b)). Factoring in both GBs, Figure 7.4(c) shows that the strain in the GB region is ~40% greater than that of the bulk.

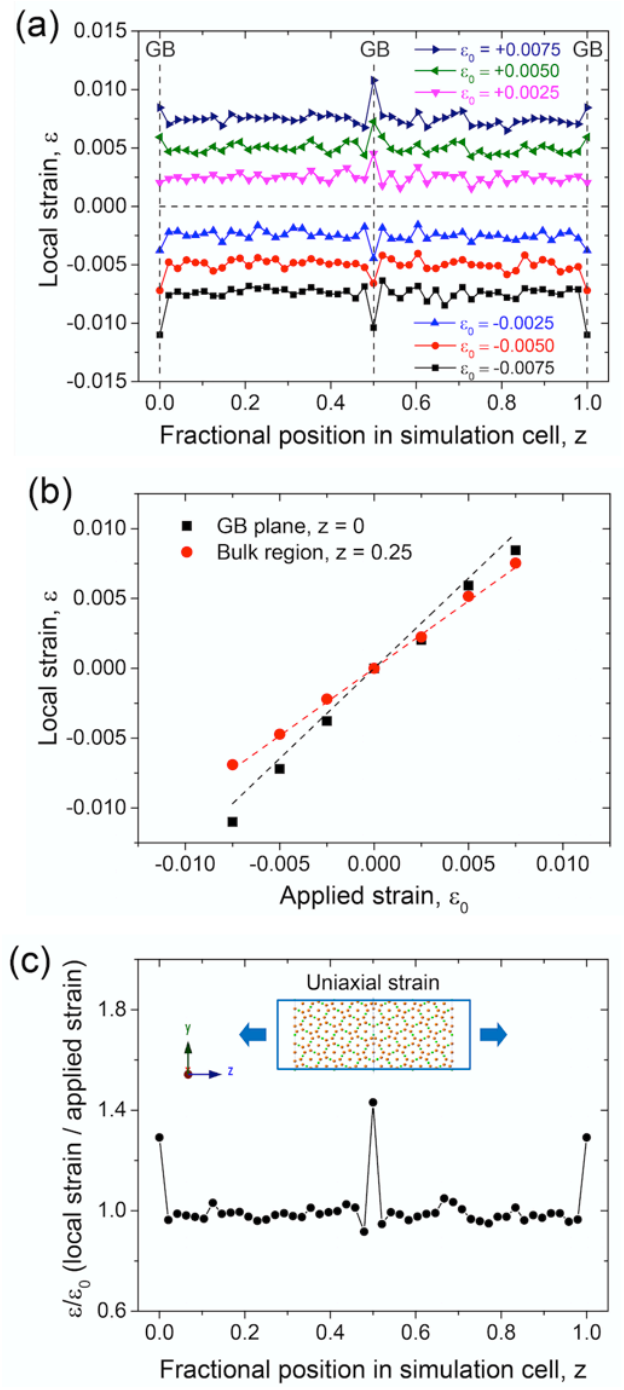

Figure 7.4 Calculated local strains for the Σ5 tilt GB cell at 300 K under uniaxial loading. (a) Local strain as a function of position normal to the GB plane; (b) Relation between local and applied (global) strain in the GB plane at z=0 and in the bulk region (z=0.25); (c) Ratio of local to applied strain as a function of position normal to the GB plane.

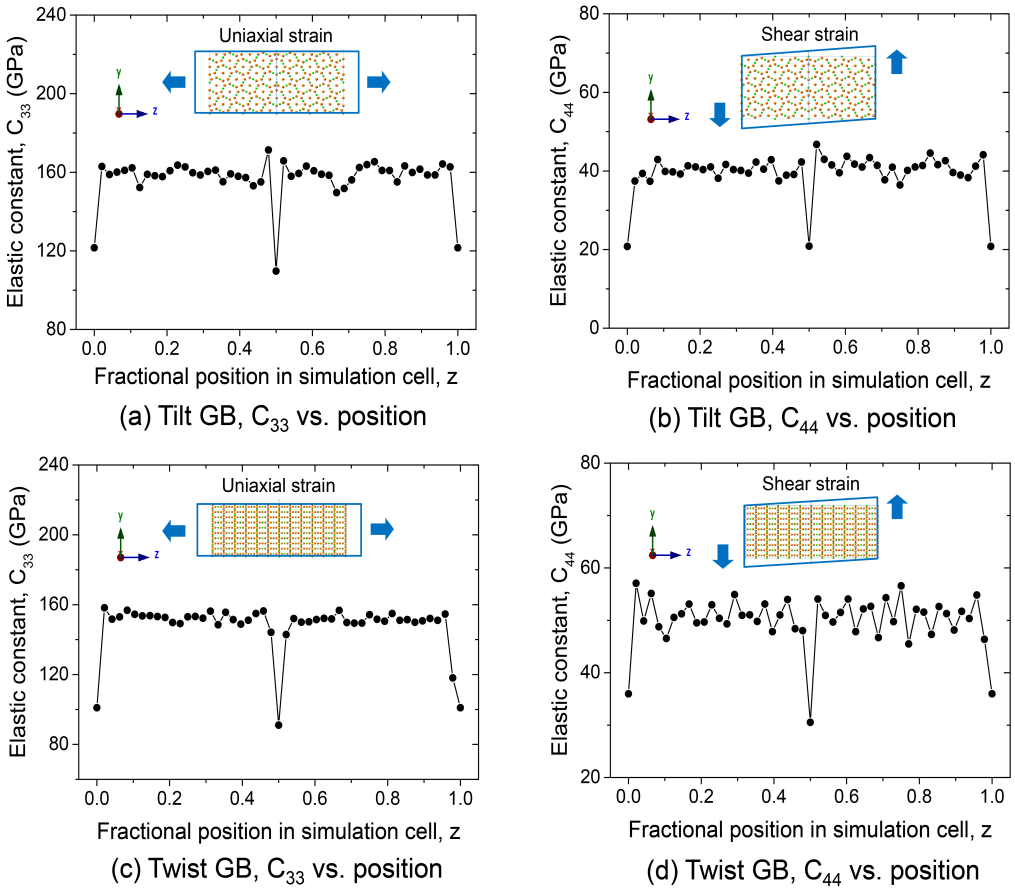

Figure 7.5 Calculated elastic constants C_{33} and C_{44} at 300 K as a function of position normal to the GB planes for the (a, b) the Σ5 symmetric tilt GB cell and (c, d) the Σ5 twist GB cell.

Table 7.2 Calculated elastic constants, C_{33} and C_{44} (in GPa), in the bulk and GB regions for the Σ5 tilt and twist GB simulation cells.

Elastic constant	Σ5 Tilt GB			Σ5 Twist GB		
	Bulk	GB	Δ (%)	Bulk	GB	Δ (%)
C_{33}, uniaxial	159	115	-28	152	96	-37
C_{44}, shear	40	21	-48	51	33	-35

Figure 7.5 plots the elastic constants C_{33} and C_{44} for the tilt and twist GBs as a function of position normal to the GB plane. As previously described, these two elastic constants represent the elastic and shear modulus of the system: $C_{33} \sim E$ and $C_{44} \sim G$. The elastic constant data were calculated by combining strain data with the stress for a given applied strain. A summary of all elastic constants is given in Table 7.2.

Turning first to the elastic constant associated with uniaxial strain, C_{33}, Figure 7.5a,c show that C_{33} is approximately constant in the bulk regions of the computational cells, and is equal to 159 and 152 GPa. This elastic constant is predicted to be much smaller in the GB regions: a value of 115 GPa is obtained for the tilt GB, with an even smaller value of 96 GPa predicted for the twist system. These values are 28% and 37% smaller, respectively, than the corresponding bulk values.

Similarly, the elastic constant associated with shear deformation, C_{44}, is predicted to be significantly smaller in both classes of GBs: in the bulk, C_{44} = 40 and 51 GPa, whereas in the tilt and twist GBs values of 21 and 33 GPa are found, respectively. Thus, the GBs are 48% and 35% softer with respect to shear than is the bulk. In total, our calculations predict that GBs in LLZO can have elastic moduli that are approximately 25 – 50% smaller than the bulk.

7.4 Discussion

Could GB 'soft spots' explain Li metal penetration in LLZO? A strict interpretation of the Monroe-Newman criterion stipulates that a viable SE should have a shear modulus, *G*, that is approximately twice that of Li metal. Assuming Li can be treated as an isotropic polycrystalline metal, then $G_{Li} \sim 4$ GPa.[60] Thus, a solid electrolyte with $G_{SE} > \sim 8$ GPa = $2G_{Li}$ should be capable of suppressing dendrite initiation. Even though our calculations predict that GBs in LLZO are up

to ~50% softer than the bulk, the smallest value for C_{44} obtained for the GBs examined here, 21 GPa, easily surpasses the $2G_{\mathrm{Li}}$ threshold. Therefore, it would seem that GBs – although significantly softer than the bulk – are not 'soft enough' to serve as initiation points for dendrites.

A few caveats to this conclusion should be acknowledged, however. First, treating the Li anode as an isotropic solid may be overly simplistic. For example, our prior study reported that the elastic properties of Li are highly anisotropic:[60] the resolved shear modulus of Li ranges from a minimum of 1.5 GPa in the <111> direction to a maximum of approximately 11 GPa along <100>.[60] Doubling the largest of these values results in a threshold of 22 GPa, a value which is larger than the shear modulus predicted for the Σ5 tilt boundary, 21 GPa. Hence, this GB does not meet the Monroe-Newman criterion.

Second, as mentioned earlier, the atomic-scale structure and orientation distribution of GBs in LLZO is at present unknown. The low energies of the two GB orientations examined here suggest that they are plausible structures in equilibrated LLZO samples, such as those processed using at high temperatures. Nevertheless, the present GBs represent idealized systems with relatively low degrees of disorder and excess volume. It is therefore possible that they represent a best-case scenario: softening in less-ordered, general GBs could be more severe and extend to larger spatial regions. Higher energy GBs with less-compact structures could be generated via lower temperature synthesis routes. Solute segregation and impurity phases at GBs,[58,62,147–149,151,153] such as hydroxides and carbonates, could also impact elastic properties. Further study is needed to assess these factors.

Third, although softening is demonstrated here for GBs, it is reasonable to speculate that this behavior could also apply to other microstructural features that exhibit local disruptions to crystallinity and/or density, such as at surface scratches or near pores.[155,160]

Finally, given that real electrode/electrolyte interfaces are often structurally and compositionally complex, it is reasonable to consider whether the Monroe & Newman criterion (i.e., ~$2G_{Li}$) should be interpreted quantitatively, or instead is best employed as a qualitative guideline. The latter interpretation suggests that local decreases in elastic properties, such as those caused by microstructural features, could be sufficient to promote metal penetration even if the local modulus is larger than $2G_{Li}$.

7.5 Conclusions

Inhomogeneities in the elastic properties of a solid electrolyte were examined in the context of Monroe and Newman's elasticity model for dendrite initiation. Molecular dynamics simulations were used to evaluate elastic moduli near grain boundaries in the prototype solid electrolyte, LLZO. These calculations reveal that moduli can be as much as 50% smaller at grain boundaries than in the bulk. This inhomogeneous softening is expected to result in accumulation of Li at electrode/grain boundary junctions during electrodeposition. Thus, grain boundary 'soft spots' may contribute to the mechanism by which soft lithium metal can penetrate an ostensibly stiff solid electrolyte. Additional study is needed to characterize the elastic properties of other types of grain boundaries, account for potential variations in grain boundary composition arising from impurities or segregation, and to explore effects in solids beyond LLZO.

This work highlights scenarios by which a solid electrolyte's microstructure can contribute to inhomogeneous electrodeposition and dendrite penetration. At present these scenarios have received limited attention in the battery literature. A better understanding of the role of microstructure will aid in the design of long-lived solid state batteries.

Chapter 8 Conclusions and Next Steps

8.1 Conclusions

At present, LLZO is one of the most promising Li solid electrolytes due its favorable combination of high conductivity and chemical stability against Li metal. However, there are several challenges that limit the use of LLZO in practical batteries. These include: reactivity with air, adhesion/wettability at electrode interfaces, interfacial resistance, inhomogeneous transport and mechanical properties arising from microstructural imperfections, and dendrite suppression. As a step towards overcoming those challenges, the work presented in this dissertation characterizes several properties of LLZO using density functional theory and molecular dynamics calculations. The knowledge gained will enable the development of rational strategies for improving solid state batteries employing LLZO, as well as for other classes of solid electrolytes.

Firstly, the electrochemical stability window of LLZO was examined using DFT calculations. The EW determines an electrolyte's resistance to undesirable electronic transport, and, by extension, controls phenomena such as short-circuiting and self-discharge. The position of the EW also impacts electrochemical oxidation and reduction of LLZO by the electrodes. DFT calculations revealed that LLZO is an excellent electronic insulator with the large band gap (6.4

eV from GW calculations). An evaluation of the absolute positions of the band edges lends further supports the observation of limited electronic transport in LLZO. These calculations also indicate that LLZO is stable against p-type conduction up to ~4 V vs. Li/Li^+ arising from hole injection from oxidation by the positive electrode. In addition, the conduction band minimum in LLZO is predicted to lie slightly above Li/Li^+, suggesting moderate stability against n-type charge injection from the anode. These data indicate that a wide EW window is an intrinsic property of LLZO, and need not arise from kinetic stabilization resulting from new phase formation at electrode interfaces.

Next, the impact of air exposure on LLZO surface was explored by calculating the thermodynamic driving force (Gibbs free energy of reaction, ΔG) for the hydration and carbonation of LLZO. DFT calculations indicate that the Li^+/H^+ ion exchange pathway is a thermodynamically favorable route for the formation of a Li_2CO_3 layer on the surface of LLZO. On the other hand, direct hydration and carbonation of LLZO is found to be thermodynamically unfavorable. The resulting contamination layers contribute to high interfacial resistance between Li and LLZO, presumably due to poor wettability. To test this hypothesis, the Li wettability of the LLZO surface was predicted. Calculations indicate that Li strongly wets pristine LLZO, but not Li_2CO_3 and LiOH, which is consistent with the high interfacial resistance in the presence of a contamination layer. The reaction of LLZO in humid air also involves the protonation of LLZO. To examine the impacts of proton on the transport properties of LLZO, the Li^+ and H^+ ion diffusivity and conductivity was calculated using AIMD. The Li ionic conductivity is comparable to pristine LLZO for minor levels of contamination (~9 %), while Li-ion conductivities are significantly decreased at high levels of proton contamination (~63 %).

Elastic properties were examined to assess the effectiveness of LLZO in suppressing dendrite formation at the Li-LLZO interface. Based on the model of Monroe and Newman, LLZO is predicted to be stiff enough to suppress lithium dendrite formation. For example, linear elasticity models suggest that a solid electrolyte having a shear modulus greater than approximately 8.5 GPa can suppress dendrite formation on a Li anode. The present calculations yield averaged shear moduli for Al and Ta-doped LLZO of 58-60 GPa, far exceeding the targeted value. Nevertheless, it is important to recognize that scenarios exist in which dendrites could still form even in the presence of a solid electrolyte that satisfies Monroe's criterion (eg., microstructural features such as porosity at the interface or poor interfacial wetting). Thus, the Monroe-Newman criterion should be considered as a necessary but insufficient condition for achieving dendrite resistance: contributions from microstructure should also be considered.

Current focusing caused by fast Li-ion migration along GBs is explored as a possible scenario resulting in dendrite formation. In the presence of fast GB transport, Li plating would occur preferentially in regions where GBs intersect the electrode surface. Assuming the arrival rate of Li at these intersections is faster than its lateral migration away, then the resulting 'pile-up' of Li could nucleate dendrites. This 'fast GB diffusion' hypothesis is studied by calculating the rate of Li-ion migration along three low-energy tilt GBs (Σ3 & Σ5) of LLZO. Our MD results reveal that Li-ion diffusion is comparable in all 3 tilt GBs at high temperatures (> 900 K), and only slightly slower than bulk diffusion. In contrast, room temperature diffusion differs significantly between the Σ3 and Σ5 systems: diffusion in the more compact Σ3 boundary remains relatively fast (~50% of the bulk rate), while transport in the Σ5 boundaries is roughly two orders of magnitude slower than the bulk. Diffusion within the Σ5 boundaries is isotropic, while anisotropic transport is observed in the Σ3 system at lower temperatures (< 700 K). In the

latter system, intra-plane diffusion at 300 K is up to 4 times faster than the bulk, while transboundary diffusion is ~200 times slower. Generally, Li transport is reduced in the GB region. Thus, current focusing along GBs due to faster GB Li-ion transport does not appear to explain Li dendrite penetration.

Additionally, we hypothesize that softening of the LLZO in the vicinity of GBs can provide a mechanism for dendrite penetration. These effects could arise from deviations in density and atomic structure near the GB plane. MD calculations are performed to examine the softening using two, low-energy Σ5 tilt and twist GBs. The elastic constants associated with uniaxial strain perpendicular to the GB plane and with shear parallel to the GB were calculated at 300 K. These calculations indicate a severe softening in the immediate vicinity of the GB: elastic constants are observed to be up to 50% smaller at GBs than in the bulk. We propose that nanoscale softening attributed to microstructural features such as GBs may explain why these features are susceptible to metal penetration during electrodeposition.

8.2 Next steps

Although the low energies of the GBs studied in the latter chapters of this dissertation suggest that they will be present in annealed samples, lower-temperature synthesis routes could generate higher-energy GBs with less-compact structures. Such GBs are expected to have a larger impact on Li-ion conductivity and elastic properties. More systematic study of the impact of GB mis-orientation on transport and mechanical properties should be considered in future studies.

The present atomistic models have also emphasized GB properties in pristine LLZO, and the impact of adventitious impurities and intentional additives (e.g., dopants such as Al and Ta,

or sintering aides) on GB phenomena have not been considered. Consequently, computational studies that quantify the impact of segregation and second phase formation at GBs in LLZO would be also a helpful next step.

In addition, the different atomic structure of the GB could result in a distinct bonding environment. First-principles calculations can be performed regarding the electronic structure at GBs with a detailed bonding analysis.

Finally, evaluating the mechanical properties in the vicinity of GBs would also be a valuable follow-on study. For example, the ideal shear strength can be calculated to determine the resistance of GB to plastic deformation. Fracture toughness is another mechanical property that can be estimated computationally to explain Li penetration along GBs.

Bibliography

(1) Armand, M.; Tarascon, J.-M. Building Better Batteries. *Nature* **2008**, *451*, 652.

(2) Bruce, P. G.; Freunberger, S. A.; Hardwick, L. J.; Tarascon, J.-M. Li–O_2 and Li–S Batteries with High Energy Storage. *Nat. Mater.* **2012**, *11* (1), 19–29.

(3) Dunn, B.; Dunn, B.; Kamath, H.; Tarascon, J. Electrical Energy Storage for the Gridfor the Grid : A Battery of Choices. *Sci. Mag.* **2011**, *334* (6058), 928–936.

(4) Larcher, D.; Tarascon, J. M. Towards Greener and More Sustainable Batteries for Electrical Energy Storage. *Nat. Chem.* **2015**, *7* (1), 19–29.

(5) Tarascon, J.-M.; Armand, M. Issues and Challenges Facing Rechargeable Lithium Batteries. In *Materials for Sustainable Energy*; Co-Published with Macmillan Publishers Ltd, UK, 2010; pp 171–179.

(6) Yang, C.; Fu, K.; Zhang, Y.; Hitz, E.; Hu, L. Protected Lithium-Metal Anodes in Batteries: From Liquid to Solid. *Adv. Mater.* **2017**, *29* (36), 1–28.

(7) Li, J.; Ma, C.; Chi, M.; Liang, C.; Dudney, N. J. Solid Electrolyte: The Key for High-Voltage Lithium Batteries. *Adv. Energy Mater.* **2015**, *5* (4), 1–6.

(8) Liu, Y.; He, P.; Zhou, H. Rechargeable Solid-State Li–Air and Li–S Batteries: Materials, Construction, and Challenges. *Adv. Energy Mater.* **2018**, *8* (4), 1–22.

(9) Suo, L.; Hu, Y. S.; Li, H.; Armand, M.; Chen, L. A New Class of Solvent-in-Salt Electrolyte for High-Energy Rechargeable Metallic Lithium Batteries. *Nat. Commun.* **2013**, *4*, 1–9.

(10) Lee, J. S.; Kim, S. T.; Cao, R.; Choi, N. S.; Liu, M.; Lee, K. T.; Cho, J. Metal-Air Batteries with High Energy Density: Li-Air versus Zn-Air. *Adv. Energy Mater.* **2011**, *1* (1), 34–50.

(11) Lin, D.; Liu, Y.; Cui, Y. Reviving the Lithium Metal Anode for High-Energy Batteries. *Nat. Nanotechnol.* **2017**, *12* (3), 194–206.

(12) Fu, K.; Gong, Y.; Hitz, G. T.; McOwen, D. W.; Li, Y.; Xu, S.; Wen, Y.; Zhang, L.; Wang, C.; Pastel, G.; et al. Three-Dimensional Bilayer Garnet Solid Electrolyte Based High Energy Density Lithium Metal-Sulfur Batteries. *Energy Environ. Sci.* **2017**, *10* (7), 1568–1575.

(13) Roth, E. P.; Orendorff, C. J. How Electrolytes Influence Battery Safety. *Interface Mag.* **2012**, *21* (2), 45–49.

(14) Goodenough, J. B.; Kim, Y. Challenges for Rechargeable Li Batteries. *Chem. Mater.* **2010**, *22* (3), 587–603.

(15) Monroe, C.; Newman, J. The Impact of Elastic Deformation on Deposition Kinetics at

Lithium/Polymer Interfaces. *J. Electrochem. Soc.* **2005**, *152* (2), A396.

(16) Aurbach, D.; Markovsky, B.; Salitra, G.; Markevich, E.; Talyossef, Y.; Koltypin, M.; Nazar, L.; Ellis, B.; Kovacheva, D. Review on Electrode-Electrolyte Solution Interactions, Related to Cathode Materials for Li-Ion Batteries. *J. Power Sources* **2007**, *165* (2), 491–499.

(17) Amine, K.; Tukamoto, H.; Yasuda, H.; Fujita, Y. Preparation and Electrochemical Investigation of $LiMn_{2-x}Me_xO_4$ (Me: Ni, Fe, and x = 0.5, 1) Cathode Materials for Secondary Lithium Batteries. *J. Power Sources* **1997**, *68* (2), 604–608.

(18) Manthiram, A.; Chemelewski, K.; Lee, E.-S. A Perspective on the High-Voltage $LiMn_{1.5}Ni_{0.5}O_4$ Spinel Cathode for Lithium-Ion Batteries. *Energy Environ. Sci.* **2014**, *7* (4), 1339.

(19) Manthiram, A.; Yu, X.; Wang, S. Lithium Battery Chemistries Enabled by Solid-State Electrolytes. *Nat. Rev. Mater.* **2017**, *2* (4), 1–16.

(20) Bachman, J. C.; Muy, S.; Grimaud, A.; Chang, H. H.; Pour, N.; Lux, S. F.; Paschos, O.; Maglia, F.; Lupart, S.; Lamp, P.; et al. Inorganic Solid-State Electrolytes for Lithium Batteries: Mechanisms and Properties Governing Ion Conduction. *Chem. Rev.* **2016**, *116* (1), 140–162.

(21) Kanno, R.; Hata, T.; Kawamoto, Y.; Irie, M. Synthesis of a New Lithium Ionic Conductor, Thio-LISICON-Lithium Germanium Sulfide System. *Solid State Ionics* **2000**, *130* (1), 97–104.

(22) Kamaya, N.; Homma, K.; Yamakawa, Y.; Hirayama, M.; Kanno, R.; Yonemura, M.; Kamiyama, T.; Kato, Y.; Hama, S.; Kawamoto, K.; et al. A Lithium Superionic Conductor. *Nat. Mater.* **2011**, *10* (9), 682–686.

(23) Muramatsu, H.; Hayashi, A.; Ohtomo, T.; Hama, S.; Tatsumisago, M. Structural Change of Li_2S–P_2S_5 Sulfide Solid Electrolytes in the Atmosphere. *Solid State Ionics* **2011**, *182* (1), 116–119.

(24) Arbi, K.; Mandal, S.; Rojo, J. M.; Sanz, J. Dependence of Ionic Conductivity on Composition of Fast Ionic Conductors $Li_{1+x}Ti_{2-x}Al_x(PO_4)_3$, $0 \leq x \leq 0.7$. A Parallel NMR and Electric Impedance Study. *Chem. Mater.* **2002**, *14* (3), 1091–1097.

(25) Yao, X.; Huang, B.; Yin, J.; Peng, G.; Huang, Z.; Gao, C.; Liu, D.; Xu, X. All-Solid-State Lithium Batteries with Inorganic Solid Electrolytes: Review of Fundamental Science. *Chinese Phys. B* **2015**, *25* (1).

(26) Hartmann, P.; Leichtweiss, T.; Busche, M. R.; Schneider, M.; Reich, M.; Sann, J.; Adelhelm, P.; Janek, J. Degradation of NASICON-Type Materials in Contact with Lithium Metal: Formation of Mixed Conducting Interphases (MCI) on Solid Electrolytes. *J. Phys. Chem. C* **2013**, *117* (41), 21064–21074.

(27) Bohnke, O. The Fast Lithium-Ion Conducting Oxides $Li_{3x}La_{2/3-x}TiO_3$ from Fundamentals to Application. *Solid State Ionics* **2008**, *179* (1–6), 9–15.

(28) Murugan, R.; Thangadurai, V.; Weppner, W. Fast Lithium Ion Conduction in Garnet-Type $Li_7La_3Zr_2O_{12}$. *Angew. Chemie - Int. Ed.* **2007**, *46* (41), 7778–7781.

(29) Geiger, C. A.; Alekseev, E.; Lazic, B.; Fisch, M.; Armbruster, T.; Langner, R.; Fechtelkord, M.; Kim, N.; Pettke, T.; Weppner, W. Crystal Chemistry and Stability of "$Li_7La_3Zr_2O_{12}$" Garnet: A Fast Lithium-Ion Conductor. *Inorg. Chem.* **2011**, *50* (3), 1089–1097.

(30) Rangasamy, E.; Wolfenstine, J.; Sakamoto, J. The Role of Al and Li Concentration on the Formation of Cubic Garnet Solid Electrolyte of Nominal Composition $Li_7La_3Zr_2O_{12}$. *Solid State Ionics* **2012**, *206*, 28–32.

(31) Thompson, T.; Sharafi, A.; Johannes, M. D.; Huq, A.; Allen, J. L.; Wolfenstine, J.; Sakamoto, J. A Tale of Two Sites: On Defining the Carrier Concentration in Garnet-Based Ionic Conductors for Advanced Li Batteries. *Adv. Energy Mater.* **2015**, *5* (11), 1–9.

(32) Thompson, T.; Wolfenstine, J.; Allen, J. L.; Johannes, M.; Huq, A.; David, I. N.; Sakamoto, J. Tetragonal vs. Cubic Phase Stability in Al-Free Ta Doped $Li_7La_3Zr_2O_{12}$ (LLZO). *J. Mater. Chem. A* **2014**, *2* (33), 13431–13436.

(33) Allen, J. L.; Wolfenstine, J.; Rangasamy, E.; Sakamoto, J. Effect of Substitution (Ta, Al, Ga) on the Conductivity of $Li_7La_3Zr_2O_{12}$. *J. Power Sources* **2012**, *206*, 315–319.

(34) Thangadurai, V.; Kaack, H.; Weppner, W. J. F. Novel Fast Lithium Ion Conduction in Garnet-Type $Li_5La_3M_2O_{12}$ (M = Nb, Ta). *J. Am. Ceram. Soc.* **2003**, *86* (3), 437–440.

(35) Cussen, E. J. Structure and Ionic Conductivity in Lithium Garnets. *J. Mater. Chem.* **2010**, *20* (25), 5167–5173.

(36) Xie, H.; Alonso, J. A.; Li, Y.; Fernández-Díaz, M. T.; Goodenough, J. B. Lithium Distribution in Aluminum-Free Cubic $Li_7La_3Zr_2O_{12}$. *Chem. Mater.* **2011**, *23* (16), 3587–3589.

(37) O'Callaghan, M. P.; Lynham, D. R.; Cussen, E. J.; Chen, G. Z. Structure and Ionic-Transport Properties of Lithium-Containing Garnets $Li_3Ln_3Te_2O_{12}$ (Ln = Y, Pr, Nd, Sm−Lu). *Chem. Mater.* **2006**, *18* (19), 4681–4689.

(38) Thangadurai, V.; Weppner, W. $Li_6ALa_2Ta_2O_{12}$ (A=Sr, Ba): Novel Garnet-like Oxides for Fast Lithium Ion Conduction. *Adv. Funct. Mater.* **2005**, *15* (1), 107–112.

(39) Koch, B.; Vogel, M. Lithium Ionic Jump Motion in the Fast Solid Ion Conductor $Li_5La_3Nb_2O_{12}$. *Solid State Nucl. Magn. Reson.* **2008**, *34* (1–2), 37–43.

(40) Roof, I. P.; Smith, M. D.; Cussen, E. J.; zur Loye, H. C. Crystal Growth of a Series of Lithium Garnets $Ln_3Li_5Ta_2O_{12}$ (Ln=La, Pr, Nd): Structural Properties, Alexandrite Effect and Unusual Ionic Conductivity. *J. Solid State Chem.* **2009**, *182* (2), 295–300.

(41) Bernstein, N.; Johannes, M. D.; Hoang, K. Origin of the Structural Phase Transition in $Li_7La_3Zr_2O_{12}$. *Phys. Rev. Lett.* **2012**, *109* (20), 1–5.

(42) Awaka, J.; Kijima, N.; Hayakawa, H.; Akimoto, J. Synthesis and Structure Analysis of Tetragonal $Li_7La_3Zr_2O_{12}$ with the Garnet-Related Type Structure. *J. Solid State Chem.* **2009**, *182* (8), 2046–2052.

(43) Logéat, A.; Köhler, T.; Eisele, U.; Stiaszny, B.; Harzer, A.; Tovar, M.; Senyshyn, A.; Ehrenberg, H.; Kozinsky, B. From Order to Disorder: The Structure of Lithium-Conducting Garnets $Li_{7-x}La_3Ta_xZr_{2-x}O_{12}$ (x = 0-2). *Solid State Ionics* **2012**, *206*, 33–38.

(44) Wu, J. F.; Chen, E. Y.; Yu, Y.; Liu, L.; Wu, Y.; Pang, W. K.; Peterson, V. K.; Guo, X. Gallium-Doped $Li_7La_3Zr_2O_{12}$ Garnet-Type Electrolytes with High Lithium-Ion Conductivity. *ACS Appl. Mater. Interfaces* **2017**, *9* (2), 1542–1552.

(45) Xu, Y.-N.; Ching, W. Y. Electronic Structure of Yttrium Aluminum Garnet $Y_3Al_5O_{12}$. *Phys. Rev. B* **1999**, *59* (16), 10530–10535.

(46) Larraz, G.; Orera, A.; Sanjuán, M. L. Cubic Phases of Garnet-Type $Li_7La_3Zr_2O_{12}$: The Role of Hydration. *J. Mater. Chem. A* **2013**, *1* (37), 11419–11428.

(47) Cheng, L.; Wu, C. H.; Jarry, A.; Chen, W.; Ye, Y.; Zhu, J.; Kostecki, R.; Persson, K.; Guo, J.; Salmeron, M.; et al. Interrelationships among Grain Size, Surface Composition, Air Stability, and Interfacial Resistance of Al-Substituted $Li_7La_3Zr_2O_{12}$ Solid Electrolytes. *ACS Appl. Mater. Interfaces* **2015**, *7* (32), 17649–17655.

(48) Sharafi, A.; Meyer, H. M.; Nanda, J.; Wolfenstine, J.; Sakamoto, J. Characterizing the Li-$Li_7La_3Zr_2O_{12}$ Nterface Stability and Kinetics as a Function of Temperature and Current Density. *J. Power Sources* **2016**, *302*, 135–139.

(49) Cheng, L.; Chen, W.; Kunz, M.; Persson, K.; Tamura, N.; Chen, G.; Doeff, M. Effect of Surface Microstructure on Electrochemical Performance of Garnet Solid Electrolytes. *ACS Appl. Mater. Interfaces* **2015**, *7* (3), 2073–2081.

(50) Han, X.; Gong, Y.; Fu, K.; He, X.; Hitz, G. T.; Dai, J.; Pearse, A.; Liu, B.; Wang, H.; Rubloff, G.; et al. Negating Interfacial Impedance in Garnet-Based Solid-State Li Metal Batteries. *Nat. Mater.* **2017**, *16* (5), 572–579.

(51) Fu, K. K.; Gong, Y.; Liu, B.; Zhu, Y.; Xu, S.; Yao, Y.; Luo, W.; Wang, C.; Lacey, S. D.; Dai, J.; et al. Toward Garnet Electrolyte–Based Li Metal Batteries: An Ultrathin, Highly Effective, Artificial Solid-State Electrolyte/Metallic Li Interface. *Sci. Adv.* **2017**, *3* (4), 1–12.

(52) Tsai, C. L.; Roddatis, V.; Chandran, C. V.; Ma, Q.; Uhlenbruck, S.; Bram, M.; Heitjans, P.; Guillon, O. $Li_7La_3Zr_2O_{12}$ Interface Modification for Li Dendrite Prevention. *ACS Appl. Mater. Interfaces* **2016**, *8* (16), 10617–10626.

(53) Monroe, C.; Newman, J. Dendrite Growth in Lithium/Polymer Systems. *J. Electrochem. Soc.* **2003**, *150* (10), A1377.

(54) Cheng, E. J.; Sharafi, A.; Sakamoto, J. Intergranular Li Metal Propagation through Polycrystalline $Li_{6.25}Al_{0.25}La_3Zr_2O_{12}$ Ceramic Electrolyte. *Electrochim. Acta* **2017**, *223*, 85–91.

(55) Tenhaeff, W. E.; Rangasamy, E.; Wang, Y.; Sokolov, A. P.; Wolfenstine, J.; Sakamoto, J.; Dudney, N. J. Resolving the Grain Boundary and Lattice Impedance of Hot-Pressed $Li_7La_3Zr_2O_{12}$ Garnet Electrolytes. *ChemElectroChem* **2014**, *1* (2), 375–378.

(56) David, I. N.; Thompson, T.; Wolfenstine, J.; Allen, J. L.; Sakamoto, J. Microstructure and Li-Ion Conductivity of Hot-Pressed Cubic $Li_7La_3Zr_2O_{12}$. *J. Am. Ceram. Soc.* **2015**, *98* (4), 1209–1214.

(57) Ohta, S.; Seki, J.; Yagi, Y.; Kihira, Y.; Tani, T.; Asaoka, T. Co-Sinterable Lithium Garnet-Type Oxide Electrolyte with Cathode for All-Solid-State Lithium Ion Battery. *J. Power Sources* **2014**, *265*, 40–44.

(58) Li, Y.; Wang, Z.; Li, C.; Cao, Y.; Guo, X. Densification and Ionic-Conduction Improvement of Lithium Garnet Solid Electrolytes by Flowing Oxygen Sintering. *J. Power Sources* **2014**, *248*, 642–646.

(59) El Shinawi, H.; Janek, J. Stabilization of Cubic Lithium-Stuffed Garnets of the Type "$Li_7La_3Zr_2O_{12}$" by Addition of Gallium. *J. Power Sources* **2013**, *225*, 13–19.

(60) Yu, S.; Schmidt, R. D.; Garcia-Mendez, R.; Herbert, E.; Dudney, N. J.; Wolfenstine, J. B.; Sakamoto, J.; Siegel, D. J. Elastic Properties of the Solid Electrolyte $Li_7La_3Zr_2O_{12}$ (LLZO). *Chem. Mater.* **2016**, *28* (1), 197–206.

(61) Thompson, T.; Yu, S.; Williams, L.; Schmidt, R. D.; Garcia-Mendez, R.; Wolfenstine, J.; Allen, J. L.; Kioupakis, E.; Siegel, D. J.; Sakamoto, J. Electrochemical Window of the Li-Ion Solid Electrolyte $Li_7La_3Zr_2O_{12}$. *ACS Energy Lett.* **2017**, *2* (2), 462–468.

(62) Sharafi, A.; Yu, S.; Naguib, M.; Lee, M.; Ma, C.; Meyer, H. M.; Nanda, J.; Chi, M.; Siegel, D. J.; Sakamoto, J. Impact of Air Exposure and Surface Chemistry on Li–$Li_7La_3Zr_2O_{12}$ Interfacial Resistance. *J. Mater. Chem. A* **2017**, *5* (26), 13475–13487.

(63) Sharafi, A.; Kazyak, E.; Davis, A. L.; Yu, S.; Thompson, T.; Siegel, D. J.; Dasgupta, N. P.; Sakamoto, J. Surface Chemistry Mechanism of Ultra-Low Interfacial Resistance in the Solid-State Electrolyte $Li_7La_3Zr_2O_{12}$. *Chem. Mater.* **2017**, *29* (18), 7961–7968.

(64) Yu, S.; Siegel, D. J. Grain Boundary Contributions to Li-Ion Transport in the Solid Electrolyte $Li_7La_3Zr_2O_{12}$ (LLZO). *Chem. Mater.* **2017**, *29* (22), 9639–9647.

(65) Hohenberg, P.; Kohn, W. Inhomogeneous Electron Gas. *Phys. Rev.* **1964**, *136* (3B), B864–B871.

(66) Kohn, W.; Sham, L. J. Self-Consistent Equations Including Exchange and Correlation Effects. *Phys. Rev.* **1965**, *140* (4A), A1133–A1138.

(67) Jones, R. O.; Gunnarsson, O. The Density Functional Formalism, Its Applications and Prospects. *Rev. Mod. Phys.* **1989**, *61* (3), 689–746.

(68) Perdew, J. P.; Zunger, A. Self-Interaction Correction to Density-Functional Approximations for Many-Electron Systems. *Phys. Rev. B* **1981**, *23* (10), 5048–5079.

(69) Ceperley, D. M.; Alder, B. J. Ground State of the Electron Gas by a Stochastic Method. *Phys. Rev. Lett.* **1980**, *45* (7), 566–569.

(70) Perdew, J. P.; Burke, K. Comparison Shopping for a Gradient-Corrected Density Functional. *Int. J. Quantum Chem.* **1996**, *57* (3), 309–319.

(71) Perdew, J. P.; Burke, K.; Ernzerhof, M. Generalized Gradient Approximation Made Simple. *Phys. Rev. Lett.* **1996**, *77* (18), 3865–3868.

(72) Hedin, L. New Method for Calculating the One-Particle Green's Function with Application to the Electron-Gas Problem. *Phys. Rev.* **1965**, *139* (3A), A796--A823.

(73) Gunnarsson, F. A. and O. The GW Method. *Reports Prog. Phys.* **1998**, *61* (3), 237.

(74) Kresse, G.; Furthmüller, J. Efficient Iterative Schemes for Ab Initio Total-Energy Calculations Using a Plane-Wave Basis Set. *Phys. Rev. B - Condens. Matter Mater. Phys.* **1996**, *54* (16), 11169–11186.

(75) Blöchl, P. E. Projector Augmented-Wave Method. *Phys. Rev. B* **1994**, *50* (24), 17953–17979.

(76) Kresse, G.; Joubert, D. From Ultrasoft Pseudopotentials to the Projector Augmented-Wave Method. *Phys. Rev. B* **1999**, *59* (3), 1758–1775.

(77) Heyd, J.; Scuseria, G. E.; Ernzerhof, M. Hybrid Functionals Based on a Screened Coulomb Potential. *J. Chem. Phys.* **2003**, *118* (18), 8207–8215.

(78) Krukau, A. V.; Vydrov, O. A.; Izmaylov, A. F.; Scuseria, G. E. Influence of the Exchange Screening Parameter on the Performance of Screened Hybrid Functionals. *J. Chem. Phys.* **2006**, *125* (22).

(79) Shishkin, M.; Kresse, G. Implementation and Performance of the Frequency-Dependent GW Method within the PAW Framework. *Phys. Rev. B - Condens. Matter Mater. Phys.* **2006**, *74* (3), 1–13.

(80) Fuchs, F.; Furthmüller, J.; Bechstedt, F.; Shishkin, M.; Kresse, G. Quasiparticle Band Structure Based on a Generalized Kohn-Sham Scheme. *Phys. Rev. B - Condens. Matter Mater. Phys.* **2007**, *76* (11), 1–8.

(81) Pack, J. D.; Monkhorst, H. J. "special Points for Brillouin-Zone Integrations"-a Reply. *Phys. Rev. B* **1977**, *16* (4), 1748–1749.

(82) Lee, J. G. *Computational Materials Science: An Introduction*; Crc Press, 2016.

(83) Adams, S.; Rao, R. P. High Power Lithium Ion Battery Materials by Computational Design. *Phys. Status Solidi* **2011**, *208* (8), 1746–1753.

(84) Chen, H.; Adams, S. Bond Softness Sensitive Bond-Valence Parameters for Crystal Structure Plausibility Tests. *IUCrJ* **2017**, *4*, 614–625.

(85) Adams, S.; Rao, R. P. Ion Transport and Phase Transition in $Li_{7-x}La_3(Zr_{2-x}M_x)O_{12}$ (M = Ta^{5+}, Nb^{5+}, x = 0, 0.25). *J. Mater. Chem.* **2012**, *22* (4), 1426–1434.

(86) Plimpton, S. Fast Parallel Algorithms for Short-Range Molecular Dynamics. *Journal of Computational Physics*. 1995, pp 1–19.

(87) Xu, K. Electrolytes and Interphases in Li-Ion Batteries and Beyond. *Chem. Rev.* **2014**, *114* (23), 11503–11618.

(88) Cheng, L.; Assary, R. S.; Qu, X.; Jain, A.; Ong, S. P.; Rajput, N. N.; Persson, K.; Curtiss, L. A. Accelerating Electrolyte Discovery for Energy Storage with High-Throughput Screening. *J. Phys. Chem. Lett.* **2015**, *6* (2), 283–291.

(89) Kumar, N.; Siegel, D. J. Interface-Induced Renormalization of Electrolyte Energy Levels in Magnesium Batteries. *J. Phys. Chem. Lett.* **2016**, *7* (5), 874–881.

(90) Zhu, Y.; He, X.; Mo, Y. Origin of Outstanding Stability in the Lithium Solid Electrolyte Materials: Insights from Thermodynamic Analyses Based on First-Principles Calculations. *ACS Appl. Mater. Interfaces* **2015**, *7* (42), 23685–23693.

(91) Murnaghan, F. D. The Compressibility of Media under Extreme Pressures. *Proc. Natl. Acad. Sci.* **1944**, *30* (9), 244 LP-247.

(92) Toroker, M. C.; Kanan, D. K.; Alidoust, N.; Isseroff, L. Y.; Liao, P.; Carter, E. A. First

Principles Scheme to Evaluate Band Edge Positions in Potential Transition Metal Oxide Photocatalysts and Photoelectrodes. *Phys. Chem. Chem. Phys.* **2011**, *13* (37), 16644–16654.

(93) Miara, L. J.; Ong, S. P.; Mo, Y.; Richards, W. D.; Park, Y.; Lee, J.-M.; Lee, H. S.; Ceder, G. Effect of Rb and Ta Doping on the Ionic Conductivity and Stability of the Garnet $Li_{7+2x-y}(La_{3-x}Rb_x)(Zr_{2-y}Ta_y)O_{12}$ ($0 \leq x \leq 0.375$, $0 \leq y \leq 1$) Superionic Conductor: A First Principles Investig. *Chem. Mater.* **2013**, *25* (15), 3048–3055.

(94) Han, F.; Zhu, Y.; He, X.; Mo, Y.; Wang, C. Electrochemical Stability of $Li_{10}GeP_2S_{12}$ and $Li_7La_3Zr_2O_{12}$ Solid Electrolytes. *Adv. Energy Mater.* **2016**, *6* (8).

(95) Tran, F.; Blaha, P. Accurate Band Gaps of Semiconductors and Insulators with a Semilocal Exchange-Correlation Potential. *Phys. Rev. Lett.* **2009**, *102* (22), 5–8.

(96) Luntz, A. C.; Voss, J.; Reuter, K. Interfacial Challenges in Solid-State Li Ion Batteries. *J. Phys. Chem. Lett.* **2015**, *6* (22), 4599–4604.

(97) Cheng, M.; Rangasamy, E.; Liang, C.; Sakamoto, J.; More, K. L.; Chi, M. Excellent Stability of a Lithium-Ion-Conducting Solid Electrolyte upon Reversible Li^+/H^+ Exchange in Aqueous Solutions. *Angew. Chemie - Int. Ed.* **2015**, *54* (1), 129–133.

(98) Yow, Z. F.; Oh, Y. L.; Gu, W.; Rao, R. P.; Adams, S. Effect of Li^+/H^+ Exchange in Water Treated Ta-Doped $Li_7La_3Zr_2O_{12}$. *Solid State Ionics* **2016**, *292*, 122–129.

(99) Larraz, G.; Orera, A.; Sanz, J.; Sobrados, I.; Diez-Gómez, V.; Sanjuán, M. L. NMR Study of Li Distribution in $Li_{7-x}H_xLa_3Zr_2O_{12}$ Garnets. *J. Mater. Chem. A* **2015**, *3* (10), 5683–5691.

(100) Wilhoit, R. C.; Chao, J.; Hall, K. R. Thermodynamic Properties of Key Organic Oxygen Compounds in the Carbon Range C1 to C4. Part 1. Properties of Condensed Phases. *J. Phys. Chem. Ref. Data* **1985**, *14* (1), 1–175.

(101) Lee, K.; Murray, É. D.; Kong, L.; Lundqvist, B. I.; Langreth, D. C. Higher-Accuracy van Der Waals Density Functional. *Phys. Rev. B* **2010**, *82* (8), 81101.

(102) Smith, J. R.; Hong, T.; Srolovitz, D. J. Metal-Ceramic Adhesion and the Harris Functional. *Phys. Rev. Lett.* **1994**, *72* (25), 4021–4024.

(103) Boulant, A.; Bardeau, J. F.; Jouanneaux, A.; Emery, J.; Buzare, J.-Y.; Bohnke, O. Reaction Mechanisms of $Li_{0.30}La_{0.57}TiO_3$ Powder with Ambient Air: H^+/Li^+ Exchange with Water and Li_2CO_3 Formation. *Dalt. Trans.* **2010**, *39* (16), 3968–3975.

(104) Sakanoi, R.; Shimazaki, T.; Xu, J.; Higuchi, Y.; Ozawa, N.; Sato, K.; Hashida, T.; Kubo, M. Communication: Different Behavior of Young's Modulus and Fracture Strength of CeO_2: Density Functional Theory Calculations. *J. Chem. Phys.* **2014**, *140* (12).

(105) Ni, J. E.; Case, E. D.; Sakamoto, J. S.; Rangasamy, E.; Wolfenstine, J. B. Room Temperature Elastic Moduli and Vickers Hardness of Hot-Pressed LLZO Cubic Garnet. *J. Mater. Sci.* **2012**, *47* (23), 7978–7985.

(106) Li, Y.; Han, J. T.; Wang, C. A.; Vogel, S. C.; Xie, H.; Xu, M.; Goodenough, J. B. Ionic Distribution and Conductivity in Lithium Garnet $Li_7La_3Zr_2O_{12}$. *J. Power Sources* **2012**, *209*, 278–281.

(107) Rettenwander, D.; Blaha, P.; Laskowski, R.; Schwarz, K.; Bottke, P.; Wilkening, M.; Geiger, C. A.; Amthauer, G. DFT Study of the Role of Al^{3+} in the Fast Ion-Conductor $Li_{7-3x}Al^{3+}_xLa_3Zr_2O_{12}$ Garnet. *Chem. Mater.* **2014**, *26* (8), 2617–2623.

(108) Mehl, M. J.; Osburn, J. E.; Papaconstantopoulos, D. A.; Klein, B. M. Intermetallic Structural Properties. *Phys. Rev. B* **1990**, *41* (15), 311–323.

(109) Ranganathan, S. I.; Ostoja-Starzewski, M. Universal Elastic Anisotropy Index. *Phys. Rev. Lett.* **2008**, *101* (5), 3–6.

(110) Chung, D.-H.; Swica, J. J.; Crandall, W. B. Relation of Single-Crystal Elastic Constants to Polycrystalline Isotropic Elastic Moduli of MgO. *J. Am. Ceram. Soc.* **1963**, *46* (9), 452–457.

(111) Wachtman, J. B.; Tefft, W. E.; Lam, D. G.; Apstein, C. S. Exponential Temperature Dependence of Young's Modulus for Several Oxides. *Phys. Rev.* **1961**, *122* (6), 1754–1759.

(112) Dovesi, R.; Roetti, C.; Freyria-Fava, C.; Prencipe, M.; Saunders, V. R. On the Elastic Properties of Lithium, Sodium and Potassium Oxide. An Ab Initio Study. *Chem. Phys.* **1991**, *156* (1), 11–19.

(113) Pugh, S. F. XCII. Relations between the Elastic Moduli and the Plastic Properties of Polycrystalline Pure Metals. *London, Edinburgh, Dublin Philos. Mag. J. Sci.* **1954**, *45* (367), 823–843.

(114) Niu, H.; Chen, X. Q.; Liu, P.; Xing, W.; Cheng, X.; Li, D.; Li, Y. Extra-Electron Induced Covalent Strengthening and Generalization of Intrinsic Ductile-to-Brittle Criterion. *Sci. Rep.* **2012**, *2*, 1–6.

(115) Wolfenstine, J.; Jo, H.; Cho, Y. H.; David, I. N.; Askeland, P.; Case, E. D.; Kim, H.; Choe, H.; Sakamoto, J. A Preliminary Investigation of Fracture Toughness of $Li_7La_3Zr_2O_{12}$ and Its Comparison to Other Solid Li-Ionconductors. *Mater. Lett.* **2013**, *96*, 117–120.

(116) Rice, R. W. Possible Effects of Elastic Anisotropy on Mechanical Properties of Ceramics. *J. Mater. Sci. Lett.* **1994**, *13* (17), 1261–1266.

(117) C. Nash, H.; Smith, C. S. Single-Crystal Elastic Constants of Lithium. *J. Phys. Chem. Solids* **1959**, *9* (2), 113–118.

(118) Slotwinski, T.; Trivisonno, J. Temperature Dependence of the Elastic Constants of Single Crystal Lithium. *J. Phys. Chem. Solids* **1969**, *30* (5), 1276–1278.

(119) Day, J. P.; Ruoff, A. L. The Variation of the Elastic Constants of Lithium with Temperature and Pressure. *Phys. status solidi* **1974**, *25* (1), 205–213.

(120) Felice, R. A.; Trivisonno, J.; Schuele, D. E. Temperature and Pressure Dependence of the Single-Crystal Elastic Constants of Li and Natural Lithium. *Phys. Rev. B* **1977**, *16* (12), 5173–5184.

(121) Robertson, W. M.; Montgomery, D. J. Elastic Modulus of Isotopically-Concentrated Lithium. *Phys. Rev.* **1960**, *117* (2), 440–442.

(122) Bridgman, P. W. The Effect of Tension on the Electrical Resistance of Certain Abnormal

Metals. *Proc. Am. Acad. Arts Sci.* **1922**, *57* (3), 41–66.

(123) Chaim, R.; Hefetz, M. Effect of Grain Size on Elastic Modulus and Hardness of Nanocrystalline ZrO_2 -3 Wt % Y_3O_3 Ceramic. *J. Mater. Sci.* **2004**, *39* (9), 3057–3061.

(124) Jackman, S. D.; Cutler, R. A. Effect of Microcracking on Ionic Conductivity in LATP. *J. Power Sources* **2012**, *218*, 65–72.

(125) Cho, Y. H.; Wolfenstine, J.; Rangasamy, E.; Kim, H.; Choe, H.; Sakamoto, J. Mechanical Properties of the Solid Li-Ion Conducting Electrolyte: $Li_{0.33}La_{0.57}TiO_3$. *J. Mater. Sci.* **2012**, *47* (16), 5970–5977.

(126) Herbert, E. G.; Tenhaeff, W. E.; Dudney, N. J.; Pharr, G. M. Mechanical Characterization of LiPON Films Using Nanoindentation. *Thin Solid Films* **2011**, *520* (1), 413–418.

(127) Suzuki, Y.; Kami, K.; Watanabe, K.; Watanabe, A.; Saito, N.; Ohnishi, T.; Takada, K.; Sudo, R.; Imanishi, N. Transparent Cubic Garnet-Type Solid Electrolyte of Al_2O_3-Doped $Li_7La_3Zr_2O_{12}$. *Solid State Ionics* **2015**, *278*, 172–176.

(128) Ren, Y.; Shen, Y.; Lin, Y.; Nan, C. W. Direct Observation of Lithium Dendrites inside Garnet-Type Lithium-Ion Solid Electrolyte. *Electrochem. commun.* **2015**, *57*, 27–30.

(129) Nakagawa, T.; Nakamura, A.; Sakaguchi, I.; Shibata, N.; Lagerlof, K. P. D.; Yamamoto, T.; Haneda, H.; Ikuhara, Y. Oxygen Pipe Diffusion in Sapphire Basal Dislocation. *J. Ceram. Soc. Japan* **2006**, *114* (1335), 1013–1017.

(130) McKenna, K.; Shluger, A. The Interaction of Oxygen Vacancies with Grain Boundaries in Monoclinic HfO_2. *Appl. Phys. Lett.* **2009**, *95* (22), 1–4.

(131) Williams, N. R.; Molinari, M.; Parker, S. C.; Storr, M. T. Atomistic Investigation of the Structure and Transport Properties of Tilt Grain Boundaries of UO_2. *J. Nucl. Mater.* **2015**, *458*, 45–55.

(132) Metlenko, V.; Ramadan, A. H. H.; Gunkel, F.; Du, H.; Schraknepper, H.; Hoffmann-Eifert, S.; Dittmann, R.; Waser, R.; De Souza, R. A. Do Dislocations Act as Atomic Autobahns for Oxygen in the Perovskite Oxide $SrTiO_3$? *Nanoscale* **2014**, *6* (21), 12864–12876.

(133) De Souza, R. A.; Pietrowski, M. J.; Anselmi-Tamburini, U.; Kim, S.; Munir, Z. A.; Martin, M. Oxygen Diffusion in Nanocrystalline Yttria-Stabilized Zirconia: The Effect of Grain Boundaries. *Phys. Chem. Chem. Phys.* **2008**, *10* (15), 2067–2072.

(134) Sun, L.; Marrocchelli, D.; Yildiz, B. Edge Dislocation Slows down Oxide Ion Diffusion in Doped CeO_2 by Segregation of Charged Defects. *Nat. Commun.* **2015**, *6*, 1–10.

(135) Shen, F.; Dixit, M. B.; Xiao, X.; Hatzell, K. B. Effect of Pore Connectivity on Li Dendrite Propagation within LLZO Electrolytes Observed with Synchrotron X-Ray Tomography. *ACS Energy Lett.* **2018**, *3* (4), 1056–1061.

(136) Tschopp, M. A.; Solanki, K. N.; Gao, F.; Sun, X.; Khaleel, M. A.; Horstemeyer, M. F. Probing Grain Boundary Sink Strength at the Nanoscale: Energetics and Length Scales of Vacancy and Interstitial Absorption by Grain Boundaries in α-Fe. *Phys. Rev. B - Condens. Matter Mater. Phys.* **2012**, *85* (6), 1–21.

(137) Tschopp, M. A.; Coleman, S. P.; McDowell, D. L. Symmetric and Asymmetric Tilt Grain

Boundary Structure and Energy in Cu and Al (and Transferability to Other Fcc Metals). *Integr. Mater. Manuf. Innov.* **2015**, *4* (1), 11.

(138) Rajagopalan, M.; Tschopp, M. A.; Solanki, K. N. Grain Boundary Segregation of Interstitial and Substitutional Impurity Atoms in Alpha-Iron. *Jom* **2014**, *66* (1), 129–138.

(139) Bean, J. J.; McKenna, K. P. Origin of Differences in the Excess Volume of Copper and Nickel Grain Boundaries. *Acta Mater.* **2016**, *110*, 246–257.

(140) Iguchi, F.; Tsurui, T.; Sata, N.; Nagao, Y.; Yugami, H. The Relationship between Chemical Composition Distributions and Specific Grain Boundary Conductivity in Y-Doped $BaZrO_3$ Proton Conductors. *Solid State Ionics* **2009**, *180* (6–8), 563–568.

(141) Shibata, N.; Yamamoto, T.; Ikuhara, Y.; Sakuma, T. Structure of [110] Tilt Grain Boundaries in Zirconia Bicrystals. *J. Electron Microsc. (Tokyo).* **2001**, *50* (6), 429–433.

(142) Jia, C. L. Atomic-Resolution Measurement of Oxygen Concentration In. **2010**, *2001* (2004), 2001–2005.

(143) Kim, M.; Duscher, G.; Browning, N. D.; Sohlberg, K.; Pantelides, S. T.; Pennycook, S. J. Nonstoichiometry and the Electrical Activity of Grain Boundaries in $SrTiO_3$. *Phys. Rev. Lett.* **2001**, *86* (18), 4056–4059.

(144) Siegel, D. J.; Hamilton, J. C. Computational Study of Carbon Segregation and Diffusion within a Nickel Grain Boundary. *Acta Mater.* **2005**, *53* (1), 87–96.

(145) González-Romero, R. L.; Meléndez, J. J.; Gómez-García, D.; Cumbrera, F. L.; Domínguez-Rodríguez, A. A Molecular Dynamics Study of Grain Boundaries in YSZ: Structure, Energetics and Diffusion of Oxygen. *Solid State Ionics* **2012**, *219*, 1–10.

(146) Catarelli, S. R.; Lonsdale, D.; Cheng, L.; Syzdek, J.; Doeff, M. Intermittent Contact Alternating Current Scanning Electrochemical Microscopy: A Method for Mapping Conductivities in Solid Li Ion Conducting Electrolyte Samples . *Frontiers in Energy Research* . 2016, p 14.

(147) El-Shinawi, H.; Paterson, G. W.; MacLaren, D. A.; Cussen, E. J.; Corr, S. A. Low-Temperature Densification of Al-Doped $Li_7La_3Zr_2O_{12}$: A Reliable and Controllable Synthesis of Fast-Ion Conducting Garnets. *J. Mater. Chem. A* **2017**, *5* (1), 319–329.

(148) Li, Y.; Cao, Y.; Guo, X. Influence of Lithium Oxide Additives on Densification and Ionic Conductivity of Garnet-Type $Li_{6.75}La_3Zr_{1.75}Ta_{0.25}O_{12}$ Solid Electrolytes. *Solid State Ionics* **2013**, *253*, 76–80.

(149) Liu, K.; Ma, J. T.; Wang, C. A. Excess Lithium Salt Functions More than Compensating for Lithium Loss When Synthesizing $Li_{6.5}La_3Ta_{0.5}Zr_{1.5}O_{12}$ in Alumina Crucible. *J. Power Sources* **2014**, *260*, 109–114.

(150) Ren, Y.; Deng, H.; Chen, R.; Shen, Y.; Lin, Y.; Nan, C. W. Effects of Li Source on Microstructure and Ionic Conductivity of Al-Contained $Li_{6.75}La_3Zr_{1.75}Ta_{0.25}O_{12}$ Ceramics. *J. Eur. Ceram. Soc.* **2015**, *35* (2), 561–572.

(151) Cheng, L.; Park, J. S.; Hou, H.; Zorba, V.; Chen, G.; Richardson, T.; Cabana, J.; Russo, R.; Doeff, M. Effect of Microstructure and Surface Impurity Segregation on the Electrical and Electrochemical Properties of Dense Al-Substituted $Li_7La_3Zr_2O_{12}$. *J. Mater. Chem. A*

2014, *2* (1), 172–181.

(152) Li, Y.; Han, J. T.; Wang, C. A.; Xie, H.; Goodenough, J. B. Optimizing Li^+ Conductivity in a Garnet Framework. *J. Mater. Chem.* **2012**, *22* (30), 15357–15361.

(153) Jin, Y.; McGinn, P. J. Al-Doped $Li_7La_3Zr_2O_{12}$ Synthesized by a Polymerized Complex Method. *J. Power Sources* **2011**, *196* (20), 8683–8687.

(154) Sundström, L.-G.; Bark, F. H. On Morphological Instability during Electrodeposition with a Stagnant Binary Electrolyte. *Electrochim. Acta* **1995**, *40* (5), 599–614.

(155) Porz, L.; Swamy, T.; Sheldon, B. W.; Rettenwander, D.; Frömling, T.; Thaman, H. L.; Berendts, S.; Uecker, R.; Carter, W. C.; Chiang, Y. M. Mechanism of Lithium Metal Penetration through Inorganic Solid Electrolytes. *Adv. Energy Mater.* **2017**, *7* (20), 1–12.

(156) Li, Y.; Zhou, W.; Chen, X.; Lü, X.; Cui, Z.; Xin, S.; Xue, L.; Jia, Q.; Goodenough, J. B. Mastering the Interface for Advanced All-Solid-State Lithium Rechargeable Batteries. *Proc. Natl. Acad. Sci.* **2016**, *113* (47), 13313–13317.

(157) Aguesse, F.; Manalastas, W.; Buannic, L.; Del Amo, J. M. L.; Singh, G.; Llordés, A.; Kilner, J. Investigating the Dendritic Growth during Full Cell Cycling of Garnet Electrolyte in Direct Contact with Li Metal. *ACS Appl. Mater. Interfaces* **2017**, *9* (4), 3808–3816.

(158) Hongahally Basappa, R.; Ito, T.; Morimura, T.; Bekarevich, R.; Mitsuishi, K.; Yamada, H. Grain Boundary Modification to Suppress Lithium Penetration through Garnet-Type Solid Electrolyte. *J. Power Sources* **2017**, *363*, 145–152.

(159) Wang, C.; Gong, Y.; Dai, J.; Zhang, L.; Xie, H.; Pastel, G.; Liu, B.; Wachsman, E.; Wang, H.; Hu, L. In Situ Neutron Depth Profiling of Lithium Metal-Garnet Interfaces for Solid State Batteries. *J. Am. Chem. Soc.* **2017**, *139* (40), 14257–14264.

(160) Wu, B.; Wang, S.; Lochala, J.; Desrochers, D.; Liu, B.; Zhang, W.; Yang, J.; Xiao, J. The Role of the Solid Electrolyte Interphase Layer in Preventing Li Dendrite Growth in Solid-State Batteries. *Energy Environ. Sci.* **2018**, *11* (7), 1803–1810.

(161) Barai, P.; Higa, K.; Srinivasan, V. Effect of Initial State of Lithium on the Propensity for Dendrite Formation: A Theoretical Study. *J. Electrochem. Soc.* **2017**, *164* (2), A180–A189.

(162) Tikekar, M. D.; Archer, L. A.; Koch, D. L. Stabilizing Electrodeposition in Elastic Solid Electrolytes Containing Immobilized Anions. *Sci. Adv.* **2016**, *2* (7).

(163) Zhou, W.; Li, Y.; Xin, S.; Goodenough, J. B. Rechargeable Sodium All-Solid-State Battery. *ACS Cent. Sci.* **2017**, *3* (1), 52–57.

(164) Virkar, A. V; Viswanathan, L.; Biswas, D. R. On the Deterioration of *β*''-Alumina Ceramics under Electrolytic Conditions. *J. Mater. Sci.* **1980**, *15* (2), 302–308.

(165) Albertus, P.; Babinec, S.; Litzelman, S.; Newman, A. Status and Challenges in Enabling the Lithium Metal Electrode for High-Energy and Low-Cost Rechargeable Batteries. *Nat. Energy* **2018**, *3* (1), 16–21.

(166) Wolfenstine, J.; Allen, J. L.; Sakamoto, J.; Siegel, D. J.; Choe, H. Mechanical Behavior of Li-Ion-Conducting Crystalline Oxide-Based Solid Electrolytes: A Brief Review. *Ionics,*

2017, 1–6.

(167) Adams, J. B.; Wolfer, W. G.; Foiles, S. M. Elastic Properties of Grain Boundaries in Copper and Their Relationship to Bulk Elastic Constants. *Phys. Rev. B* **1989**, *40* (14), 9479–9484.

(168) Nomura, M.; Adams, J. B. Mechanical Properties of Twist Grain Boundaries in Cu. *Interface Sci.* **1994**, *2* (2), 137–146.

(169) Saylor, D. M.; Dasher, B. El; Pang, Y.; Miller, H. M.; Wynblatt, P.; Rollett, A. D.; Rohrer, G. S. Habits of Grains in Dense Polycrystalline Solids. *J. Am. Ceram. Soc.* **2004**, *87* (4), 724–726.

(170) Canepa, P.; Dawson, J. A.; Sai Gautam, G.; Statham, J. M.; Parker, S. C.; Islam, M. S. Particle Morphology and Lithium Segregation to Surfaces of the $Li_7La_3Zr_2O_{12}$ Solid Electrolyte. *Chem. Mater.* **2018**, *30* (9), 3019–3027.

(171) Klenk, M. J.; Lai, W. Finite-Size Effects on the Molecular Dynamics Simulation of Fast-Ion Conductors: A Case Study of Lithium Garnet Oxide $Li_7La_3Zr_2O_{12}$. *Solid State Ionics* **2016**, *289*, 143–149.

(172) Jalem, R.; Rushton, M. J. D.; Manalastas, W.; Nakayama, M.; Kasuga, T.; Kilner, J. A.; Grimes, R. W. Effects of Gallium Doping in Garnet-Type $Li_7La_3Zr_2O_{12}$ Solid Electrolytes. *Chem. Mater.* **2015**, *27* (8), 2821–2831.

(173) de Jong, M.; Chen, W.; Angsten, T.; Jain, A.; Notestine, R.; Gamst, A.; Sluiter, M.; Krishna Ande, C.; van der Zwaag, S.; Plata, J. J.; et al. Charting the Complete Elastic Properties of Inorganic Crystalline Compounds. *Sci. Data* **2015**, *2*, 150009.